博士論文

Teleoperated 2-D Micro/Nanomanipulation Using Atomic Force Microscope

原子間力顕微鏡を用いたマイクロ / ナノ・テレマニピュレーション・システムに関する基礎研究

指導教官

橋本 秀紀 助教授

東京大学大学院 工学系研究科

電気工学専攻 ６７３１６

Sitti Metin

平成１１年６月１８日提出

Abstract

The target of this thesis is the teleoperated 2-D pushing of micro/nanoparticles and touching interaction at the micro/nano scale using Atomic Force Microscope (AFM) for reducing the manipulation and interaction barrier between macro and micro/nano worlds. For this purpose, a system called Tele-Micro/Nanomanipulator is proposed. In this system, AFM is utilized as the micro/nanomanipulator, and also the 3-D nano scale topology sensor and micro/nano force sensor. As AFM, a home-made open structure AFM system using piezoresistive cantilevers and sensor-integrated closed-loop XYZ positioners is constructed. In the macro world part of the system, a Virtual Reality-based visual and force display user interface is utilized for controlling the motions of the AFM cantilever by a direct teleoperation control or task-based teleoperation control. Shaded images of the AFM scanning data are displayed interactively, and a 1-DOF home-made haptic device has been used for real-time micro/nano scale force/tactile feedback and generating motion commands for the AFM cantilever. Between the macro and micro/nano worlds, scaled bilateral teleoperation controllers are proposed taking the scaling and bandwidth effects into consideration. These controllers utilize Virtual Impedance and force-reflecting position servo controller approaches. Methods are proposed for the selection of the scaling factors for the force and position information.

Using the AFM cantilever tip, mechanical contact push/pull, cutting, drilling, and etc. kind of 1-D or 2-D manipulations are possible at the micro/nano scale. Tele-Micro/Nanomanipulator system is focused especially on pushing manipulation and touching interaction. Dynamical modeling and control of the AFM cantilever, and modeling of micro/nano scale forces using continuum mechanics models have been proposed for these applications. Pushing of micro/nano particles are utilized in two ways: 2-D positioning/assembly of particles on substrates, and tribological characterization of particle-substrate interfaces. As pushing experiments, gold-coated 2, 1 and 0.48 μm size latex particles are positioned on silicon substrates, and also the frictional behaviour between the latex particles and silicon substrate is observed in ambient conditions. Different behaviours such as pure sliding, stick-slip, or rolling are observed. Furthermore, precise values of shearing forces are measured. For the touching experiments tele-compliance feedback of selected points on silicon and mica surfaces, and tele-tactile feedback of silicon fabricated etched patterns are realized. These experiments show that the system can be utilized for pushing and touching applications at the micro/nano scale, and modeled dynamics and forces correspond with the experimental results.

論文の内容の要旨

本論文の主眼は、マクロ世界とマイクロ / ナノ世界の間に存在する、マニピュレーションとインタラクションにおける障壁の高さを下げることを目的として、原子間力顕微鏡 (Atomic Force Microscope; AFM) を用いた、マイクロ / ナノ粒子の遠隔操作型 2 次元プッシングとマイクロ / ナノスケールでの接触インタラクションにある。この目的のために遠隔マイクロ / ナノマニピュレーションというシステムを提案する。このシステムでは、 AFM をマイクロ / ナノマニピュレータとして、さらには、 3 次元ナノスケールのトポロジーセンサー、あるいはマイクロ / ナノ力センサとして利用する。 AFM として、開構造の AFM システムをピエゾ抵抗カンチレバーとセンサ集積の閉ループ XYZ ポジショナーとを用いて自作した。システムのマクロ世界の部分では、バーチャル・リアリティを基礎とした視覚および力覚提示ユーザインタフェースが利用される。これによって、AFM のカンチレバーの動作は直接遠隔操作制御、あるいはタスクに基づいた遠隔操作制御によって制御される。 AFM 走査データの画像はインタラクティブに提示される。さらに、自作した 1 自由度ハプティック・デバイスは、実時間マイクロ / ナノスケール力覚 / 触覚フィードバックと AFM カンチレバーの動作コマンドの生成のために用いられる。マクロ世界とマイクロ / ナノ世界の間を結ぶために、スケーリング効果とバンド幅効果を考慮に入れた、スケールド・バイラテラル遠隔操作制御系を提案する。これらの制御系では、バーチャル・インピーダンスと力覚反射位置サーボ制御系アプローチを用いる。力と位置の情報に対してスケーリング・ファクタの選択方法を提案する。

AFM カンチレバーの探針を使うことで、機械的な接触、プッシュ / プル、カット、ドリルなどいくつかの 1 次元、 2 次元マニピュレーションがマイクロ / ナノスケールで可能となる。遠隔マイクロ / ナノマニピュレーション・システムではプッシング操作と接触インタラクションに焦点をあてる。これらの応用のために、連続体の力学モデルを用いた、 AFM の動的モデルと制御やマイクロ / ナノスケールの力のモデリングを提案する。マイクロ / ナノ粒子のプッシングは 2 つの観点で利用される。それは、試料上の粒子の 2 次元位置決めと組み立てと粒子と試料の間のインタフェースのトライボロジー的性質である。プッシング実験として、金でコーティングされた 2、 1、 0.48 マイクロメータ・サイズのラテック粒子がシリコン試料上におかれ、ラテック粒子とシリコン試料との間の摩擦を伴う挙動を大気中で観察する。純粋な滑べり、スティックスリップ、回転のような異なる挙動も観測される。さらに、切断力の精密な値が測定される。接触実験では、シリコンあるいはマイカ表面上の選択した点の遠隔コンプライアンス・フィードバックとシリコン・エッチング模様の遠隔触覚フィードバックが実現される。これらの実験から、本システムがマイクロ / ナノスケールでのプッシングと接触という応用に対して有効であること、さらにはモデル化されたダイナミクスと力が実験結果と一致することが示せた。

Acknowledgements

First of all, I would like to thank to my advisor Prof. Hideki Hashimoto for his enduring support, encouragement, discussions and kindness all along my thesis work. He pushed me to enter to a new research area of micro/nano-robotics which opened to me new horizons in the academic, philosophical and technological respects. At this point, our Tele-Nanorobotics project has also blossomed with the encouragement and cooperation of Prof. Fumio Harashima and Dr. Moussa Hoummady.

I am thankful to all Hashimoto Laboratory members who supported me in every sense. Since my project started with almost zero budget, the other projects in the laboratory financed the initial setup equipment costs. Mrs. Yamamoto always assisted in my applications and documents with her smiling face. Satoshi Horiguchi has contributed to the project in developing the Virtual Reality graphics interface, and also helped for the Japanese translations a lot. Also Joo-Ho Lee, Noriaki Ando, Toshiyuki Ohashi, Kiyotaka Hirahara, and all other students have kindly helped me in hardware and software problems, official procedures, and accompanied me in my Roppongi life.

LIMMS laboratory with French (CNRS) and Japanese (Univ. of Tokyo) researchers in the Institute of Industrial Science is one of the most important collaborators of my work. Prof. Hiroyuki Fujita contributed with his discussions, comments, and technical helps in MEMS-related points. Prof. Yasuhiko Arakawa had comments about the applications of our system, and provided InAs AFM image samples. Prof. Hideki Kawakatsu gave some hints about the AFM instrumentation with his AFM/STM expertise.

I am very thankful to the professors in my dissertation jury for their invaluable comments and discussions.

Two-month visitors from France, Yves Rollot from LPR in Paris and Jean-Michel Friedt from LPMO in Besancon, provided many discussions and knowledge exchange opportunities. Yves joined me in micro force modeling issues, and Jean-Michel helped to the AFM AC measurement circuit hardware and AFM contact mode imaging experiments.

Prof. Andreas Stemmer from ETHZ shared my insistance on theoretical modeling of the micro/nano forces for understanding the phenomenon during the micro/nano manipulation by email communication.

The fruitful discussions with companies also improved my technical knowledge and enabled the home-made AFM system. We are thankful to the Park Scientific Instruments Co. for providing the piezoresistive cantilevers, Olympus Co. for the special type Optical Micrsocope system, and Physick Instrumente Co. for the closed-loop

positioning stage.

Ozlem always shared the same way with me with her love and enduring support. This thesis would not be possible without her accompany in my hard and happy times. Moreover, my family in Turkey has been always with me during my work in Tokyo not physically but with their heartful understanding and motivation support.

The last but not the least, I am thankful to the Japanese Ministry of Education for providing me the Monbusho Research Scholarship all along my study.

Contents

List of Figures

List of Tables

Chapter 1

Introduction

Controlled action at a distance, teleoperation, has been used since the earliest times to extend man's reach into hostile or distant places. Tele-robotics systems for operating robots in hazardous environments such as nuclear plants, and remote sites such as outer space or deep sea have been a recent hot topic in the field of teleoperation. Besides of these kinds of applications, there is a new emerging application area of such systems which we call *Tele-Micro/Nanorobotics*. Since man has barriers with micro and nano scale worlds as shown in Figure 1.1, i.e. cannot sense, interact or manipulate directly in these worlds, one solution is teleoperation between macro and micro/nano worlds. This kind of application has become possible by the trends in imaging, manipulation and fabrication technologies as shown in Figure 1.2 (from [64]) using the micro/nano mechatronics and MEMS technologies. By the the invention of Scanning Tunneling Microscope (STM) and Atomic Force Miscoscope (AFM), 3-D topology images with even atomic resolution have become possible. Although the micro/nano scale imaging technologies are being established, micro/nano scale manipulation and fabrication technologies are still in their early infancy. Therefore, Tele-Micro/Nanorobotics approach is to be utilized for proposing new techniques for the manipulation and fabrication of the micro/nano scale objects in this study.

1.1 Micro/Nano Manipulation: Necessity of a New Robotics Field

Going from macro to micro/nano world, the main phenomenon is the reduction of the size of objects where the effect of length change is defined as *scaling effect*. Scaling effect for different physical and geometrical parameters can be seen in Table 1.1 and Figure 1.4. As can be seen from the table and figure, by decreasing the size, for example, inertial forces decrease with the power of 4, and angle/rotational information does not change. Considering these kind of effects, following physical and other object property

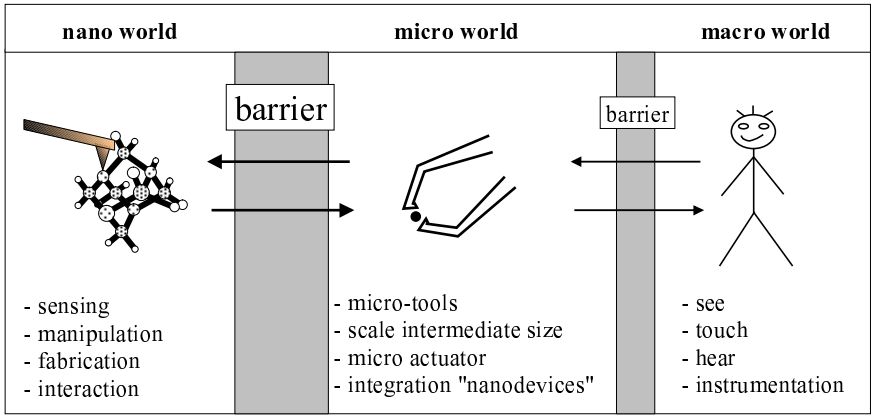

Figure 1.1: Barriers among macro, micro and nano worlds.

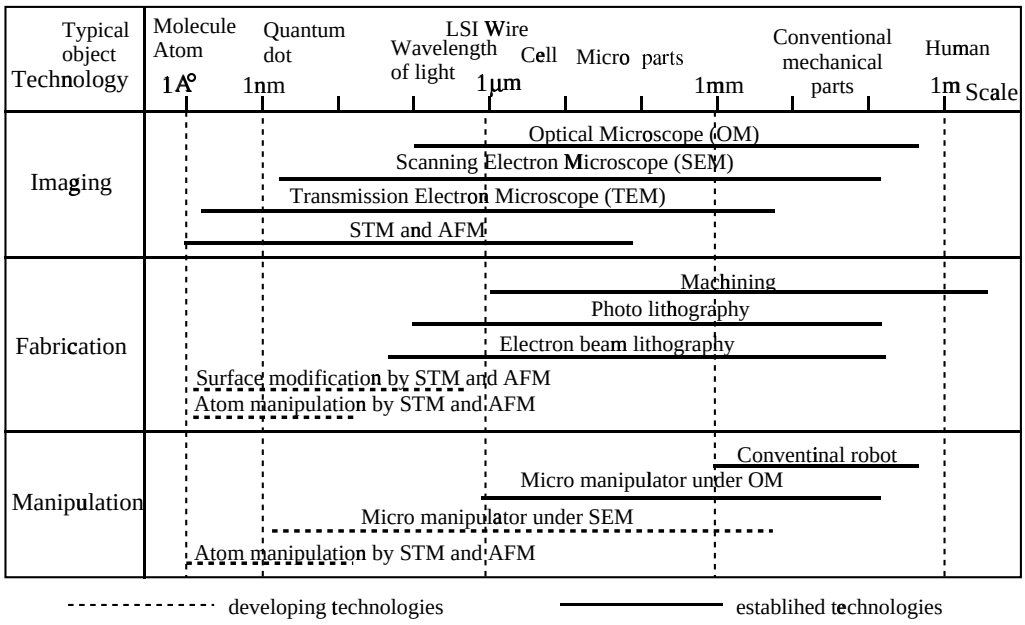

Figure 1.2: Imaging, fabrication and manipulation technologies in the micro/nano world.

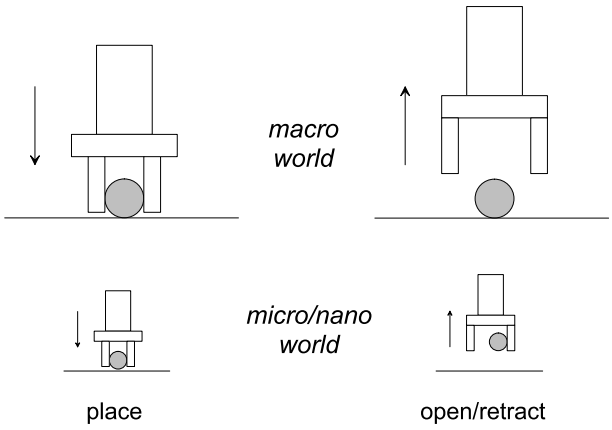

Figure 1.3: Example case of the sticking effect at the micro/nano scale during placing an object and moving back.

changes occur at the micro/nano scale due to the scaling effect:

- Other surface or adhesion forces such as van der Waals, electrostatic and capillary forces become dominant with respect to the intertial forces [21], [2]. As different from the macro scale object manipulation, this dominancy may result in *sticking effect* where an example of the sticking of the objects to the gripper at the micro/nano world during placing an object is shown in Figure 1.3.
- Going to few nanometer or molecular scale, continuum mechanics is not valid, a new physics utilizing electromechanical quantum mechanics and chemistry is necessary for exact analysis.
- Besides of applied load, frictional forces become affected by adhesion forces which differs from the macro world. Thus, a new definition of friction is needed for the micro/nano scale.
- Resonant frequency increases with the length power of 1 which implies that the dynamics in the nano world is very fast. Therefore, quasi-static dynamics approaches are more feasible for a teleoperated micro/nano manipulation control case.
- *Specifity* incerases in the sense of manipulation task such that sticking forces depend on the object geometry and material type, object-gripper distance, environmental parameters such as temperature and humidity, and environement type such as air, vacuum or liquid. Thus, manipulation, sensing, control and micro/nano manipulator design strategy depends intensely on the task specification and environment.

- Objects become more fragile and easily deformed with imperfect shapes. Thus, visual feedback is very important for uncertain object and micro/nano gripper shapes, and force-feedback is needed for not breaking or deforming the objects and the manipulation tool at the micro/nano scale.
- Rotational position is not affected by scaling, but the translational positioning is linearly scaled which means high precision linear positioning is necessary for micro/nano manipulation.
- Manipulation control becomes sensitive to environmental disturbances, and uncertain environmental parameters may result in unpredicted effects.

Taking the above points into consideration, *micro/nano physics-based robotics and sensing with intelligent control* is indispensible for micro/nano manipulation. Following features are needed for the new robotics field:

1. Design of micro/nano grippers taking the sticking effect and specific task into consideration (reducing the sticking forces [3], or controlling adhesive forces ([70], [59], [22]),
2. Nanometer precision intelligent manipulation control with sensory (visual and force) feedback due to the uncertain and nonlinear dynamics and disturbances: teleoperated control or real-time semi-autonomous sensory feedback intelligent control,
3. Robust and stable nonlinear controller design is necessary due to the nonlinearity and uncertainties at the actuators and manipulation interactions,
4. Cameras are replaced by micro/nano physics-based microscopy,
5. At the molecular scale (*molecular robotics* case), besides of nano physics, chemistry is indispensible for controlled manipulation; micro/nanorobotics necessitates interdisciplinary research among engineers and scientists.

1.2 Micro/Nano Manipulation Approaches

Micro/nano scale manipulation approaches can be classified depending on the starting point, process, interaction and operation as given in Figure 1.5. At the respect of starting point for manipulation, manipulation systems can be classified as *bottom-up* and *top-down* approaches [42]. In bottom-up approach [66], [57], [76], [37], knowing how to manipulate atoms or molecules using STM or AFM, larger objects (that even

Parameter	*Equation*	*Scaling Effect*
Length	L	L
Surface Area	$\propto L^2$	L^2
Volume	$\propto L^3$	L^3
Mass	ρV	L^3
Pressure	SP	L^2
Gravitational Force	mg	L^3
Inertial Force	$m\frac{d^2x}{dt^2}$	L^4
Viscosity Force	$c\frac{S}{L}\frac{\partial x}{\partial t}$	L^2
Elastic Force	$eS\frac{\Delta L}{L}$	L^2
Linear Spring Constant	$2UV/(\Delta L)^2$	L
Eigen Vibration Frequency	$\sqrt{K/m}$	L^{-1}
Angular Momentum	amr^2	L^5
Electrostatic Force	$\frac{\epsilon S}{2}\frac{V^2}{d^2}$	L^0
Electromagnetic Force	$\frac{B}{2\mu}S_m$	L^2
Thermal Expansion Force	$eS\frac{\Delta L(T)}{L}$	L^2
Piezoelectric Force	$eS\frac{\Delta L(E)}{L}$	L^2

Table 1.1: Scaling effect in the physical parameters.

may not exist in the nature) are trying to be built. Such kind of nanotechnology is the ultimate goal in the miniaturization. However, we can not neither handle micro parts as large as $100nm$ nor correct micro defects of a LSI mask by STM, because STM can only be utilized to handle objects of atomic scale at present. On the other hand, the top-down approach [53], [33], [38], [65], [39], [60], [78], [6], [51] starts from familiar operations in the macroscobic world and moves towards the smaller and smaller objects and more and more precision of handling. In this most frequently utilized approach Codourey *et al.* [12] achieved pick and place task of octagonal diamonds with $50\mu m$ diameter in the project titled *Nano-Robotics* under Optical Microscope (OM). Koyano et al. [41] proposed new micro object handling and teleoperation system with concentrated visual fileds and new handling skills. They achieved to fabricate pyramidal 3-D structures made of polymer particles of $2\mu m$ in diameter using Scanning Electron Microscope (SEM) and two-arm micro-manipulator system [49]. Zesch et al. [84] utilized piezoresistive AFM cantilevers for force controlled 2-D pushing of microparts on a planar substrate. Zhou et al. [85] try to control the position of a microcantilever on a substrate precisely by integrating visual and force information. Their result show the improved performance by using also force feedback.

As the manipulation process, biochemical processes such as *self-assembly* can be uti-

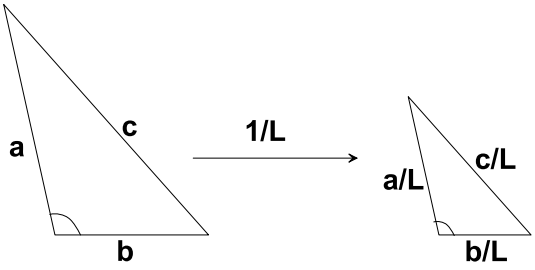

Figure 1.4: Scaling effect in the geometric parameters.

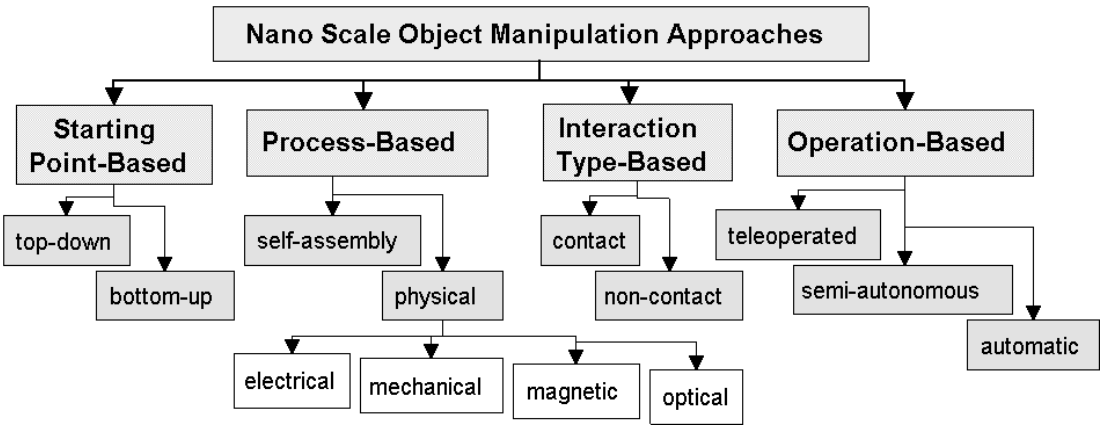

Figure 1.5: Micro/Nano scale object manipulation approach classifications.

lized for constructing micro/nano devices or materials. Several laboratories especially in the fields of chemistry (supramolecular chemistry) and biology are trying to use this approach [43] where it is promising in building higly-repetitive or symmetrical structures, but is unlikely to produce, by itself, the asymmetric structures needed in nano machinery, and they are ill-suited for rapid prototyping. The second approach which can be called as *physical manipulation* is aimed in manipulating selected particular micro/nano objects locally in high precision using physical effects, i.e. forces such as electrical, mechanical, magnetic and optical forces. By physical manipulation, an external force for positioning or assembling objects in 2-D or 3-D, cutting, drilling, twisting, bending, pick-and-place, push and pull kind of tasks are to be meant. STM-based atom/molecule manipulation systems control the electrical force between the metallic STM probe and the substrate atom/molecules for pick-and-place, or push and pull kind of tasks [76], [44], [80]. AFM-based manipulation systems utilize the AFM tip for pushing or pulling nano objects such as particles [66], [37], [4], [26], [5], [68] or cutting DNA [75] or fiber [52], and etc. by controlling the applied mechanical load on the sample. AFM-based the smallest pushed particle is around 15 nm radius upon our knowledge

due to the mechanical difficulties for moving atoms or molecules in the respects of tip size and strong interatomic forces. Inoue et al. [34] utilize magnetic fields to control the motion of the microparts. Finally, laser trapping approaches can be used to move micro/nano particles in 2-D or 3-D by the applied laser light force [63].

Depending on the interaction type, *non-contact* and *contact* manipulation systems exist. In the former, laser trapping (optical tweezers) or electrostatic or magnetic field forces are utilized. Yamomoto et al. [17] can cut DNA using restriction enzymes on a laser trapped bead, and Stroscio et al. [76] utilized electrical force between STM probe tip and surface atoms for non-contact manipulation of Xe or Ni atoms. As the contact manipulation, AFM probe tip is utilized for positioning particles on a substrate by contact pushing or pulling operations [66], [37], [58].

As the operation-based approaches, there are *teleoperated* and *automatic* approaches [74]. Since the micro/nano physical and chemical phenomenon which is still not completely understood, it is early for automatic manipulation systems, and teleoperation technology at the initial phase is a promising tool for understanding these uncertainties and improving automatic manipulation strategies using the human intelligence [67]. Teleoperation systems have the stages of *direct teleoperation*, and *task-based/semi-autonomous* teleoperation systems where in the former, an operator directly enters to the control-loop of the micro/nanomanipulator (Figure 1.6.a), and in the latter, the operator only sends high-level task commands, and the manipulator realizes the tasks in an autonomous way (Figure 1.6.b). Hollis et al. [30] utilized STM probe as the slave-robot and 6-DOF fine motion device called Magic Wrist as the master device for feeling atomic scale topography in operator's hand. They tried to feel the topology of gold and graphite, but there were problems of mechanical and electrical noise which deforms the tactile feeling, and no true force-reflecting behaviour. The nanoManipulator group [] utilizes commercial AFM and haptic device for real-time haptic display. They utilize plane and probe model [18], [45], [25] for surface force feedback, but they do not have any report on scaled teleoperation control problem and micro/nano force modeling. The final goal is fully automatic systems which can enable the mass-production of micro/nano robots or machines in the future, but there is no such a work yet.

For the imaging devices during micro/nano manipulation, OM, SEM, AFM and STM are most frequently used microscopes where their properties are reported in Table 1.2. Until to 1 μm scale OM integrated with CCD camera is enough with 30-100 frames/sec speed. However, for submicron imaging OM cannot be used mostly (using special techniques such as fulleoresance labeling, submicron imaging is possible). Therefore SEM, AFM or STM is utilized where SEM has limitations in the sense of requiring vacuum chamber, getting only 2-D image and works only for conducting and some semi-conducting objects, and STM can be utilized only for conducting and semi-conducting objects. However, AFM can be used for any object, thus it is especially unique in the biological field where biological objects can be observed even in liquid *in vitro*.

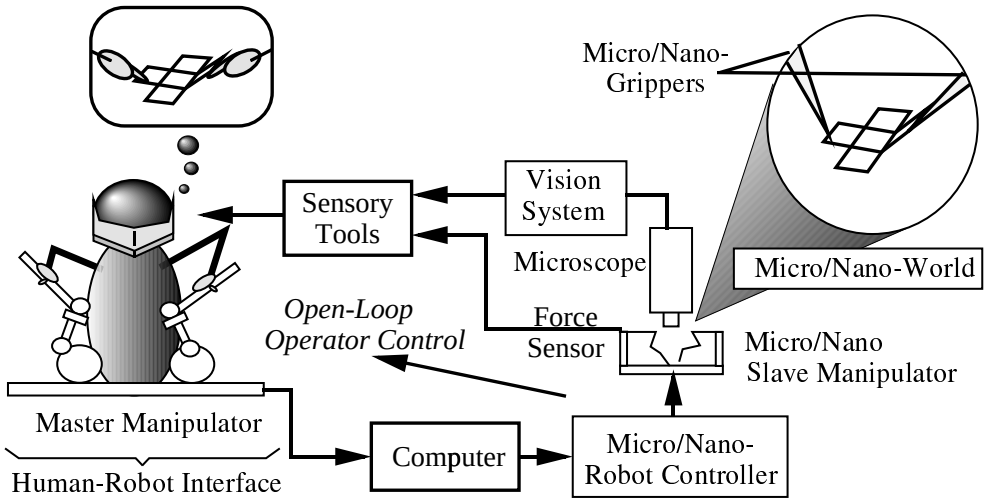

(a) Direct teleoperation.

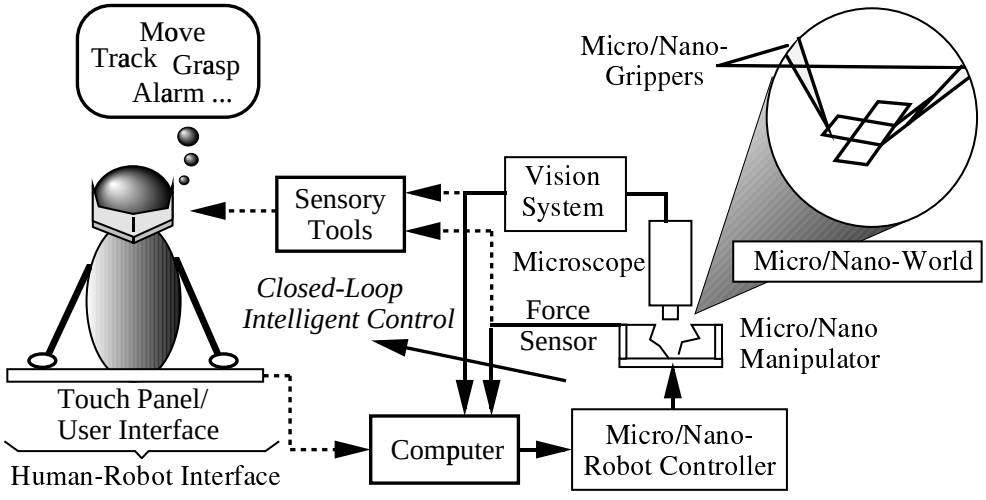

(b) Task-oriented teleoperation.

Figure 1.6: Direct teleoperation (a) and task-oriented (b) teleoperation system structures.

Microscopes *Properties*	**AFM**	**STM**	**SEM**	**0M**
Heighest Resolution	0.1 nm	0.1 nm	~ 5 nm	~ 40 nm
Visible Object Types	all	(1/2)conductors	(1/2)conductors	all
Imaging Type	near-field	near-field	far-field	far-field
Object Interaction	contact non-contact	non-contact	non-contact	non-contact
Imaging Environment	all	vacuum or air	vacuum	air or liquid
Imaging Principle	interatomic forces	tunneling current	electron emission	material-light interaction
Imaging Dimensions	3-D	3-D	2-D	2-D

Table 1.2: Imaging devices used for micro/nano manipulation and their properties.

Thus, AFM is selected for nano scale imaging in this study for not putting limitations on the object types. Finally, the vision sensors can be classified as *far-field* or *near-field* sensors where far-field sensors can get images of the manipulation tool and the manipulated object from another reference while in near-field case only the relative distance between the tool and object can be held during manipulation. Thus, far-field sensor is preferable for easy manipulation, but it is not possible in few nanometer scale with present technology.

1.3 Application Areas

Micro/nano manipulation systems constitute one of the major branches of the nanotechnology research which is one of the crucial technologies of the forthcoming century. Applications of these manipulation systems inside the nanotechnology research can be divided into parts depending on the filed such as molecular biology and genetics, solid-state physics, chemistry, material science, computer industry and medicine as shown in Figure 1.7.

In the field of molecular biology and genetics, DNA is a very popular nano object since its precise manipulation can cause a breakthrough in genetics research. Using laser trapping, single DNA molecules in their globular states are trapped in a buffer solution [40]. Yuqiu et al. [83] utilized mechanical, electrical and chemical approaches to move and extend single DNA molecules. Morishima et al. [50] transported DNA molecules using dielectrophoretic forces. Furthermore, Stark et al. [75] used AFM tip for dissection of chromosomes in ambient conditions and buffer.

Viruses (between 1-50 nm sizes) are also manipulated. Individual tabacco viruses are manipulated using AFM tip for understanding their friction and mechanical properties

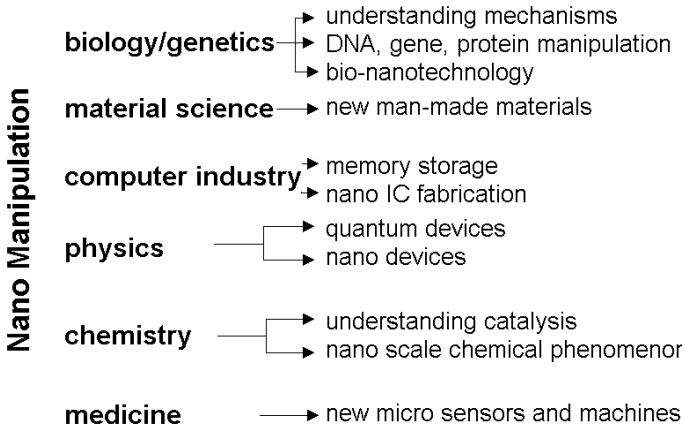

Figure 1.7: Application areas of the micro/nano manipulation systems.

[19]. By this way, it may become possible to understand the mechanism of adhesion mechanism of the viruses during entering inside of a cell.

On the other hand, in order to construct new solid-state devices, precise manipulation and fabrication systems are indispensible. Because present LIGA processes have the limit of 100 nm for chip industry, and a new nano fabrication technology is necessary. For this kind of technology, STM-based approaches can be useful such that Eigler et al. [16] showed the possibility of moving metal atoms such that nano wires or other conducting components can be fabricated. On the other hand, Aono et al. [1] used two STM probes to measure conductance properties of the solid-state structures very precisely and locally.

In the computer technology area, high-density memory storage is one of the important challenging technologies for the computer industry, and many researchers are proposing new methods. One of them is using STM or AFM probes for writing and reading on a disk. Requicha et al. [56] manipulate gold particles with 15 nm size such that they can be positioned precisely in 2-D, and memory can be created by putting a particle to an array or not (if there is a particle:1, if not:0).

1.4 Our Approach

A **teleoperated**, **mechanical** and **contact type** micro/nano manipulation system for the 2-D manipulation of **any type of micro/nano scale objects** with sizes in the range of $10nm - 5\mu m$ in **any type of environment** (air, liquid or vacuum) is proposed. With this system, it is possible to *manually* probe surfaces at nanometric scale, while *feeling* the nano force and topology in the operator's hand. AFM is selected

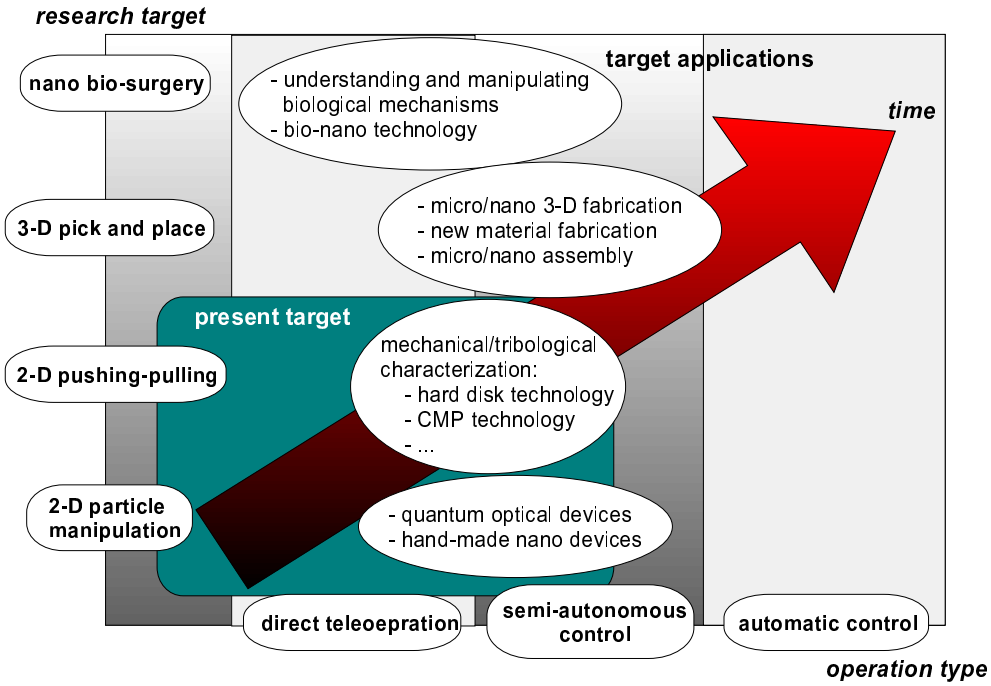

Figure 1.8: The target of the overall micro/nano manipulation project.

to be the micro/nano manipulator which can push, pull or cut micro/nano objects by applied contact force as well as the micro/nano topology and force sensor. Designing a scaled bilateral force feedback teleoperation control system using a haptic device, AFM probe xyz motion is controlled by the operator directly or in semi-autonomous way. By constructing the telemanipulation system, the unmature knowledge of micro/nano forces between the AFM probe and the micro/nano objects during manipulation is aimed to be improved and understood more clearly by analytical and experimental models. The present and future target of the manipulation system is given in Figure 1.8.

1.5 Contributions

This paper discusses the integration of the *micro/nano mechatronics* technology such as AFM, precision positioning, micro/nano actuators, sensors and grippers, and etc., and *macro mechatronics* technology such as tele-robotics, intelligent robot control, advanced-user interfaces, and etc. For this purpose, a bilateral force feedback tele-operation control system with nano scale force modeling for the micro/nano scale tele-manipulation applications where a 3-D Virtual Reality (VR) visualization interface and

1 DOF haptic master device coupled with a home-made AFM for feeling and manipulating nano scale objects are constructed. The contributions of this study are:

- physical modeling of the interaction forces between AFM tip and samples for 2-D micro/nano manipulation applications in order to understand the underlying physical phenomenon; thus, development of reliable strategies for the micro/nano particle manipulation, and construction of a novel Virtual Reality Simulator tool for interacting with the micro/nano scale world,
- discussing the scaled bilateral teleoperation control problem with real nano scale experimental data for the first time:
  - tele-touch to substrates at the nano scale,
  - user-friendly micro/nano manipulation user interface with real-time force-feedback,
  - showing the necessity of real-time force feedback in the nano world where real-time visual feedback may not be possible and can contain many errors,
- constructing an **open-hardware** and **open-software** AFM system specific to manipulation applications for controlling every parameter directly,
- showing the effectiveness of using piezoresistive cantilevers as future self-sensing micro-robot grippers: force-controlled 2-D positioning of micro/nanoparticles using piezolevers.

1.6 Outline of the Thesis

The organization of the paper is as follows: at first, the overall Tele-Micro/Nanomanipulator system setup is given. Then as the part of the system, *micro/nano world* with AFM, visual and force sensing, control and manipulator issues, *macro world* with user interface consisting of visual and force displays, and *macro to micro/nano world* with scaled bilateral teleoperation control problem are explained. As the applications of the system, at first tele-touch to surfaces, and next, controlled pushing of micro/nanoparticles are explained with problem definition, strategy, user interface, experimental results and discussions. Finally, conclusions and future remarks are reported.

Chapter 2

Tele-Micro/Nanomanipulator System Setup

The general structure of the Tele-Micro/Nanomanipulator system is given in Figure 2.1. The main components are: the user interface in the macro world, micro/nano manipulator, actuator and sensors in the micro/nano world, and teleoperation control between both worlds.

In this study, there are two different systems to be constructed:

- **System I: Tele-Microrobotics System**

  In this setup given in Figure 2, micro scale objects are manipulated using the AFM cantilever tip for 2-D positioning on a substrate. Vision sensor is Optical Microscope (OM), force sensor is AFM, and user interface consists of monitor for task-based (semi-autonomous) teleoperation. With this system, micro objects with sizes between 1-5 μm can be positioned or assembled in 2-D.

- **System II: Tele-Nanorobotics System**

  For manipulating objects that cannot be seen using OM, the setup in Figure 2.3 is constructed. Here, AFM is the vision and force sensors, and manipulation tool at the same time. The operation type is direct teleoperation where a Virtual Reality (VR)-based 3-D computer graphics and force feedback interface is constructed. With this system, nano objects with the sizes down to 10s of nanometer can be manipulated in 2-D.

The main feature of these systems is being open-structure such that:

1. open-structure:

   - the software and hardware can be easily changed or replaced directly due to the open-software C programming with all communication (TCP/IP, RS232

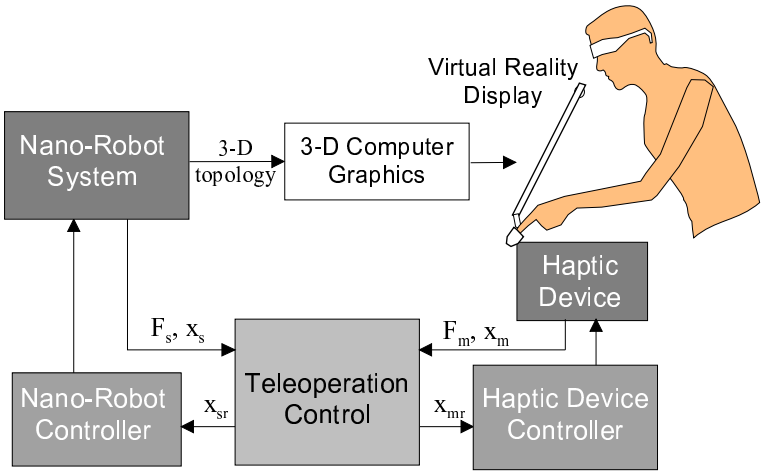

Figure 2.1: The structure of a teleoperated nano manipulation system.

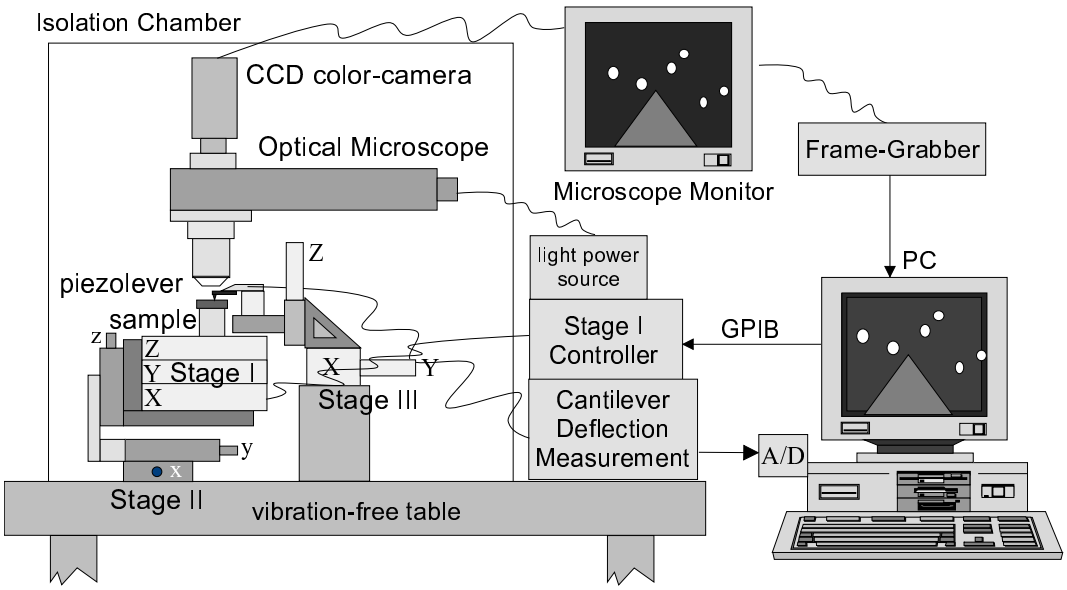

Figure 2.2: Tele-Microrobotics system setup with task-based teleoperation control.

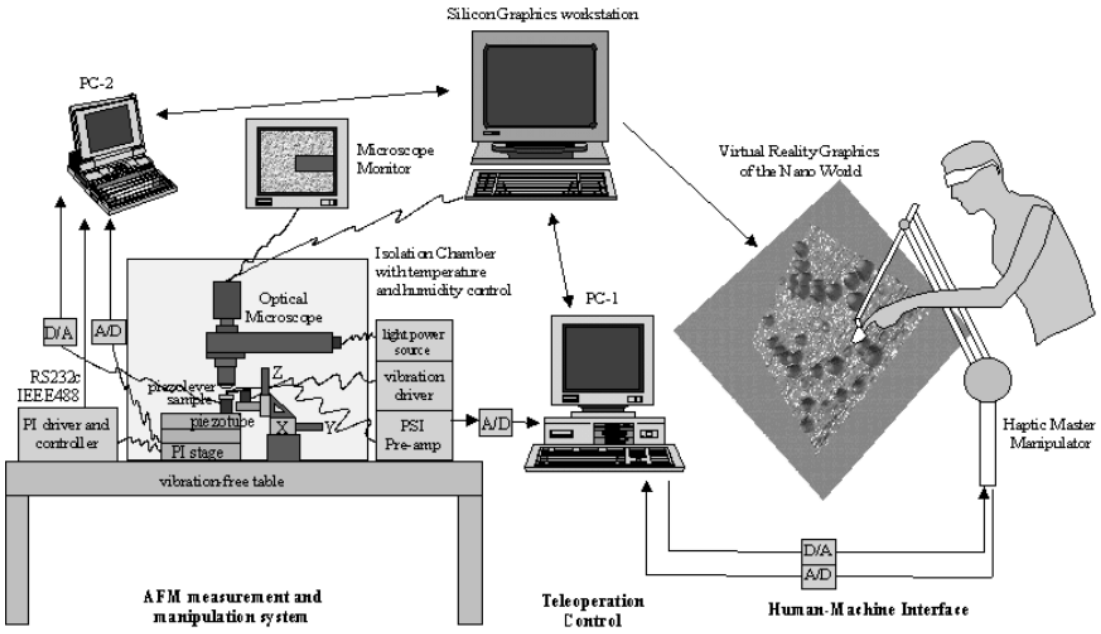

Figure 2.3: Tele-Micro/Nanomanipulator system setup with direct teleoperation control.

and GPIB), data acquisition (A/D boards), graphics library (ImageLib, Glut and OpenGL libraries in C++ programming), algorithms in C programming, and hardware control tools (D/A boards and communication interfaces),

- modular: systems can be used for different tasks with minor changes,
- all hardware can be accessed from the software,
- networked applications are also possible using the Ethernet,

2. rough to fine methodology:

   - imaging in the micro scale using the optical microscope (OM), and zooming through the 2-D display to get nano scale images using the AFM,
   - rough manual positioners are utilized for initial micro scale alignment, and then the computer controlled piezo-positioner enables the fine positioning.

3. real-time:

   - all hardware signals are recieved and sent using fast A/D and D/A 16 bit boards: real-time AFM and operator force and position measurements with bilateral teleoperation controller algorithm enable reliable force-feedback micro/nano manipulation experiments,
   - real-time Linux OS is utilized for controlled sampling time of 500 Hz for the all control software,
   - OM images are displayed using a frame grabber with 50 Hz sampling time,

4. user friendly: Virtual Reality (VR) user interface with haptic feedback of scaled nano forces, and 2-D and 3-D graphics displays of OM and AFM images enables a dexterous teleoperated nano manipulation interface.

Chapter 3

System Part I: Micro/Nano World

Micro/nano world part of the system consists of AFM system with piezoresistive cantilever as the 3-D topology microscope, force sensor and contact manipulation tool, modeling and understanding of AFM probe-nano object interaction forces and dynamics for reliable manipulation control, and nanometer precision fine positioning control.

3.1 Atomic Force Microscope

The basic structure of a conventional AFM system is shown in Figure 3.1. The basic components of AFM are the MEMS fabricated flexible cantilever beam, the deflection measurement system with atomic resolution, and XYZ positioner with atomic resolution. Cantilever has a measured spring constant k_c, resonant frequency f_r, $100-400\ \mu m$ length and few micrometer thickness and very sharp conical, pyramidal or cylindirical tip with 10s of nanometer apex radius. Cantilever beam deflection can be measured using a laser light with four-cell photodiodes, conductance measurements, or piezoresistance or piezoelectricity measurement depending on the cantilever type and purpose. Using piezoelectric actuators with or without integrated sensors, the z position of the tip or sample is changed until there is a contact between the cantilever tip apex and sample atoms. Due to long-range or short-range attractive or repulsive interatomic forces (an overall summary of all microscopic and macroscopic forces can be found in [62]), $F_z(t)$, the cantilever is deflected as $\zeta(t)$ depending on the tip-sample distance $h(t)$. The typical $\zeta(t)$-$h(t)$ relation is shown in Figure 3.2. At the beginning, the tip is far away from the sample where there is no interatomic force and deflection, but when h becomes approximately $20-50\ nm$, there occurs an attraction due to long range van der Waals and electrostatic forces. This attraction region is called *non-contact* region. Then the tip contacts to the sample around $1-2\ A^o$ distance where $F_z = 0$ after an attractive force peak. Moving the tip (or sample) more, short-range Pauli forces between tip and sample atoms repel each other, and the cantilever is elastically deformed

almost in a linear way. This region is called *contact region*. If the tip is moved more, then there may be plastic deformation which is not desirable for imaging. If the tip is retracted in the same way there occurs a hystheresis at the attractive force peak due to the tip-sample adhesion.

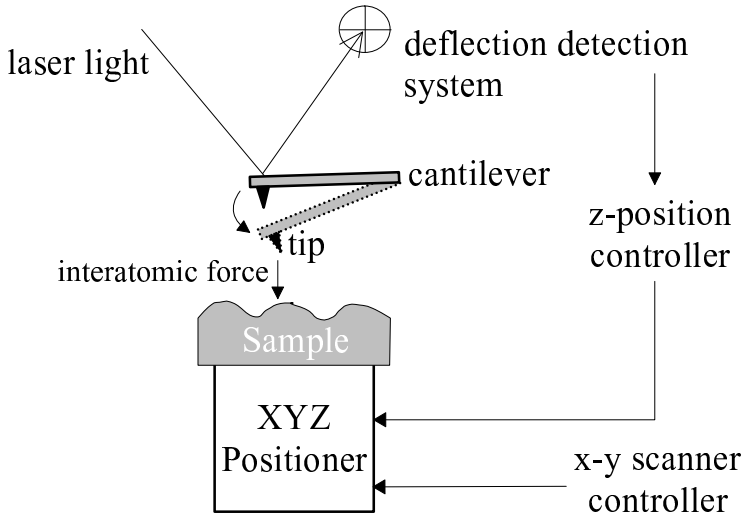

Figure 3.1: The basic structure of a conventional AFM.

If the sample is moved slowly enough such that the cantilever is at equilibrium at each moved position, F_z can be computed by measuring ζ with the relation:

$$F_z = k_c \zeta. \tag{3.1}$$

Instead of a laser interferometry-type deflection detection system, ζ is measured by a Wheastone bridge-based deflection measurement electronics in our system as shown in Figure 3.3 since a piezoresistive cantilever (Park Scientific Instruments Co.) [23], [79] is used where the overall home-made AFM system photo is given in Figure 3.4. It is a Si cantilever that exhibits piezoresistive effect [14] such that when the cantilever is stressed by any external force, the resistance of the cantilever changes. Thus, the output of the bridge is a voltage difference V_{out}, and the nanometer value of the $\zeta(t)$ is computed from the below equation:

$$\zeta(t) = SG_2(G_1 V_{out}(t) + V_{off}), \tag{3.2}$$

where $G_1 = G_2 = 100$ are the amplification gains, V_{off} is the offset voltage which is needed when there is an offset depending on the different resistance values of the cantilevers, V_0 is the bridge voltage, and S is the constant scaling ratio which is calibrated experimentally for each cantilever previously. For the calibration, the cantilever

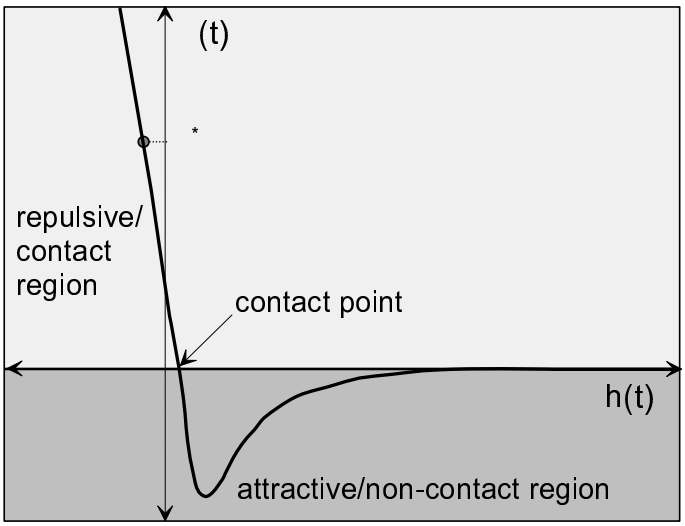

Figure 3.2: The typical cantilever deflection, i.e. interatomic force, and tip-sample distance relation.

is bended in the linear contact region by a hard surface such as Si with a controlled stage experimentally. Getting the slope of the line, S is computed as shown in Figure 3.1.

3.2 Visual Sensing in Micro/Nano World

3.2.1 Micro Vision Sensor: Optical Microscope

A reflecting light-type Optical Microscope (OM) (Olympus Co.) is used as the top-view vision sensor. Its specifications are given in Table 3.1. A color camera (Sony Co.) on the OM is connected to a Matrox Co. Meteor frame-grabber (Meteor II) which enables real-time color image viewing of the micro world on the PC screen with the range of 640×480 pixels in the image frame, (x_p, y_p), and approximately $57 \times 45 \mu m^2$ in the world coordinates, $(x_{\mu m}, y_{\mu m})$. Hereafter, the world coordinates mean the coordinate frame for the AFM positioner x-y motion space. An example display for the real-time OM images is given in Figure 3.6. In the case of linear mapping between both spaces, $x_{\mu m} = \alpha_x x_p$ and $y_{\mu m} = \alpha_y y_p$ where $\alpha_x = \alpha_y \approx 95 nm/pixel$ are constant x and y scaling constants. However, during the experiments, it is observed that there is also some rotaion in the coordinates due to the orientations of the camera, stage and sample surface. Therefore, a calibration process is needed before the experiments in order to map (x_p, y_p) to $(x_{\mu m}, y_{\mu m})$ which is explained later.

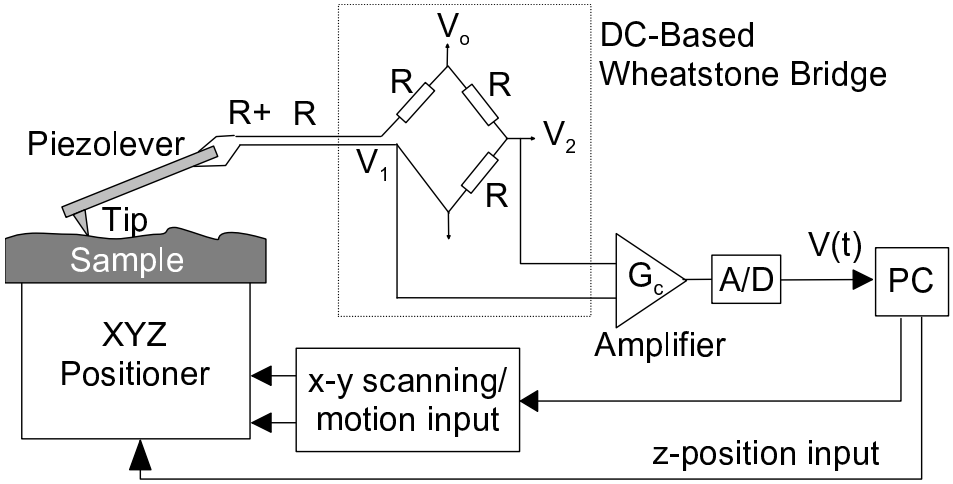

Figure 3.3: AFM with piezoresistive cantilever (PSI Co.^{TM}) and electronic detection system.

working distance	$25mm$
maximum resolution	$\approx$ $500nm$
image resolution	$\approx$ $95nm/pixel$
lens magnification	$\times 80$
lens numerical aperture	0.5
overall magnification	$\times 5000$ (on monitor)
base stand	5DOF (manual)

Table 3.1: Optical Microscope specifications.

3.2.2 Nano Scale 3-D Imaging using AFM

AFM is convetionally used for getting 3-D atomic resolution topology images. There are mainly two types of AFM imaging: *contact* and *non-contact* mode imaging.

Contact Imaging

The AFM hardware for contact imaging is the same as in Figure 3.3. Controlling the z-motion such that cantilever deflection reaches a reference value ζ^* in the contact region as shown in Figure 3.2, the relative z-motion corresponds to the height at that (x,y) point. Scanning all (x,y) points in a rectangular region, and tracking ζ^*, topology data can be held. This method is called contact imaging. An example contact image of our home-made AFM is given in Figure 3.7. Furthermore, another example of an

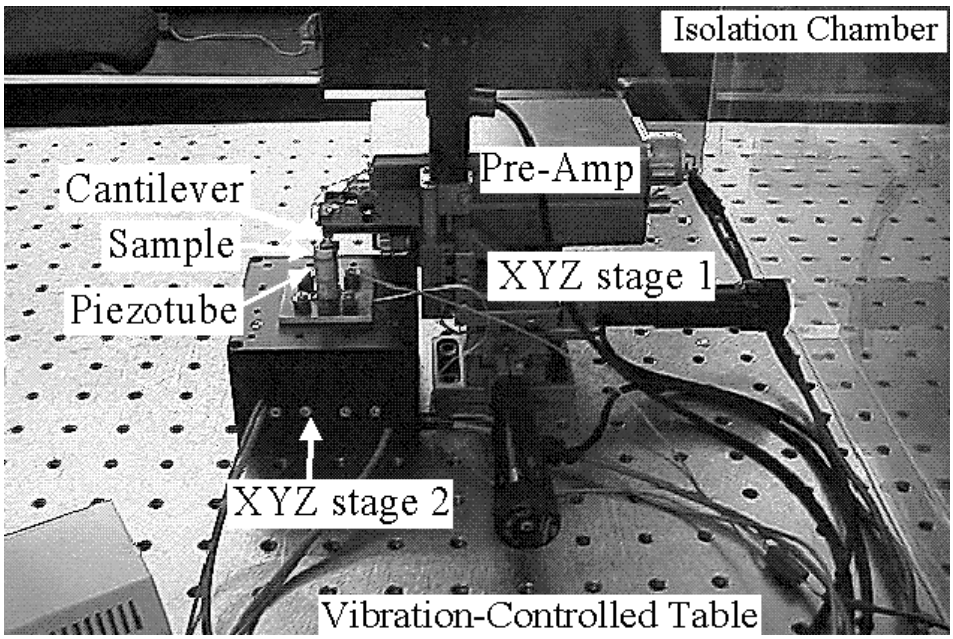

Figure 3.4: Home-made AFM setup.

atomic resolution AFM contact image data of the mica surface held by a commercial AFM in our laboratory is given in Figure 3.8. The problems of this kind of imaging are:

- large lateral frictional forces during xy-scanning which can destroy, change, or move soft or not well immobilized samples,
- high applied normal load to sample.

Especially for biological samples, contact mode may not give stable images due to above problems. But for well-fixed hard samples such as mica, Si or graphite this mode can give the best atomic resolution images. The z resolution can go down to 0.01 nm, but xy-resolution is worse (approx. 0.1 nm at best) due to the finite size of the tip radius.

Non-Contact Imaging

In the non-contact mode, the cantilever is vibrated with a sinus wave generator using a piezoelectric bimorph kind of actuator with known amplitude A and frequency f, which is a little smaller or larger then the cantilever resonance frequency f_r, above the sample at the non-contact region. The home-made hardware constructed for this kind of imaging is given in Figure 3.9. There are two types of non-contact imaging: *non-contact* and *intermittent contact (tapping)* modes. At the former, the cantilever

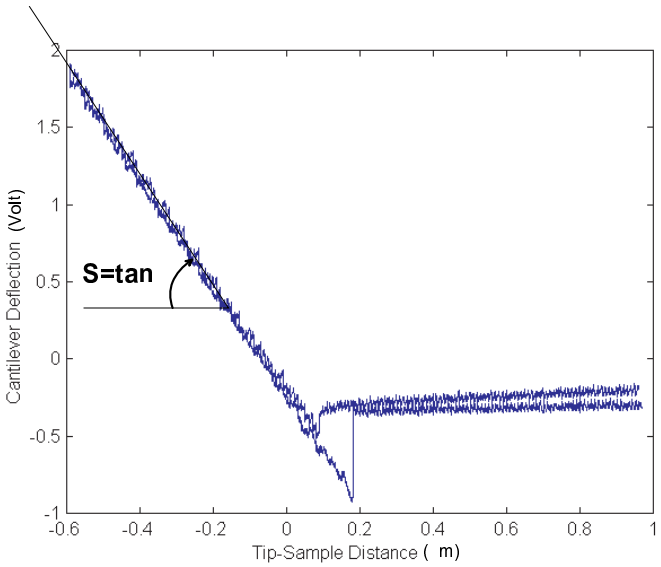

Figure 3.5: Calibration of the parameter S which scales the $Volt$ deflection values to nm.

is located above the sample around few nanometers in the attractive region without touching to the sample, and also vibrated with few nanometers amplitude. In the latter one, the cantilever is located approximately $10 - 100$ nm above, and vibrated with a large amplitude $20 - 200$ nm around f_r. In this case, the tip switches between non-contact and contact with the sample. But the contacts are instantenous, and therefore the applied load and lateral scanning force is rather smaller than the contact imaging mode.

In both modes, A and f is changed due to the interatomic force gradient, and detecting these changes using lock-in-amplifier, frequency demodulation kind of electronic circuits, the change in amplitude ΔA, frequency Δf, and even phase $\Delta\phi$ can be measured. Observing again constant effects, 3-D topology images can be held. As an example of the change in the amplitude of the cantilever vibration depending on the tip-sample distance $h(t)$ can be seen in Figure 3.10 for the tapping mode imaging case ($A = 100$ nm, $f = 133.4$ KHz, $f_r = 133.5$ KHz). Also an example tapping mode image of a particle is given in Figure 3.11.

Non-contact imaging is difficult to realize in ambient conditions. Because, the humidity results in a water layer on samples, and when the cantilever is vibrated very close to surface, the cantilever can easily jump to contact due the hydration/capillary forces. Thus, this mode is prefarable in vacuum or controlled humidity environments. It has the advantage of not deforming the object, and not applying any load. Thus, for biological or not well-fixed samples it is advantegous to use this mode by careful

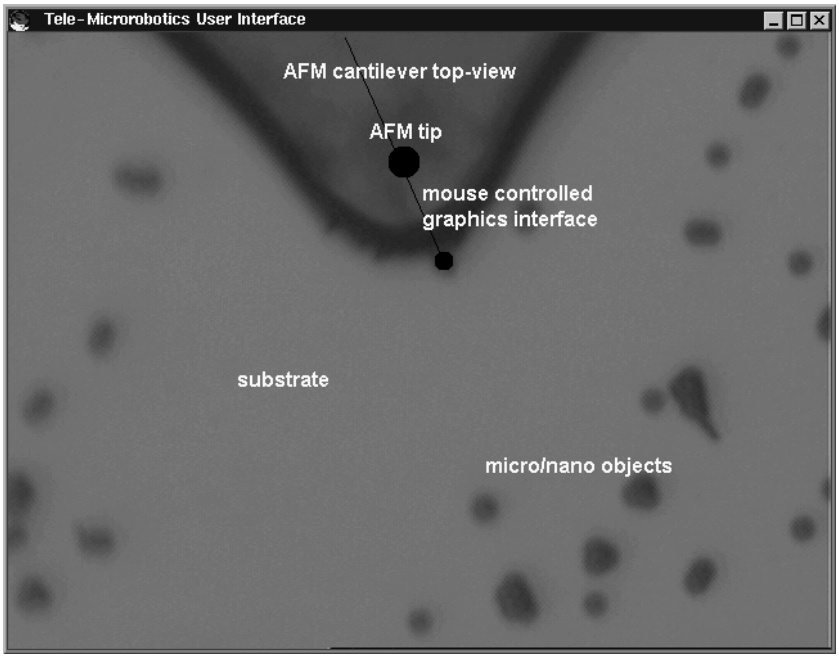

Figure 3.6: Example top-view OM images during micro scale imaging of the cantilever and micro/nano objects where this image is used in micro object manipulation as an user interface by the mouse cursor clicks.

setting. On the other hand, the tapping mode is advantegous such that it can use the advantages of both contact and non-contact modes. Even there is water layer on the sample, there is almost no jump-in-contact problem due to the large A (large vibration energy). There is some applied load and lateral force on the sample with compared to the non-contact mode. However, this effect can be neglected with respect to the contact mode.

For the manipulation applications, the nano objects to be manipulated are designed not to be firmly fixed on the substrate, and contact-type of scanning can move the objects. Therefore, during imaging, non-contact AFM imaging is required. However, since our system is assumed to work in ambient conditions with relative high humidity, tapping mode is preferred. Thus, our strategy is: **imaging in the tapping mode and manipulation in the contact-mode**.

3.3 Micro/Nano Force Sensing

Denoting the deflections along the x, y and z axes as ζ_x, ζ_y and ζ_z respectively as shown in Figure 3.12, the deflection vector is defined as $\zeta = [\zeta_x \ \zeta_y \ \zeta_z]^T$. Taking the

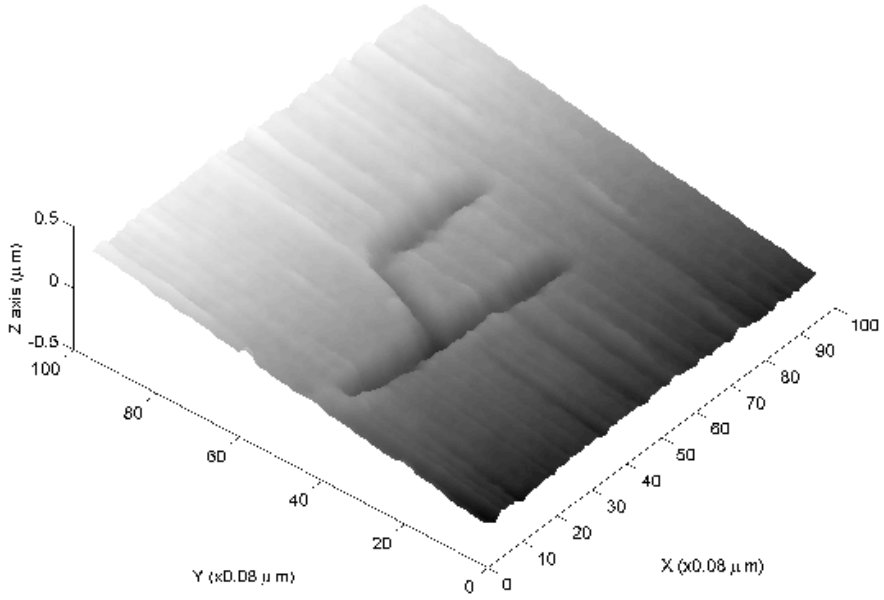

Figure 3.7: Contact type image of FIB drilled Si '4' (8 $\mu m \times 8\ \mu m \times 1\ \mu m$ image size; 0.2 μm maximum drilled height).

force vector as $\mathbf{F} = [F_x\ F_y\ F_z]^T$, and assuming the cantilever with the normal stiffness of k_c is tilted by an angle of α along the x-axis, the deflection is determined by the forces as follows [13]:

$$\begin{aligned} \zeta &= \mathbf{CF} \\ \mathbf{C} &= \frac{1}{k_c}\begin{bmatrix} c_1 & 0 & 0 \\ 0 & c_2 & c_3 \\ 0 & c_3 & 1 \end{bmatrix} \end{aligned} \tag{3.3}$$

where $c_1 = 2L_z^2/L_y^2 + t_c^2/L_x^2$, $c_2 = 3L_z^2/L_y^2$, $c_3 = 3L_z/(2L_y)$, L_x, $L_y and\ L_z$ are the cantilever lengths along the x-y-z axes, and t_c is the cantilever thickness. Thus, the important point is, the cantilever cannot be modeled as three decoupled springs for an accurate modeling where y and z axes are coupled. Using our piezoresistive deflection measurement system, only ζ_z can be measured (also ζ_x can be measured if the optical detection method is utilized which is our future work). Then, the measured deflection corresponds to:

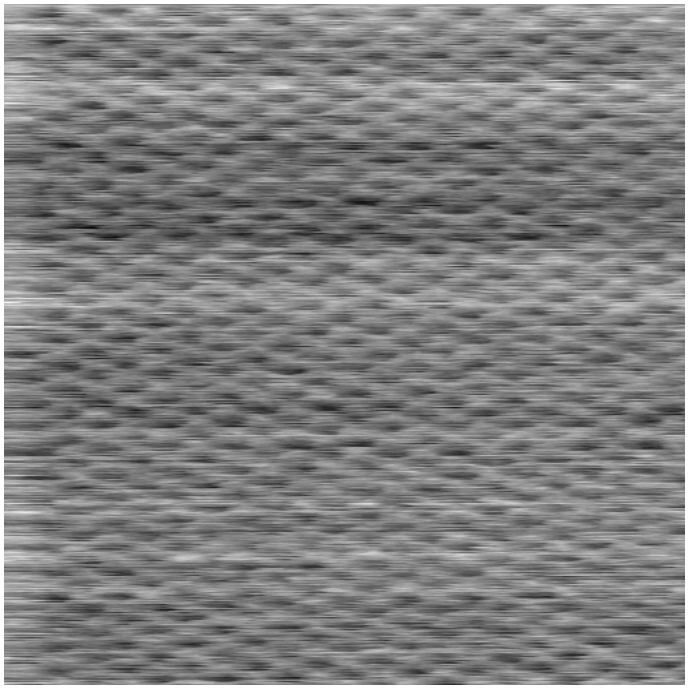

Figure 3.8: Contact type atomic resolution AFM image of mica atoms ($8 \times 8\ nm^2$ image size) using the JEOL Co. JSPM-4200 AFM in ambient conditions.

$$\zeta_z = (c_3 F_y + F_z)/k_c \ . \tag{3.4}$$

Thus, the lateral force of F_y has also affect on ζ_z. Assuming the change of the normal force is negligible during the pushing operation, the change in F_y, i.e. ΔF_y, can be computed as:

$$\Delta F_y = k_c \Delta \zeta_z / c_3 \ . \tag{3.5}$$

This means that the F_y frictional force component corresponding to the applied pushing load can be observed from ζ_z directly.

3.4 Manipulation Tool

AFM is also utilized as the simple push, pull, cut, and etc. kind of manipulation tool in the contact mode. The piezoresistive cantilever (Park Scientific Instruments Co.) has the sharp tip with $3 - 4\ \mu m$ height, and $20 - 30\ nm$ tip apex radius as shown in Figure 3.13 where it is at the bottom side of the cantilver as can be seen in Figure 3.14.

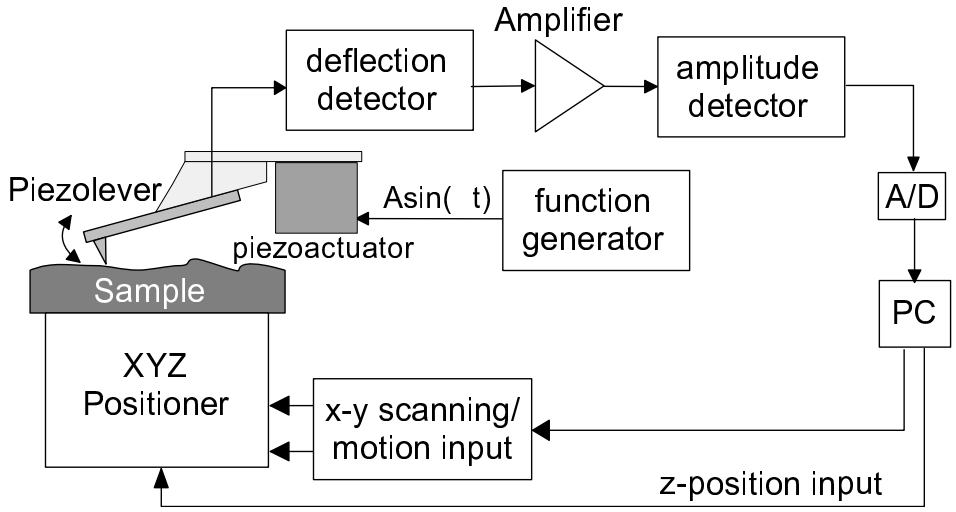

Figure 3.9: Home-made non-contact imaging hardware.

3.4.1 Manipulator Dynamics Modeling

Modeling of the cantilever and nano force dynamics is essential for reliable manipulation control. In the case of approaching and retracting from a flat surface in air, cantilever dynamics can be modeled as a simple mass-spring system as shown in Figure 3.15 with effective mass $m_c = k_c/(4\pi^2 f_r^2)$, damping $b_c = \pi f_r/Q_c$ (Q_c is the quality factor of the cantilever in air), and stiffness k_c such that during approaching and retracting from a sample surface

$$\begin{aligned} & m_c\ddot{h}(t) + 2m_c b_c(\dot{h}(t) + \dot{z}(t)) + k_c(h(t) + z(t) - L) \\ = & \begin{cases} F_{non-con}(h(t)) - B_0^l \dot{h}(t) u(h(t) - L_l), & h(t) > a_0 \\ F_{con}(h(t)) - B_0^s \dot{h}(t), & h(t) \leq a_0 \end{cases} \end{aligned} \tag{3.6}$$

where $F_{non-con}(t)$ and $F_{con}(t)$ are the non-contact and contact tip-sample interaction forces, $h(t)$ is the tip-sample distance, $z(t)$ is the tip-position from the initial rest point, L is the tip-sample initial rest distance, $B_0^l \approx \pi\tau_l R_c(a_0 - h(t))/L_l$ is the liquid-layer damping, $B_0^s \approx \pi\tau_s R_c(a_0 - h(t))/L_s$ is the sample damping, R_c is the cantilever tip radius, the function $u(x)$ is equals to 0 if $x < 0$ and to 1 else, τ_l and τ_s are the viscosity constants and L_l and L_s are the thicknesses of the liquid layer and sample respectively, and $a_0 = 30^{-1/6}\sigma$ is the contact point where σ is the interatomic distance. Here, the cantilever deflection $\zeta(t)$ which is the experimentally measured quantity is defined as $\zeta(t) = h(t) + z(t) - L$.

3.4.2 Manipulation Tasks

Using an AFM cantilever, manipulation tasks as shown in Figure 3.16. Due to its mechanical principle, only mechanical manipulation tasks such as push/pulling, cutting, point-touching, indenting and drilling can be realized. However, by adding some other biochemicals such as enzymes [17], more chemical manipulations can also be realized. In this thesis, pushing/pulling and point-touching tasks will be focused on, and the other task applications are direct with the proposed system and methods.

3.5 Nano Scale Precision Position Control

Piezoelectric XYZ actuators are utilized for atomic resolution positioning. These actuators have hystheresis and drift problems depending on the motion duration and range, and temperature changes. For imaging, since xy motion consists of scanning with specified range, actuators can be calibrated off-line using laser interferometry, and these calibration data are then can be used for accurate scanning (in the case of commercial AFMs). However, in manipulation tasks, the tip moves on arbitrary points in a given range; thus, open-loop control is almost not reliable. Therefore, the best is to integrate high resolution sensors such as capacitive, strain gauge, LVDT (Linear Variable Differential Transformer), or optical sensors to motion axes for closed-loop control. In our system, a Physick Instrumente Co. XYZ closed-loop stage with 10 nm resolution using LVDT sensors at each axis, 0.1% hystheresis error and 100 μm range in all axes is utilized. The dynamics of the stage along the y-axis can be given as [29]:

$$\frac{1}{\omega_y^2}\ddot{y}_s + \frac{1}{\omega_y Q_y}\dot{y}_s + y_s = \tau_y - f_{as} \ , \tag{3.7}$$

where $\omega_y = 2\pi f_y$, $f_y = \sqrt{k_y/m_s}/(2\pi) = 250\ Hz$ is the y-stage resonant frequency with m_s and k_y are the stage and sample total mass and k_y is the y-axis stage stiffness, $Q_y = 20$ is the amplification factor, y_s denotes the sample y-axis position, and τ_y is the stage driving force. The same equation and values are valid for x and z axes with the only change of $f_z = 400\ Hz$.

For the manipulation of the particles and initial settings, three different stages are utilized. Their specifications are given in Table 3.2. The fine positioning XYZ piezoelectric stage (Physick Instrumente Co., P-762.3L) is utilized during the automatic particle assembly control. The controller for the stage uses analog PI controller with a previously calibrated sensor linearization filter circuit for $< 1\ msec$ sampling rate. The microprocessor inside the controller can be used to program the stage, however, since the user-defined position commands are necessary during the manipulation, direct XYZ position references are sent by a 16 bit D/A board from the PC computer. By this way, communication delay almost does not exist. Settling time for xy-axes is 25 $msec$, and

20 $msec$ for the z-axis as can be seen the example settling data of the each stage in Figure 3.17. The peak-to-peak noise is 20 nm which means that the accuracy of each axis is 20 nm. The measured data correspond to the actual positions where the actual position of the each axis is measured from the direct sensor output to the controller PC using a 16 bit 10 $\mu sec/channel$ A/D board. As can be seen from the figure, x-axis has the longest, and most erronous tracking since it is the bottom axis, and has the all weight over it which reduces its resonance frequency and dynamic response.

	Stage I	*Stage II*	*Stage III*
Actuator	piezoelectric	electro-strictive	bearing
Resolution	10 nm/1 nm	40 nm/1.25 μm	10 μm
Range	100 μm	30 μm/18 mm	18 mm
Control	closed-loop/open-loop	open-loop/manual	manual
Hystheresis	$<$ 0.1%/ $<$ 4%	$<$ 4.8%	

Table 3.2: Specifications of the used XYZ stages.

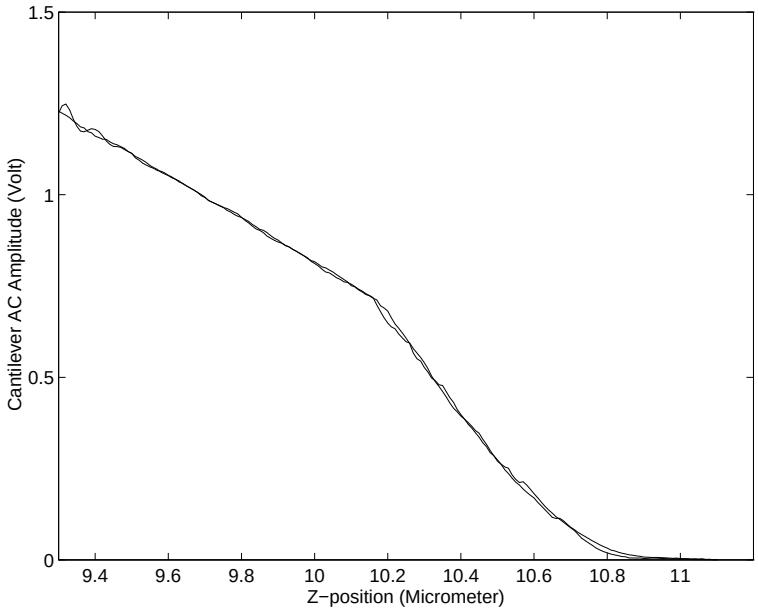

(a)

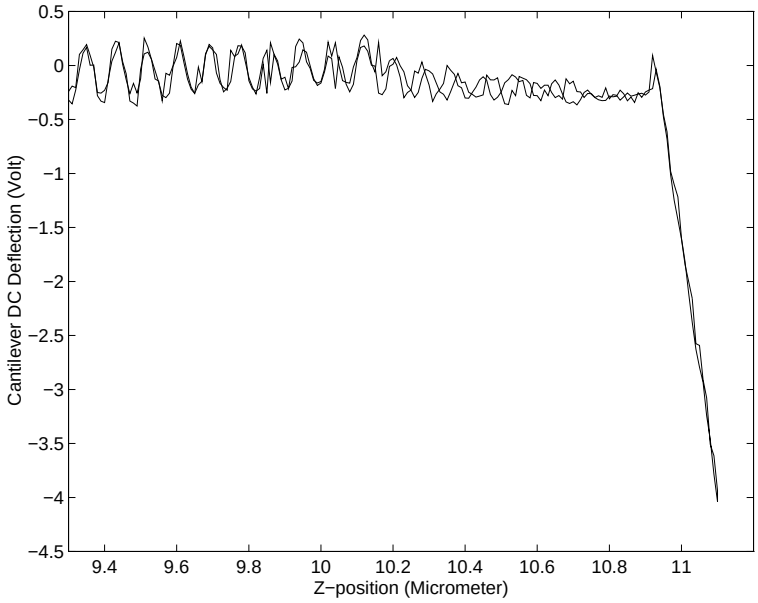

(b)

Figure 3.10: A typical change in (a) the cantilever vibration amplitude, and (b) the DC deflection during tip-sample approach and retraction to a silicon surface at the tapping mode imaging with $A = 100\ nm$ and $f = 133.4\ KHz$ AC excitation.

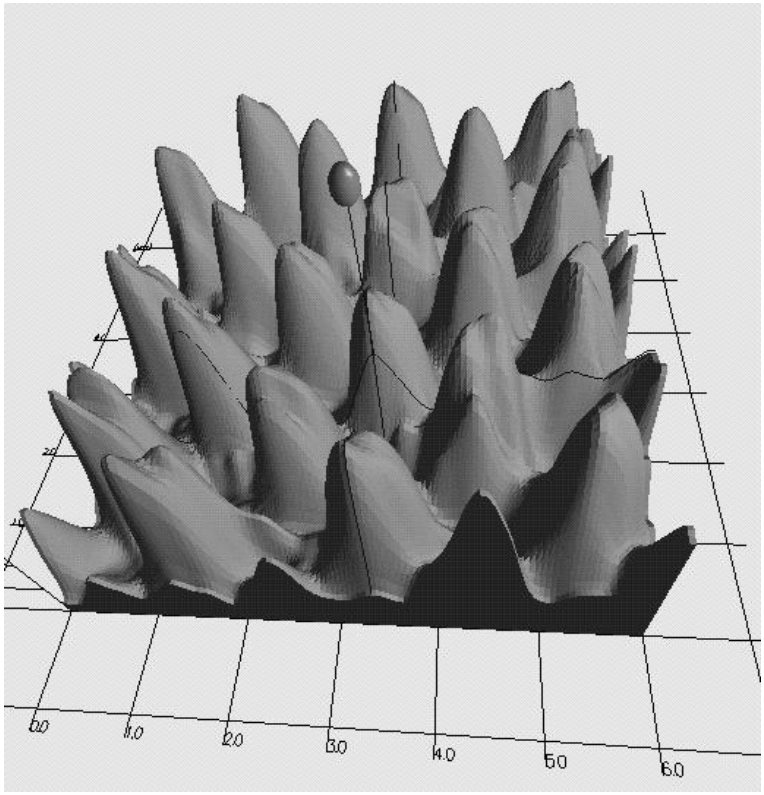

Figure 3.11: 3-D display of the tapping mode image of the silicon conical structures with 300 nm height (sample size is 6×6 μm^2).

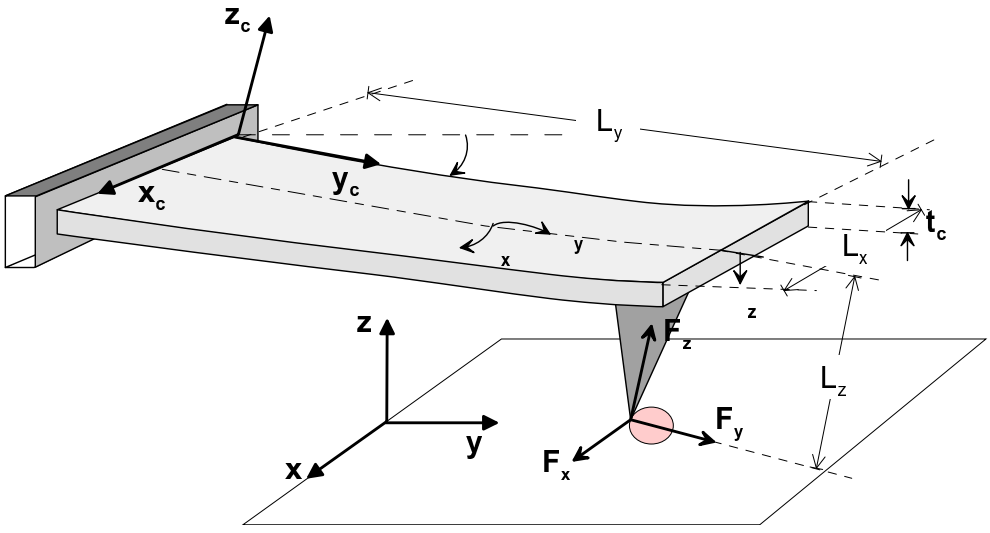

Figure 3.12: Cantilever bending along x-y-z axes during pushing nano objects.

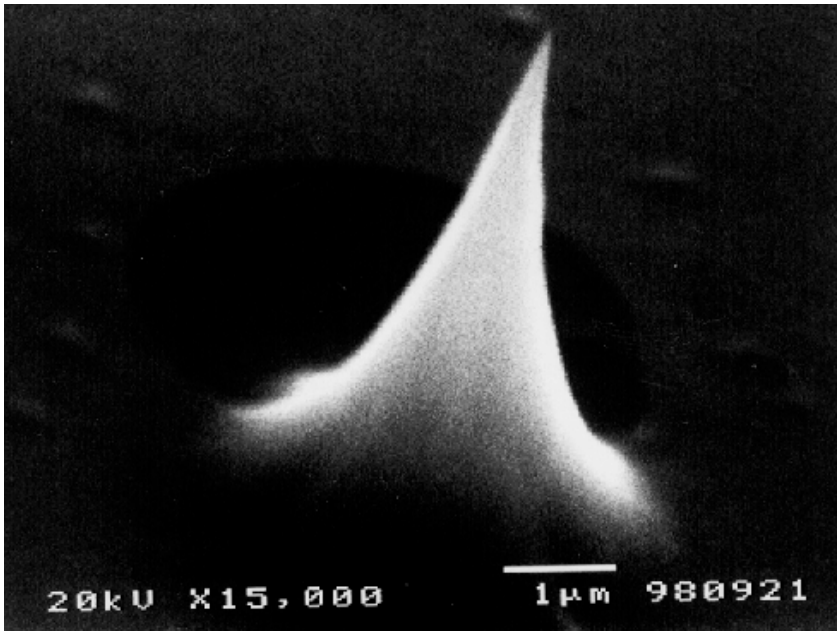

Figure 3.13: SEM photo of the Si piezolever tip with radius approximately $20 - 30\ nm$ (PSI Co.).

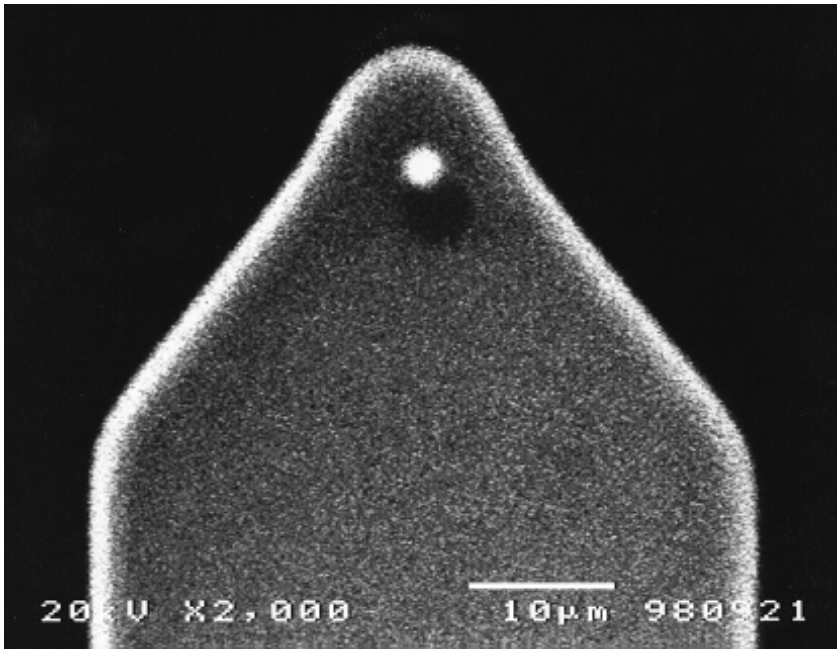

Figure 3.14: SEM photo of the head of the cantilever where the tip is at its bottom side and approximately 10 μm inside.

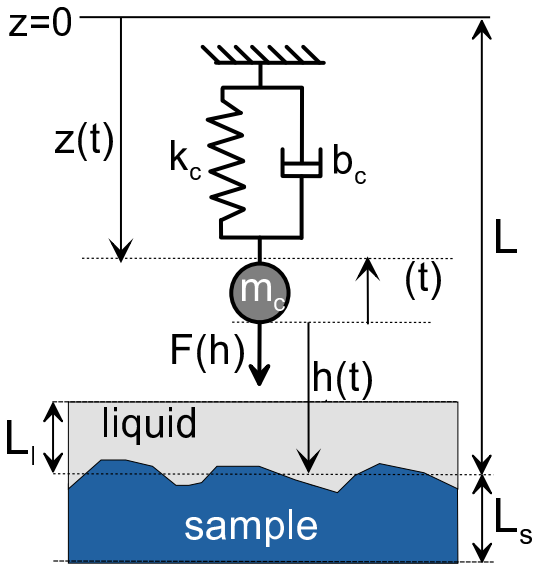

Figure 3.15: AFM cantilever model as a simple harmonic oscillator.

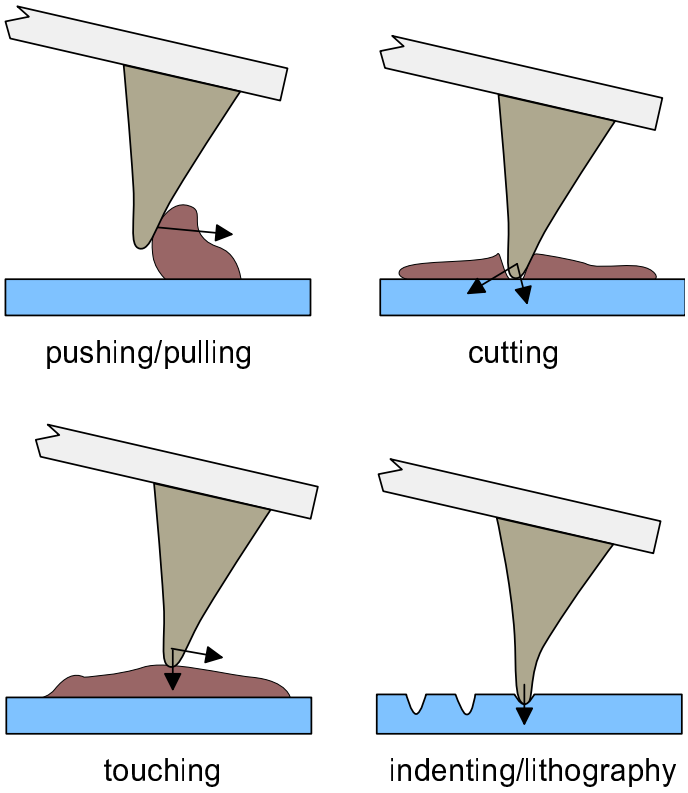

Figure 3.16: Possible mechanical manipulation tasks using one AFM cantilever.

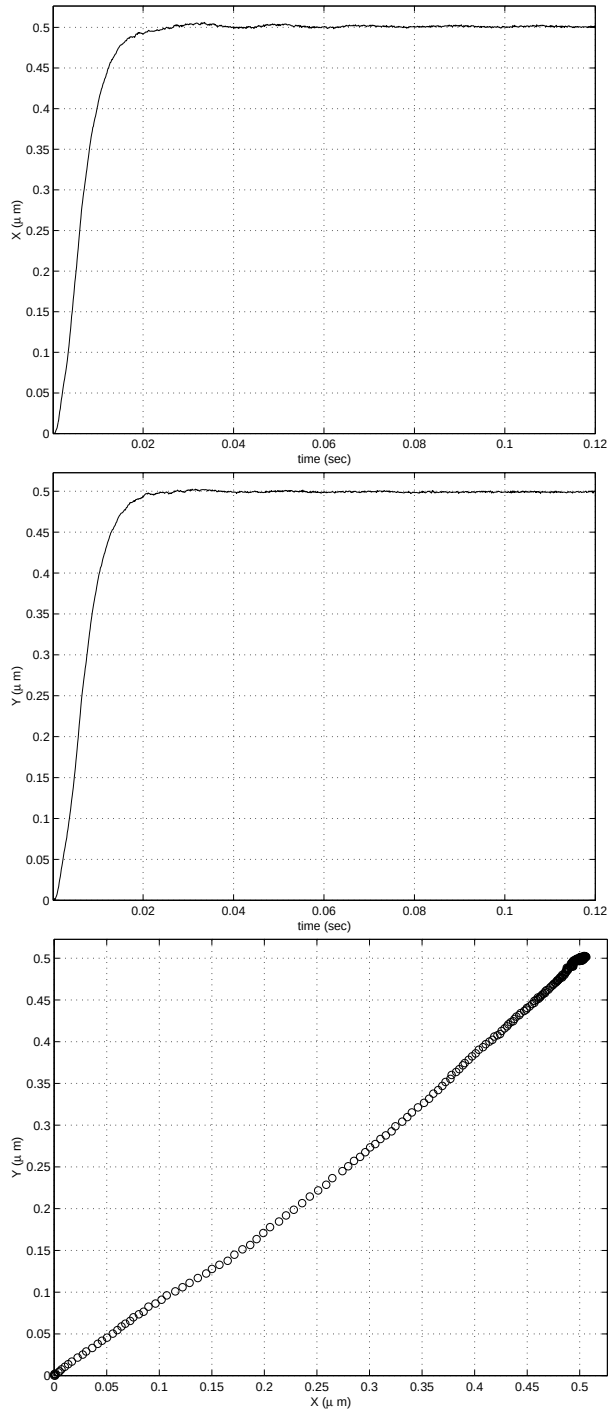

Figure 3.17: Settling data of the xy-axes of the piezoelectric stage with LVDT sensors for a motion from the (0,0) point to $(0.5\mu m, 0.5\mu m)$ position where the linearity and simultaneity of the xy-trajectory is important for xy-pushing of micro/nano objects.

Chapter 4

System Part II: Macro World

The overall setup of the VR-based visual and force display user interface and its photo are shown in Figure 4.1 and Figure 4.2 respectively.

4.1 Visual Display

Real-time and interactive visual feedback from the micro/nano world which gives information about surface roughness, shape, texture, and etc. is essential besides of haptic feedback. Since AFM can measure the 3-D topology, this information can be presented to the user in a friendly way.

Conventionally, AFM data are presented off-line or on-line as 2-D intensity images as can be seen in Figure 4.4; however, VR graphics technology has been used for generating sample images in 3-D [32]. An example of 3-D images generated using OpenGL software environment is shown in Figure 4.5 [31] This image can be rotated or zoomed in any direction, and can be presented in 3-D to the user using a stereo glass, or a head mounted display. On the other hand, depending on the samples such as separate objects on flat surfaces, 2-D image is more helpful for easy interpretation; therefore, 2-D display is also used during manipulation. Furthermore, captured OM top-view images are displayed in real-time for rough imaging of the samples and the AFM cantilever.

Nano Visulator

Nano Visulator provides the Virtual Reality 3-D graphics of the AFM topology image and AFM tip position in real-time. As shown in Figure 4.3, AFM gets the height data z at each Δx, Δy steps during scanning the sample along xy-axes. At each $(i\Delta x, j\Delta y)$ point, the position vector r_{ij} is held as follows:

$$r_{ij} = (i\Delta x, j\Delta y, z_{ij}) \tag{4.1}$$

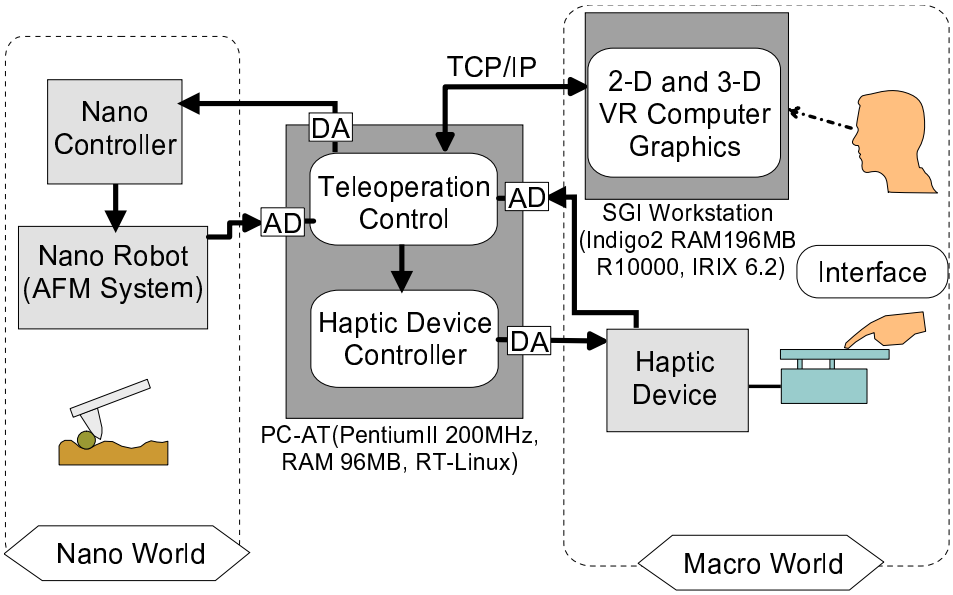

Figure 4.1: Virtual Reality-based user interface system structure.

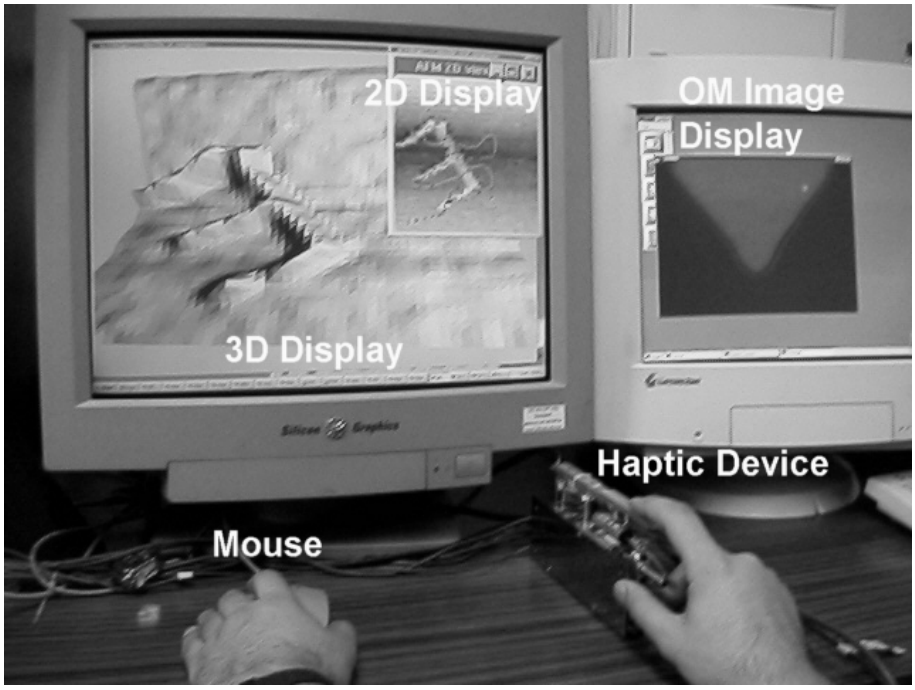

Figure 4.2: Constructed Human-Machine Interface for teleoperated nano manipulation with visual and force displays.

where $i = 0, \ldots, (SizeX - 1)$ and $j = 0, \ldots, (SizeY - 1)$, $SizeX$ and $SizeY$ are the maximum scanning sizes along x and y-axes respectively, and z_{ij} is the sample height at $(i\Delta x, j\Delta y)$. Δx and Δy are normally taken as the same. Furthermore, $\hat{z}_{ij}$ is normalized in the range such that $\hat{z}_{ij} \in [0, 1]$ by $\hat{z}_{ij} = (z_{ij} - z_{ij}^{min})/(z_{ij}^{max} - z_{ij}^{min})$ where z_{ij}^{max} and z_{ij}^{min} are the maximum and minumum height data respectively.

When transforming the acquired data to the 3D graphics data, the scaling parameters, α_{xy} and α_z along the XY directions and Z direction respectively are calculated as following:

$$\alpha_{xy} = \frac{xy_{range}}{Max\{SizeX\Delta x, SizeY\Delta y\}} \tag{4.2}$$

$$\alpha_z = \frac{z_{range}}{\Delta z} \tag{4.3}$$

where $\Delta z = z_{ij}^{max} - z_{ij}^{min}$, xy_{range} and z_{range} are the drawing range corresponding to the graphics coordinates of x-y axis and z-axis respectively, and are initialized as 3.0 and 1.0, then the graphics is drawn in the range $3.0 \times 3.0 \times 1.0$. These values are changable to any value by the operator, thus the magnification and the reduction can be done at the x-y-axes and z-axis independently.

This graphics is drawn by using the OpenGL software library to have the common use on the Silicon Graphics Workstation. The sample surface color, light source position are in accordance with eye position. The example of this graphics is shown in Figure 4.5 and Figure 4.6.

4.2 Force Display: Master/Haptic Device

For feeling the interatomic force normal to the AFM tip (frictional force feedback is excluded in this study), a home-made 1-DOF master device as shown in Figure 4.7 is constructed [28]. It consists of a linear motor which can be modeled as simple DC motors with the transfer function:

$$C(s) = \frac{X(s)}{E_a(s)} = \frac{K_m K_p}{s(T_m s + 1)} \tag{4.4}$$

where X is the displacement of the motor shaft, E_a is the applied armature voltage. The parameters and properties of the device is given in Table 4.1. Using a proportional controller with constant $G = 10000$, the closed loop transfer function becomes as

$$M(s) = \frac{C(s)G}{1 + C(s)G} = \frac{a^2}{s^2 + bs + a^2} \tag{4.5}$$

where $b = 1/T_m$ and $a^2 = GK_mK_p/T_m$.

$Bandwidth$	$\simeq 30Hz$	$Range$	$20mm$
$Friction$	$\pm 3.15mNm$	K_p	2.79×10^{-5}
K_m	$29.41(rad/sec)/V$	T_m	$0.0011sec$

Table 4.1: Properties and parameters of the haptic device.

Operator puts his/her hand to the master arm, applies the normal force $F_{op}(t)$ to the arm tip, and meanwhile feels the arm motion, $x_m(t)$. There is no power transmission from operator to the master arm; the arm moves by motor control every time in accordance with the operator force.

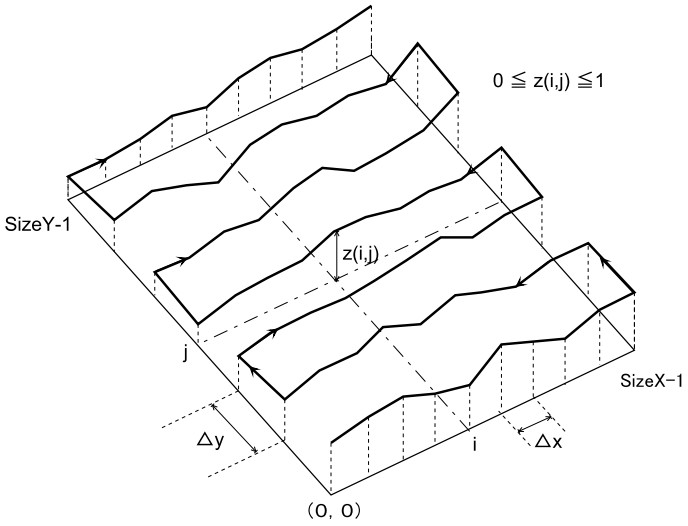

Figure 4.3: Scanning direction of the AFM and the acquired data.

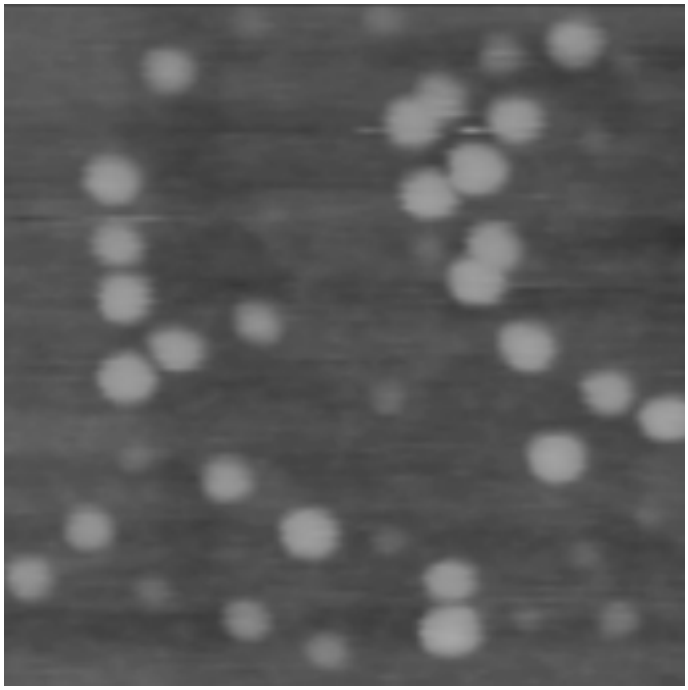

Figure 4.4: 2-D grey-scale display of the AFM image of the 10 nm size InAs quantum dots.

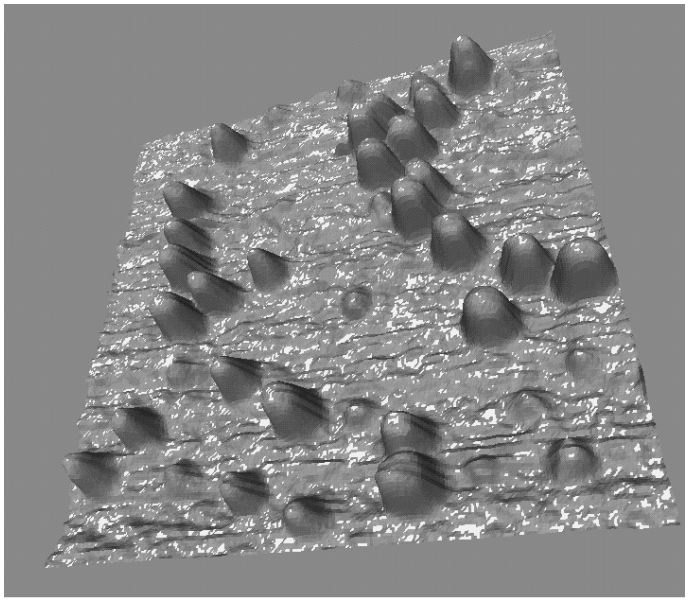

Figure 4.5: 3-D virtual reality graphics display of the AFM image of the 10 nm size InAs quantum dots with a sample size of $150 \times 150 nm^2$.

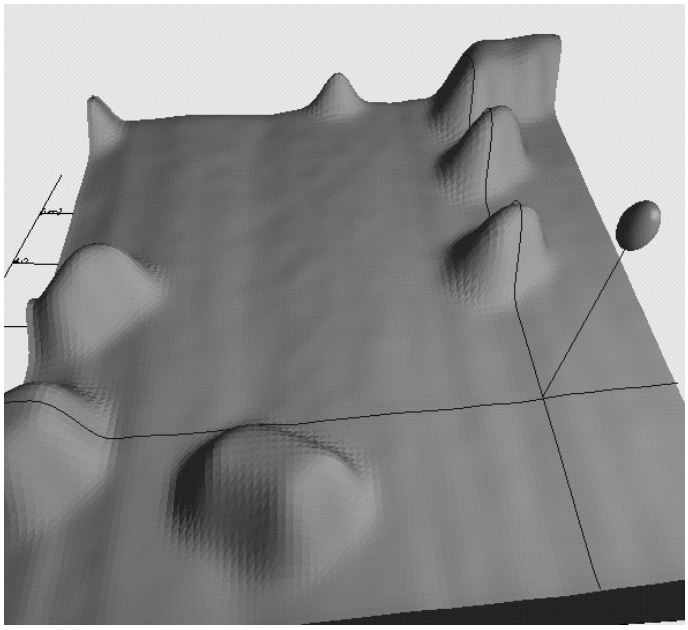

Figure 4.6: VR Nano Visulator 3-D display of 242 nm radius gold-coated latex nanoparticles with the real-time display of the AFM tip as a spherical ball..

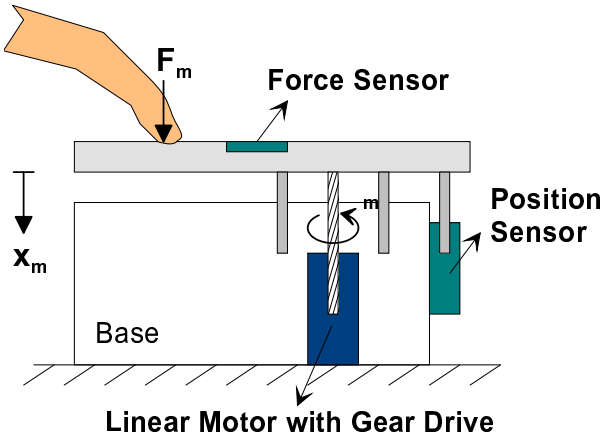

(a)

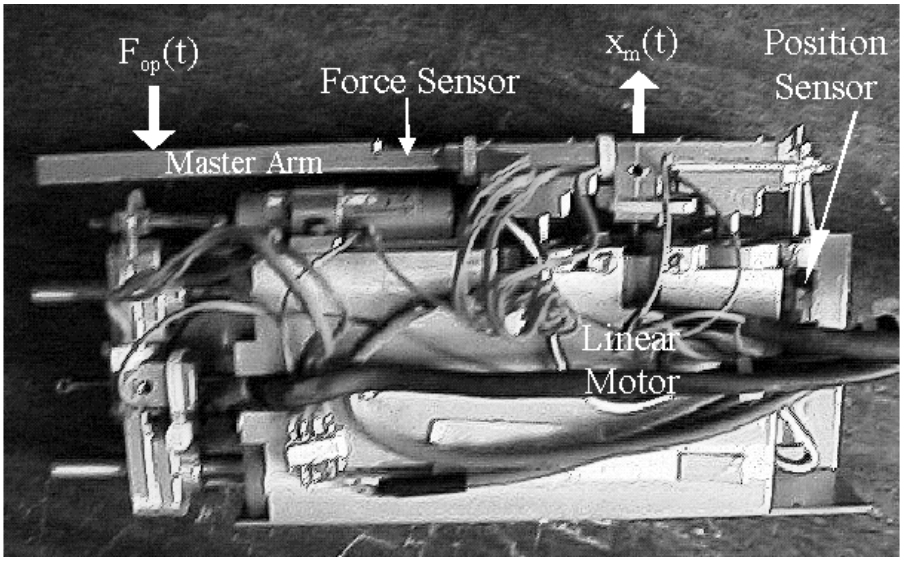

(b)

Figure 4.7: The structure (a) and photo (b) of the home-made 1-DOF haptic device for feeling the scaled interatomic micro/nano forces at the operator's finger.

Chapter 5

System Part III: Macro to Micro/Nano World

5.1 Scaling of the Force and Position Information

For scaling micro/nano forces and positions to the macro world, there are mainly two approaches: *linear* and *nonlinear* scaling. In the former,

$$\begin{aligned} x_s^*(t) &= \alpha_p x_s(t), \\ F_s^*(t) &= \alpha_f F_s(t), \end{aligned} \tag{5.1}$$

where $F_s(t)$ and $x_s(t)$ represent the slave/nano force and position respectively, $F_s^*(t)$ and $x_s^*(t)$ are the scaled values, and α_p and α_f are constant position and force scales respectively. The selection of α_x and α_p depends on the $F_m(t)$ and $x_m(t)$ mechanical and hardware limits. In this type of scaling, all forces are scaled in the same way such that the inertial forces can not be felt.

In the nonlinear scaling which is also called *impedance* scaling [14], forces are scaled independently with respect to their length scaling power relation such that

$$\begin{aligned} x_s^*(t) &= \alpha_p x_s(t), \\ F_s^*(t) &= \alpha_p^4 m_c \ddot{x}_s + \alpha_p^2 b_c \dot{x}_s + \alpha_p^2 k_c x_s, \end{aligned} \tag{5.2}$$

In this approach, the inertial forces can be magnified such that the operator can feel close to its daily experience. But this approach requires precise environment parameters while the linear scaling does not.

5.1.1 Selection of the Scaling Factors

In this thesis, the forces and positions are linearly scaled with parameters α_f and α_p. For determining these parameters, there are different approaches. Recently, Goldfarb [24] concluded two cases: (1) $\alpha_f = 1/\alpha_p = 1/L$ for structurally dominated interactions, (2) $\alpha_f = 1/\alpha_p^2 = 1/L^2$ for surface-dominated interactions where $L = (x_s^{max} - x_s^{min})/(x_m^{max} - x_m^{min})$, and assuming $L >> 1$. Furthermore, we add also a heuristic one where the maximum range and resolution, i.e. performance, of the master and slave motions and forces can be utilized. In this case:

$$\begin{aligned} \alpha_p &= \frac{x_s^{max} - x_s^{min}}{x_m^{max} - x_m^{min}} \\ \alpha_f &= \frac{f_m^{max} - f_m^{min}}{f_s^{max} - f_s^{min}} \ , \end{aligned} \tag{5.3}$$

Upper max and min terms denote the minimum and maximum values for the given parameter. This kind of scaling can be especially useful for micro/nano manipulation cases where the resolution of the stages are limited and environmental disturbances largely reduce the measurement and positioning accuracy.

At first, the measurement limitations should be considered. For the positioning limits, resolution $\delta_p = 10\ nm$ in the closed-loop control case. For the initial height of the tip above the sample contact point H, and a maximum indentation depth δ_{max}, the range $x_s^{max} - x_s^{min} = H + \delta_{max}$. The measurement range of the cantilever deflection is limited by the electronics such that $-10S \leq \zeta \leq 10S$ where S is the conversion term for the deflection from $Volt$ to μm. It is calibrated before the experiments (in our case $S = 0.033\ \mu m/Volt$). Thus, $\delta_{max} \leq 10S = 0.33 \mu m$.

For the micro/nano force measurements, the noise in the cantilever deflection measurement system e_c is peak-to-peak $50\ mV$ which means an approximate force resolution $\delta_f = 0.05 k_c S = 13\ nN$. Since ζ is limited, also $-10k_cS \leq f_s \leq 10k_cS$. For $k_c = 8\ N/m$, $-2.6\ \mu N \leq f_s \leq 2.6\ \mu N$. However, the attractive micro/nano forces are relatively very small with respect to contact forces, and typically $-0.6\ \mu N \leq f_s \leq 2.6\ \mu N$. Furthermore, due to δ_p, minimum ζ steps are limited to $k_c \delta_p = 80\ nN$. Thus, the overall force resolution in the closed-loop control case is $\delta_f = 90\ nN$. On the other hand, for the open-loop control, there is no limitation from δ_p, and $\delta_f = 13\ nN$.

The resolutions and ranges can be combined for determining the possible number of control steps N_f and N_s for the nano force and position control as follows:

$$\begin{aligned} N_p &= \frac{H + \delta_{max}}{\delta_p} \\ N_f &\leq \frac{20 k_c S}{\delta_f} \ . \end{aligned} \tag{5.4}$$

For the values of $\delta_{max} = 0.3\mu m$ and $H = 0.1\mu m$, it is computed that $N_p = 40$ and $N_p = 400$, and $N_f = 58$ and $N_f = 400$ for the case of $\delta_p = 10\ nm$ and $\delta_p = 1\ nm$ respectively. For an accurate control, N_p and N_f should be as large as possible. Therefore, 10 nm resolution may not be enough for precise feedback, and 1 nm resolution should be utilized.

For the master device, the motion range is limited to 2 cm with $\delta_p = 0.004\ cm$. Thus, $N_p = 500$ for the master positioning which could be sufficient. Force measurement resolution is $\delta_f = 0.1\ N$ for the strain gauge sensors, and the maximum measurable range is approximately $\pm 18\ N$. Thus, $N_f \leq 360$. Finally,

$$\begin{aligned} \alpha_p &= \frac{H + \delta_{max}}{2.0}\ (\mu m/cm) \\ \alpha_f &= \frac{f_m^{max} - f_m^{min}}{3.2}\ (N/\mu N)\ . \end{aligned} \tag{5.5}$$

For applying the scaling rules (1) and (2), H, δ_{max}, f_m^{max}or f_m^{min} can be arranged for enabling the scaling rule equalities.

5.2 Bandwidth Effect

If the relative difference between the bandwidths of the force feedback device, f_m, and slave device, f_s, is high, strategies should be introduced for avoiding unstabilities and unreliable force feeling. In the AFM system, x-y scanning bandwidth is around 40-50 Hz in closed-loop while the force feedback device bandwidth is around 30 Hz without any dedicated hardware. Then, one solution is limiting the scanning speed, $v_s(t)$, for feeling the nanometric/atomic features with length ΔL within the haptic device's bandwidth such that

$$v_s(t) \leq \Delta L f_m. \tag{5.6}$$

In the reverse case, where $f_m > f_s$, smoothing strategy such as adding artificial compliancy for intermediate motions can be a solution.

5.3 Hardware Disturbances

The main hardware disturbance sources in an AFM-based tele-nanorobotic system can be classified depending on the system part such as AFM, master device and tele-operation system disturbations. In the AFM system, mechanical vibration in the range of 1 Hz-10 KHz, hysteresis and thermal drift in the piezoelectric positioners, thermal electrical and $1/f$ noise in the piezoresistive AFM cantilever, water layer due to the

humidity in the air, air flow, acoustic pressure, and temperature changes are the main disturbation sources. For reducing acustic and air flow disturbances, an acrylic chamber is designed with double glasses, and a vibration-controlled table is being used in our system. In the haptic device, backlash, sensor error, hysteresis and electrical noises can exist. Additional low-pass filters can reduce the electrical noise. Finally, during teleoperation, time delay can be a significant disturbance especially in distant application cases using the computer network.

5.4 Scaled Bilateral Teleoperation Control

For feeling the scaled nano forces on the human finger, the bilateral teleoperation control system shown in Figure 5.1 is to be constructed.

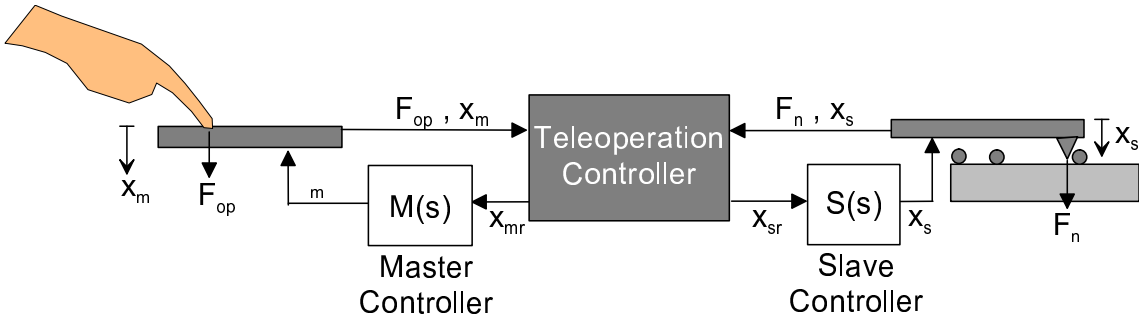

Figure 5.1: Scaled bilateral teleoperation control scheme.

5.4.1 Dynamics Modeling

Force feedback is sensed through the linear motor torque with the master arm (Figure 4.7)dynamics of:

$$m_m \ddot{x}_m + b_m \dot{x}_m = \tau_m + F_m \ , \tag{5.7}$$

with m_m is the arm mass, b_m is the damping ratio, F_m and x_m denote the operator force and arm position, and τ_m is the motor driving torque.

For the slave site, AFM tip base position $x_s(t) = z(t)$ is controlled using the piezoelectric stage. Transformer) integrated sensor is utilized. resolution is limited to 10 nm due to the sensor resolution while in open-loop 1 nm resolution is possible. The dynamics of the stage can be given as:

$$\frac{1}{\omega_n^2}\ddot{x}_s + \frac{1}{\omega_n Q}\dot{x}_s + x_s = \tau_s - F_s \ , \tag{5.8}$$

where $\omega_n = 2\pi f_n$, $f_n = \sqrt{k_s/m_s}/(2\pi) = 450\ Hz$ is the resonant frequency with m_s and k_s are the stage and sample total mass and k_s is the stage stiffness, $Q = 20$ is the amplification factor, x_s denotes the AFM cantilever base position, F_s is the force that the tip applies to the sample, and τ_s is the stage driving force.

The tip-sample interaction dynamics which is given in Eq. 6.9 can be written as:

$$F_s = k_c\zeta = -m_c^*\ddot{\zeta} + k_i x_s - k_i\zeta \ , \tag{5.9}$$

with $x_s = z$. Assuming quasi-static, i.e. slow, motion which means equilibrium at each x_s displacement:

$$F_s = \frac{k_i(x_s,\delta)k_c}{k_i(x_s,\delta) + k_c} x_s \ . \tag{5.10}$$

5.4.2 Ideal Response Definition

The ideal response of the controller is given as follows:

$$\begin{aligned} x_s &\rightarrow \alpha_p x_m \ , \\ F_m &\rightarrow \alpha_f F_s \ , \end{aligned} \tag{5.11}$$

at the steady state. Here $\alpha_f > 0$ and $\alpha_p > 0$ are the force and position scaling factors respectively.

5.4.3 Scaled Bilateral Teleoperation Controller I: Virtual Impedance Control

In order to realize the ideal response, firstly, the bilateral teleoperation system utilizing Virtual Impedance (VI) control approach (Figure 5.2) is proposed. VI is utilized to control the impedance between the master and slave arms for realizing the desired force feedback depending on the task. The basic structure of the VI control-based teleoperation system, and the VI structure is given in Figure 5.3. Thus, VI control transfer function term

$$V(s) = \frac{1}{M_v s^2 + B_v s + K_v} \ , \tag{5.12}$$

generates smooth reference master and slave positions as $x_{mr} = x_{sr}/\alpha_p$ since it also behaves as a second order low-pass filter. $M(s) = X_m(s)/X_{mr}(s)$ (given by the Eq. (4.5)) and $S(s) = X_s(s)/X_{sr}(s)$ are master and slave plant and control transfer functions. K_f is the force error feedback gain. For the simplicity of the analysis, if a spring

is assumed to be attached to the cantilever, i.e. $F_s(s) = KX_s(s)$, following equations are computed for checking the ideal responses:

$$\frac{x_m}{x_s} \approx \frac{1}{\alpha_p}, \tag{5.13}$$

$$\frac{F_m}{F_s} = \frac{K}{\alpha_p K_v K_f} + \alpha_f(1 + \frac{1}{K_f}). \tag{5.14}$$

For enabling the ideal responses, K_f should be selected as large as possible, and K_v should be selected as close as to K.

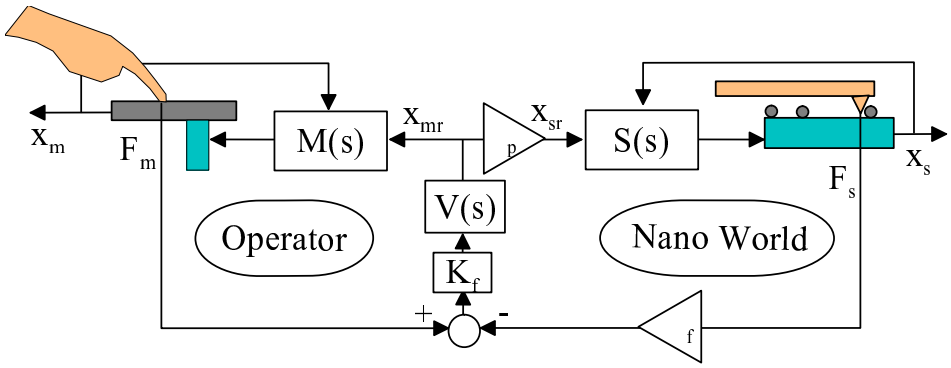

Figure 5.2: Virtual Impedance-based scaled bilateral force feedback control.

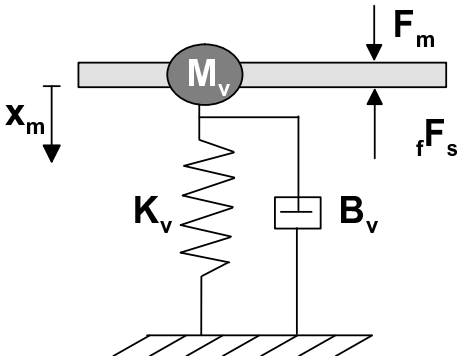

Figure 5.3: Virtual Impedance control structure.

5.4.4 Scaled Bilateral Teleoperation Controller II: Force Reflecting Servo Type Control

Second teleoperation control approach is force-reflecting servo type controller as shown in Figure 5.4. The control laws are as follows:

$$\begin{aligned} \tau_m &= -\alpha_f f_s - K_f(\alpha_f f_s - f_m) \\ \tau_s &= K_v(\alpha_p \dot{x}_m - \dot{x}_s) + K_p(\alpha_p x_m - x_s) \ , \end{aligned} \tag{5.15}$$

K_p and K_v are position control parameters, and K_f is the force error gain. Using the slave and master dynamics equations, and assuming a very hard sample such that $k_i >> k_c$, and $f_s = k_c x_s$, equalities for the ideal response at the steady state are given as follows:

$$\begin{aligned} \frac{x_m}{x_s} &= \frac{1}{\alpha_p}(1 + \frac{1}{K_p}) \\ \frac{F_m}{F_s} &= \frac{1 + K_p}{k_c \alpha_p K_f K_p} + \alpha_f(1 + \frac{1}{K_f}) \ . \end{aligned} \tag{5.16}$$

Thus, for enabling the ideal responses, K_p and K_f should be selected as large as possible.

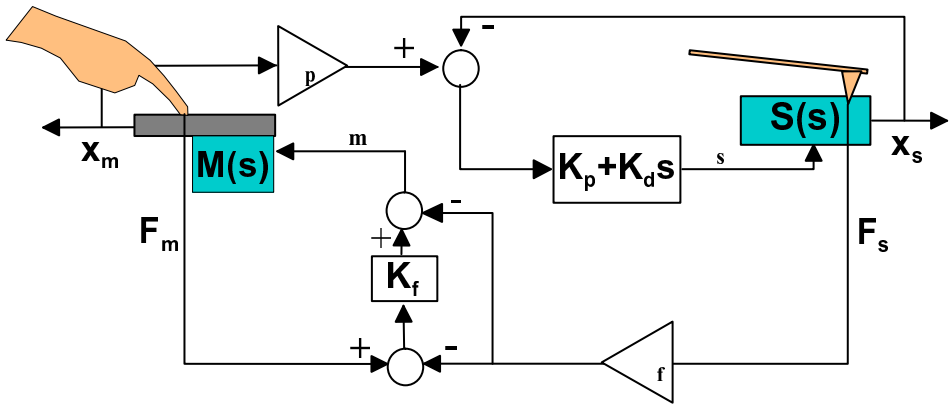

Figure 5.4: Scaled bilateral teleoperation control system.

5.4.5 Stability of the Teleoperation System

At the micro/nano scale teleoperated force feedback control, the dynamics in the micro/nano world can become highly nonlinear and coupled which may cause instability

problems. However, even it is nonlinear, the dynamics can be assumed to be passive, and thus the system stability depends on the proposed controller stability properties. For the controllers, if K_f parameter is selected very large, positioning resolution is not small enough, and the contact interaction is highly stiff, then the instability problem as the vibration of the haptic device can occur. Therefore, the stability analysis of the all system including the proposed interaction force models and positioning stage dynamics at the slave site, which is expected to be mathematically very complex, is necessary, and it is a future work.

Chapter 6

Application I: Tele-Touching to Surfaces at the Micro/Nano Scale

6.1 Introduction

In our daily lives, direct physical interaction/contact with objects such as shaking hands, grasping a glass of water, opening the tap of a bottle, and etc. constitutes one of the important sensings. However, this kind of direct interactions are limited to only macro scale objects where special tools are required for interacting i.e. small (micro/nano) scales. Integration of tele-robotics and micro/nano mechatronics technologies, i.e. tele-micro/nanorobotics technology, enables such tools [67], and this study is focused on teleoperated physical contact interactions with elastically deformable micro/nano scale surfaces. Most of the micro/nano robotics researches does not include the detailed effect of object deformation during contact type of manipulation, and this study also introduces deformation/indentation models for understanding the micro/nano scale contact behaviour in detail.

The main phenomenon at the micro/nano scale is the scaling effect where the gravitational forces become negligible with respect to attractive or repulsive interatomic forces, and sticking forces become dominant. Thus, a different mechanics, which can be called as *micro/nano mechanics*, is introduced by many researchers [10]. One of the main components of this new field is micro/nano contact mechanics [36]. For understanding the contact phenomenon of surface atoms at the micro/nano scale, Surface Force Apparatus and recently Atomic Force Microscopy (AFM) are utilized [8]. AFM can enable single asperity contact studies of any type of samples (biological objects, polymers, metals, semi-conductors, and etc.) where local contact studies with very high resolution has become possible. For AFM-based contact/indentation studies, Hertz [81], [70], [77], [75], [61], DMT, BNC and Maugis-Dugdale (MD) models [9] have been proposed. Hertz model is realistic in the case of large external loads with compared to surface

adhesion. However, load amounts may have similar magnitudes with adhesion forces during micro/nano manipulation tasks, thus this model should not be utilized in the case of small loads. DMT model adds the effect of adhesion to the Hertz model, and it can be used in the case of rigid systems, low adhesion, and small radii of curvature. But it can underestimate the true contact area, and the hystheresis between loading and unloading cannot be modeled with this model. On the other hand, JKR model also includes the effect of adhesion forces and hystheresis behaviour where it is realistic for small loads. But, it assumes that short-ranged surface forces act only inside the contact area, and this may underestimate loading due to the surface forces. Finally, MD model is the recent best model since it is analytical, can be used for any case, and does not underestimate surface forces and contact area.

In this thesis, micro/nano contact mechanics is connected with tele-robotics approach for putting human operators inside the micro/nano world for touching and physically interacting with surfaces at the micro/nano scale. This kind of study is important especially for reliable tele-manipulation of micro/nano deformable surfaces such as biological objects or polymers. This connects micro/nano contact deformation mechanics and teleoperated haptic feedback researches for the first time upon our knowledge. Hollis et al. [30] and Falvo et al. [18] utilized tele-robotics technology for tele-manipulation or tactile feedback, but did not consider the contact mechanics issue.

Our approach is to utilize Hertz, DMT, JKR, and MD deformation models for a Virtual Reality Micro/Nano Touching Simulator using the AFM, and then results are compared with teleoperated AFM tip touching experiments. For the bilateral teleoperation force feedback control, force-reflecting servo-type controller is used. The scaling problem for this kind of application is defined, and possible solutions are proposed.

The organization of the paper is as follows: at first, micro/nano scale contact mechanics is described and possible models are introduced. Then, scaled bilateral teleoperation control and scaling approach are given. Next, Virtual Reality graphics environment for tele-micro/nano-touch simulations is explained. Finally, simulation and experimental results are discussed and reported.

6.2 Problem Definition

AFM cantilever with its sharp tip is replaced by our finger at the micro/nano scale as shown in Figure 6.1. The operations are assumed to be realized in ambient conditions with no direct humidity and temperature control for the AFM system. ere, the sample is assumed to be an elastically deformable flat half-space, and the mass of the cantilever is assumed to be concentrated on the tip apex.

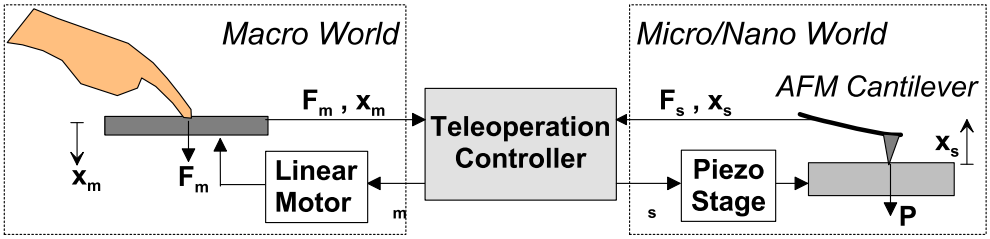

Figure 6.1: Contact-type physical interaction with deformable surfaces at the micro/nano scale using AFM tip as a single asperity contact tool and force/topology sensor.

6.3 Modeling of Non-Contact Forces Between the Tip and Surfaces

Assuming the AFM tip apex is spherial (parabolic), micro/nano forces between a sphere and elastic flat surface is to be modeled for simulating the touch interaction in a VR environment. Since the tip approaches, and then contact, all process of approaching to the surface, then contact mechanics, and finally retracting phases are all investigated.

During approaching and retracting where the tip and surface are not in contact, there are mainly attractive and sometimes repulsive type of non-contact forces exist in air conditions (gravitational forces are negligible relative to other micro/nano forces). These forces are van der Waals, capillary and electrostatic forces such that $F_{non-con}(t) = F_{vdw}(t)+F_{cap}(t)+F_{el}(t)$. At below, these forces are explained in detail. As the notation, the (-) force means the attractive and (+) do repulsive forces.

6.3.1 Van der Waals Forces

It exists for every material in every environmental conditions (like the gravitational force at the macro world), and depends on the object geometry, material type and relative distance. For different geometries, the work functions of W are given in Figure 6.2. Assuming the interaction of the spherical cantilever tip with a flat surface [35],

$$F_{vdw}(h) = -F_0 \frac{\sigma^2}{h^2} \ . \tag{6.1}$$

Here, h is the tip-surface distance, σ is the interatomic distance, $F_0 = \frac{HR_t}{6\sigma^2}$, R_t is the spherical tip radius, and H is the Hamacker constant ($0.4\times10^{-19} < H < 5\times10^{-19}$ for all materials). For the case of a liquid layer on the sample, $H = \{(H_{tip} - H_{liquid})(H_{sample} - H_{liquid})\}^{1/2}$. For example, for a SiO_2 tip and mica sample with a water layer on it

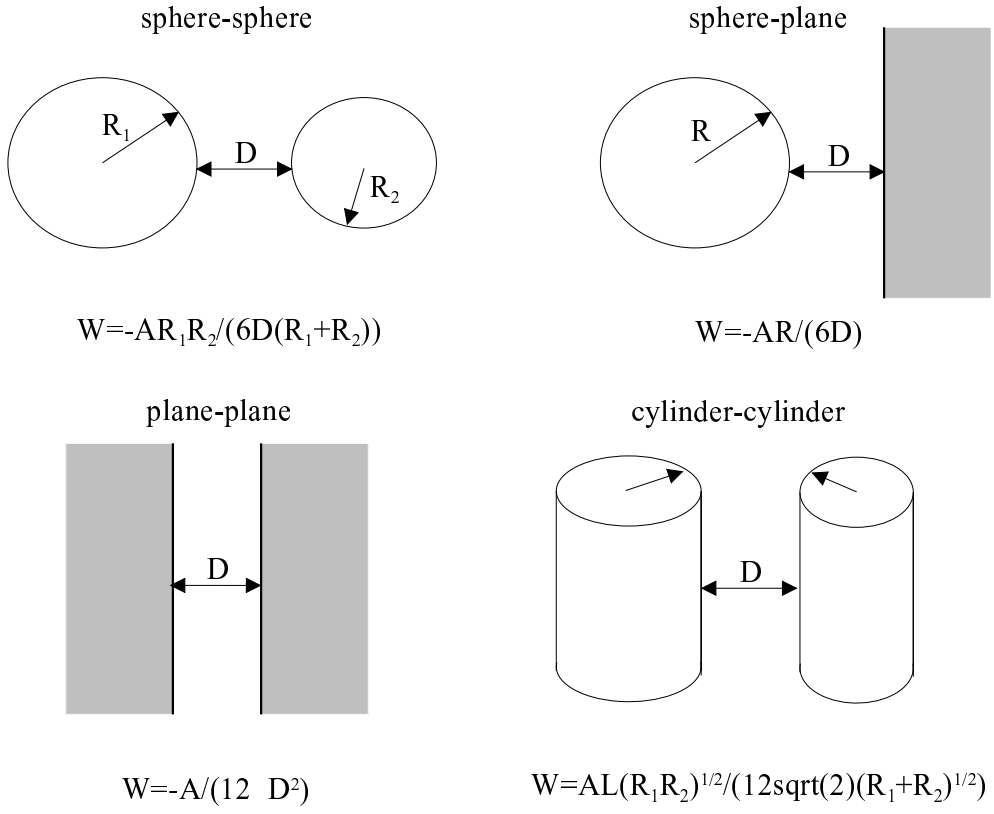

Figure 6.2: Work functions of Van der Waals force for different geometries.

case, $H \approx 1.89 \times 10^{-19} J$ where $H_{SiO_2} \approx 4 \times 10^{-19} J$, $H_{H_2O} = 0.37 \times 10^{-19} J$ and $H_{mica} = 1.35 \times 10^{-19}$.

Approaching to the contact point, F_{vdw} goes to infinity which causes a discontinuity problem. Therefore, Lennard-Jones model can be used for a better continuity such that

$$F_{vdw}(h) = -F_0\Big(\frac{\sigma^2}{h^2} - \frac{\sigma^8}{30h^8}\Big). \tag{6.2}$$

The surface roughness change the magnitude of F_{vdw} such that higher pek-to-peak roughness height b the less the F_{vdw}:

$$F_{vdwb}(h) = \Big(\frac{h}{h + b/2}\Big)F_{vdw}. \tag{6.3}$$

The retardation effect also increases the distance power from 2 to 2.7 or more. Thus, approximately, after 100 nm separation distance, F_{vdw} forces can be negligibly small.

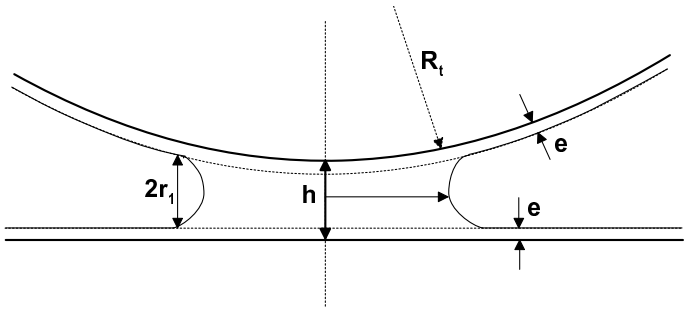

Figure 6.3: Capillary force parameters during a sphere and flat surface contact.

6.3.2 Capillary Forces

The water layer on the surfaces of the probe and the substrate result in an adhesion force. A liquid bridge occurs between the tip and surface at the close contact as shown in Figure 6.3. The parameters of this capillary force are the tip-surface distance h, radii of curvature of the meniscus as r_1 and ρ, and the thickness of the liquid layer e. Using the macroscopic theory of the capillarity theory, following model is held [15]:

$$F_{cap}(h) = \Big[\pi\rho^2\gamma_L\big(\frac{cos\theta}{r_1} + \frac{1}{\rho}\big) + 2\pi\gamma\rho sin\theta + F_{SLS}\Big]u(-h+L)\ , \tag{6.4}$$

where R_t is the tip radius, θ is the contact angle, $u(.)$ is the step function, $L = L_l$ during approaching and $L = \delta$ during retraction where $L_l \approx 2e$ is the thickness of the water layer, and δ is the breaking length of the meniscus which can be determined by the JKR contact mechanics modeling as $\delta = 0.132(6\pi\tilde{R}^{1/2}\gamma_L/K)^{2/3}$ where $1/K = [(1-\nu_t^2)/E_t + (1-\nu_a^2)/E_a]$, and E_t and E_a are the Young modulus, and ν_t and ν_s are the Poison's coefficients of the tip and particle respectively. r_1 can be approximated as $r_1 \approx -0.54/log(P/P_s)(nm)$ using Kelvin equation [35] assuming a water layer at $20C^o$ where P/P_s is the relative humidity ratio). γ_L is the liquid surface energy (for water $\gamma_L = 72mJ/m^2$), and γ_{SLS} is the surface energy between solid-liquid-solid interface. Often $\gamma_L > \gamma_{SLS}$, and the F_{SLS} force can be ignored. Finally, assuming $\theta \approx 0$ and $r_1 \ll \rho \ll R_t$, the F_{cap} reduces to:

$$F_{cap}(h) = 4\pi\gamma_L R_t(1 - \frac{h-2e}{2r_1})u(-h+L)\ . \tag{6.5}$$

6.3.3 Electrostatic Forces

Grounding a (semi)conducting substrate such as Si, Au or HOPG, the electrostatic forces are reduced. However, in the case of polystyrene latex particles, there are charges

trapped around the perimeter of the particles, and during pushing or contact, triboelectrification introduces local charges. Since the particles are not picked up, the electrostatic force between the particle and substrate is not important. But, after pushing, the charge on the particle is transfered to the tip which can cause an electrostatic force between the particle and tip (then particles can stick to the tip during retraction which is observed in some cases experimentally). As solution to this problem, the latex particles are coated with Au, and by grounding all the substrate and particles, electrostatic forces can be negligible. However, still a model for the electrostatic forces is desirable for general cases.

It is assumed that the all objects are free of charge at the beginning. But, after contacting with the objects, contact electrification and triboelectrification occurs, and forces due to these charges should be computed.

For the work functions of ϕ_1 and ϕ_2 of two surfaces, resulting voltage difference is $U = (\phi_1 - \phi_2)/e$ where $e = 1.6 \times 10^{-19}\ C$ is the e^- charge. Then the electrostatic force becomes as:

$$F_{el}(h) = -\frac{\epsilon_0 U^2 S}{2h^2} \ , \tag{6.6}$$

where ϵ_0 is the permittivity, and S is the shared area. For the tip-particle interaction, $S = 4\pi\tilde{R}r_1$, and $U = 0.25\ V$ for gold-coated particle surface and silicon tip. For the gold-coated particle and silicon substrate, $S = 4\pi R_a r_1$, and $U = 0.5\ V$. Then for $R_t = 30\ nm$, $R_a = 250\ nm$, $r_1 = 1.7\ nm$, and $h < 10\ nm$, F_{el}^{ta} is in the order of 10s of pN which can be almost neglected. For a given threshold separation distance between the tip and particle h^*, the electrostatic forces are discontinuous such that:

$$F_{el}(h) = F_{el}(h)u(h - h^*) \ , \tag{6.7}$$

where $u(x)$ function is the step function where $u = 1$ if $x \geq 0$; else $u = 0$.

6.3.4 Simulations

The above non-contact force models are simulated, and their relative magnitudes in the air environment are compared. For approaching of a silicon spherical tip to a flat gold surface as can be seen in Figure 6.4, the parameters of the simulation is as follows: $R_t = 30\ nm$, $H = 2.03 \times 10^{-19}$, $a_0 = 1.98\ A^o$, $\gamma_L = 0.072 J/m^2$, $r_1 = 1.06\ nm$, $L_l = 10\ nm$, $U = 0.25\ V$, $\epsilon_0 = 8.85 \times 10^{-12} C^2/Nm^2$, and $h^* = a_0$. The resulting forces are shown in Figure 6.5. From the figure it can be seen that $F_{cap} > F_{vdw} > F_{el}$ for the given case. Thus, F_{el} even can be neglected.

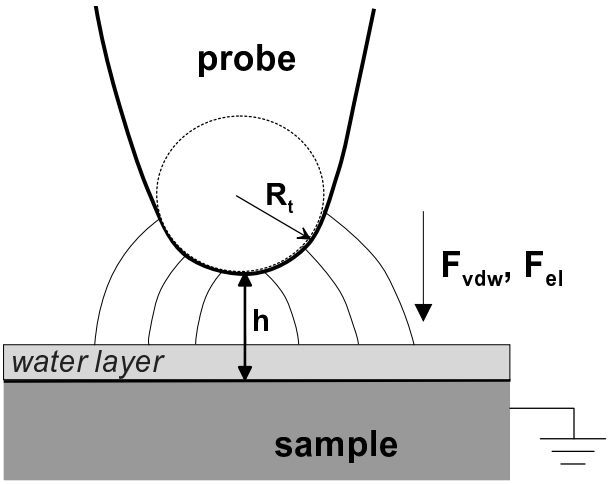

Figure 6.4: A spherical tip probe and a flat surface approach and retraction graph for surface force modeling simulations.

6.4 Modeling of the Micro/Nano Contact Mechanics

The contact mechanics of the micro/nano scale touch using the AFM tip as the single asperity contact tool is modeled as a mass-spring system as shown in Figure 6.6. P represents the applied load, k_c, b_c, m_c^*, ζ are the cantilever stiffness, damping constant, effective mass, and deflection respectively. $k_i(z,\zeta)$ and b_i are the *tip-surface interaction stiffness* and damping, and δ is the penetration depth. The dynamics of the cantilever can be given as [10]:

$$m_c^*\ddot{\zeta}(t) + 2m_c^* b_c \dot{\zeta}(t) + k_c\zeta(t) = k_i(z,\zeta)(z(t) - \zeta(t)) + 2m_c^* b_i(\dot{z}(t) - \dot{\zeta}(t) \ . \tag{6.8}$$

Assuming the damping terms are negligible, and removing the time $t \in R$ for the notation simplicity:

$$m_c^*\ddot{\zeta} + k_c\zeta = k_i(z,\zeta)(z - \zeta) \ . \tag{6.9}$$

Here, the special cases are: (1) if $k_i >> k_c$, $\zeta = z$ at the equilibrium which means there is no surface deformation, (2) when $k_i = -k_c$, then $m_c^*\ddot{\zeta} = k_i z$. During the contact, applying a load P by moving the cantilever base position to z results in the following equalities:

$$P(t) \ = \ k_c\zeta(t)$$

$$\begin{aligned} \delta(t) &= \Delta(t) - \zeta(t)cos\alpha \\ \Delta(t) &= z(t) - z_0 \ , \end{aligned} \tag{6.10}$$

where z_0 is the piezo position when the tip contacts to the sample.

6.4.1 Hertz Model

For the Hertz deformation model, load P results in a contact radius a with the general relation of:

$$\begin{aligned} P &= Ka\delta \\ \frac{1}{K} &= \frac{m}{2}(\frac{1-\nu_t^2}{E_t} + \frac{1-\nu_s^2}{E_s}) \ , \end{aligned} \tag{6.11}$$

where K is the *reduced elastic modulus* for the tip-sample system, m is the tip geometry dependent constant ($m = 1$ for the cylindirical, $m = 1.5$ for the spherical, and $m = 2$ for the conical tip case), E_t and E_s are the Young modulus, and ν_t and ν_s are the sample Poison's coefficients respectively. For our system, the AFM tip is spherical with radius $R_c \approx 20 - 30\ nm$, and using the Hertz model for a sphere-flat object interaction, $a = \sqrt{R_c\delta}$. Then following relation can be computed:

$$\Delta = \delta + \sqrt{R_c}Kcos\alpha\delta^{3/2}/k_c \ . \tag{6.12}$$

If the tip is very sharp, i.e. $R_c < 10\ nm$, the geometry can be assumed to be conical with the tip half angle ψ where $a = \pi tan\psi\delta/2$. Then,

$$\Delta = \delta + \frac{\pi tan\psi}{2Kk_c}\delta^2 \ . \tag{6.13}$$

Furthermore, some researchers [77] approximates the contact radius using simple geometry as $a = \sqrt{2\Delta R_c}$ for the spherical tip case, then:

$$\delta = \frac{k_c\Delta}{k_c + Kcos\alpha\sqrt{2\Delta R_c}} \ . \tag{6.14}$$

6.4.2 DMT Model

This model accounts for long-ranged attraction around the periphery of the contact area while the defromation geometry is Hertzian such that for a sperical tip and flat surface:

$$\begin{aligned} P &= Ka^3/R_c - 2\pi R_c\omega \\ \delta &= a^2/R_c \ , \end{aligned} \tag{6.15}$$

where ω is the adhesion energy.

6.4.3 JKR Model

Adding the short-ranged adhesion forces, for spherical tip and flat surface, JKR model results in following equations:

$$\begin{aligned} P &= Ka^3/R_c - \sqrt{3\pi\omega K a^3} \\ \delta &= a^2/R_c - 2/3\sqrt{3\pi\omega a/K} \\ a^3 &= R_c/K(P + 3\pi R_c\omega + \sqrt{6\pi R_c\omega P + (3\pi R_c\omega)^2}) \ . \end{aligned} \tag{6.16}$$

6.4.4 MD Model

MD model assumes a constant stress $\sigma_0 = 1.03/a_0$ over the annulus d in Figure 6.7. By analogy with the plastic zone ahead of a crack, MD model can be used for all cases [47], [69], [36] such that:

$$\begin{aligned} \tfrac{\lambda a^2}{2}\left(\tfrac{K}{\pi R_c^2\omega}\right)^{2/3}[\sqrt{m^2-1} + (m^2-2)cos^{-1}\tfrac{1}{m}] + \tfrac{4\lambda^2 a}{3}\tfrac{K}{\pi R_c^2\omega}^{1/3}[\sqrt{m^2-1}cos^{-1}\tfrac{1}{m} - m + 1] = 1 \ , \\ \delta = \tfrac{a^2}{R_c} - \tfrac{4\lambda a}{3}\left(\tfrac{\pi\omega}{R_c K}\right)^{1/3}\sqrt{m^2-1} \ , \\ P = \tfrac{Ka^3}{R_c} - \lambda a^2\left(\tfrac{\pi\omega K^2}{R_c}\right)^{1/3}[\sqrt{m^2-1} + m^2 cos^{-1}\tfrac{1}{m}] \ , \\ \lambda = \tfrac{2.06}{a_0}\left(\tfrac{R_c\omega^2}{\pi K^2}\right)^{1/3} \ , \end{aligned} \tag{6.17}$$

where a_0 is the interatomic distance, and m is the ratio of the width of the annular region to a. If $\lambda \to 0$, The MD model converges to the DMT model, and if $\lambda \to \infty$ it converges to the JKR model.

6.4.5 Experiment and Simulations

For comparing above deformation models, a silicon tip and silicon sample are contacted ($E_{si} = 110\ GPa$, $\nu_{Si} = 0.35$). Assuming a water layer between the tip and sample, $\omega \approx 2\gamma$ where $\gamma = 72mJ/m^2$, indentation force and a vs. Δ curves are held as shown in Figure 6.8 during unloading (retraction). In the figure, also the real data which is held from the experimental automatic approach and retraction data as the contact unloading slope of $\approx 8.5\ N/m$ is shown. However, the contact radius cannot be directly measured, and the real one is not shown. The results show that JKR overestimates the contact area while DMT and Hertz underestimates, and DMT and Hertz models also underestimates the applied load. For different samples with different E_s, MD gives the load, cantact radius and m data as can be seen in Figure 6.9. As the surface becomes soft, i.e. E_s is smaller, the contact area is increased while the applied

Model	*Assumption*	*Applicable Cases*
Hertz	no surface forces	high loads with small surface forces
DMT	long-ranged surface forces act only outside of the contact area	rigid surfaces with low adhesion
JKR	short-ranged surface forces act only inside of the contact area	small load and high surface forces
MD	periphery of tip-sample interface is modeled as a crack	all cases

Table 6.1: The properties of the contact models.

load is decreased. This may cause problems in the force feedback scaling since the same scaling factor may not give the enough scaled feedback on the operator finger for different range of surfaces. One solution is the preliminary calibration of the force scaling factor for all surfaces for optimal force feedback.

The general properties of each model is given in Table 6.1. From the table, Hertz model is realistic in the case of large external loads with compared to surface forces. However, load amounts may not be large during micro/nano manipulation tasks, thus this model should not be utilized in the case of small loads. DMT model can apply well to the rigid surfaces with low adhesion, but may underestimate the true contact area. On the other hand, JKR model adds the effect of adhesion to the Hertz model, and it can be used in the case of small loads. But, it assumes that short-ranged surface forces act only *inside* the contact area, and this may underestimate loading due to the surface forces. Finally, MD model is the recent best model since it is analytical, and does not underestimate surface forces and contact area.

As the next experiment, silicon AFM tip is touched to different materials, and the experimental unloading curves are held as shown in Figure 6.10. Depending on the E_s, the slope is different, i.e. larger E_s has a larger slope, and the pull-off (separation) point gives information about the adhesion between the tip and surfaces. The maximum adhesion exists when the sample is steel, and it is minimum for silicon sample. The infinite stiff surface line is shown also in the figure where mica gives the closest curve to this line. Steel and silicon are softer than the mica, and less slope.

Finally, the approach and retraction of a silicon probe and silicon substrate is simulated using the proposed surface force and contact models, and compared with the real experimental data. MD models are utilized as the contact model, and electrostatic forces are neglected. For a silicon material $E_t = E_s = 110\ GPa$, and the resulting parameter value for the MD model is $\lambda = 0.367$, and the equations are solved using the Newton-Raphson numerical techniques. The other force model parameters are:

$R_t = 30\ nm$, $H = H_{Si,H_2O,Si} = 1.33 \times 10^{-19}\ J$, and $\nu_{Si} = 0.27$. Thus, the simulated and experimental force-distance curves are shown in the Figures 6.11 and 6.12 respectively. In Figure 6.11a, a capillary force-dominant interaction is simulated with the paarmeters of $\gamma_L = 72mJm^2$ and $e \approx 8\ nm$. From Figure 6.11a and 6.11b, the behaviour is very similar while the magnitudes of the pull-off (separation) and contact positions are different with around ten times scale. The reasons of this scale can be due to the resolution of the stage, i.e. the large steps of motion results in more smooth and enlarged curve data, and the water layer can be larger than the expected value. As the second data, simulation model parameters in Figure 6.12a are tuned for a contact mechanics-dominant interaction in order to coincide with the real data in Figure 6.12b. By tuning the parameters, $\gamma_L = 0.45\ J/m^2$ and $e \approx 20\ nm$ values are held. Thus, the theoretical model parameters are computed for a *realistic* model by comparing with the real data.

6.5 Virtual Reality Simulator for Tele-Nano-Touch

For simulating the micro/nano touch feedback, a Virtual Reality (VR) Simulator is constructed for freely changing the parameters, and initial training. A sample interface graphics can be seen in Figure 6.13. Moreover, a realistic simulator will enable a real-time animator display for real-time nano manipulation monitoring such that the models can predict the position of the manipulated objects in real-time. and can animate this modeled behaviour in the simulator. Using the haptic device, and the micro/nano contact mechanics models, hybrid simulation type of touching experiments are realized.

6.6 System Setup

Tele-Micro/Nanorobotics system is utilized during the experiments. The hardware structure of this experiment can be seen in Figure 6.15. The Nano Visulator graphics display of the scanned real-surface data, and real-time AFM tip position, and force feedback through force reflecting servo-type controller enabled the real-time touching feedback experiments.

6.7 Experiments

6.7.1 Single-Asperity Contact Feedback

Single-asperity contact to silicon surface experiment is realized initially. The AFM tip parameters are $R_c = 20\ nm$, $k_c = 8\ N/m$ and $S = 0.033\ \mu m/Volt$. Touching to the silicon sample at the 40% humidity conditions, resulting master and scaled slave

$k_c = 40N/m$	$f_r = 150KHz$	$R_c = 10nm$
$Q_c = 100$	$\gamma_L = 0.073J/m^2$	$H = 1.89 \times 10^{-19}J$
$\omega = 0.072J/m^2$	$E_t = 170GPa$	$E_s = 4GPa$
$\nu_s = 0.3$	$\nu_t = 0.5$	$\sigma = 3.49A^o$
$L_l = 0.8nm$	$r_1 = 1.2nm$	$\delta = 4nm$

Table 6.2: Parameters of the touch simulation model.

position and forces can be seen in Figure 6.17. Experimental parameters are $K_f = 2$, initial tip height $H = 0.6\ \mu m$, $\alpha_p = 4 \times 10^{-3}$ and $\alpha_f = 2.0 \times 10^6$. As can be seen from the figure, ideal responses of tracking the master and scaled slave forces and positions are realized successfully. The negative attractive forces are significantly large enough to feel the sticking to the surface. However, this sticking effect is small during the approach, and very large when retracting back. The reason is the adhesion force which result in an increased attractive force during separation. This difference causes of the force tracking error during the approach phases since the force occurs only very close to the surface $(20 - 50\ nm)$. However, there is no tracking error for the positions since the piezoelectric stage has a closed-loop accurate control for the reference positions.

experiments:

- comparing different scaling laws
- VR SImulator results

Experimental results of bilateral interaction using the Virtual Impedance controller during touching to a mica surface is shown in Figure 6.18. $M_v = 0.1kg$, $B_v = 20N/(m/sec)$, $K_v = 0$, $\alpha_p = 15 \times 10^{-9}$, $\alpha_f = 1 \times 10^8$, and $K_f = 20$ are taken. Initial tip-sample position is $10nm$. AFM force feedback is simulated in the Nano Simulator using the derived models with the parameters in Table 6.2. As can be seen in the force-time graph, the operator starts to apply force at around 0.8 sec. Then the master device also begins to move in according to $V(s)$ until to the contact point. After the contact, the point after the (-) nano force, ideal response is being held where $F_m(t)$ and $\alpha_f F_s(t)$ are balanced, and $x_m(t)$ stops. But, if the operator continues to push more, again the controller tracks both forces and positions. When $F_m(t) = 0$ at around 4.6 sec, i.e. operator removes his finger from the device, master device moves back to the contact point again.

6.7.2 Surface Tactile Feedback

In this mode, the measured sample topology is felt on the operator's hand while scanning a sample such as in [30]. At first, the cantilever tip is approached to the surface, and put in contact with the substrate. Then, by controlling the x-y AFM

cantilever motion by a mouse, the operator, putting his/her finger on the haptic device, can feel the scaled measured relative height of the surface by the bilateral touch feedback using the force reflecting-servo type controller. As the experimental result, an image given in Figure 6.19a is scanned along the line shown in the figure. The resulting tactile-sensing with the scale parameters of $\alpha_p = 10^{-6}$ and $\alpha_f = 1 \times 10^6$, and the force error gain of $K_f = 10$ is given in Figure 6.19b. The upward jumps stand for the silicon grid structures. Furthermore, a Focused Ion Beam Fabricated character '3' as shown in Figure 6.7.2 is felt on the operator's hand by moving on a user-defined trajectory as shown in 2-D display of the AFM image in the figure. The resulting touch-feedback of the surface is given in Figure 6.21 where the topology can be felt successfully. Finally, an InAs quantum dot structures of around 10 nm size are felt on the operators's hand during scanning on the sample as given in Figure 6.22. The jumps are the quantum dot structures. In this mode, the nano objects are assumed to be fixed on the substrate since the touching operation is held in contact mode type of AFM imageing which can move not well-fixed samples on the surfaces.

6.8 Discussions

From the experimental results, it can be observed that the proposed bilateral scaled teleoperation control system is successful for providing touching force feedback at the micro/nano scale. The important parameters for the reliable sensation are:

- Scanning speed: taking the bandwith effect problem into consideration, the scanning speed should be small for feeling the small features easily,
- Force reflecting servo type of controller gives less damping force feedback since there is no artificial dynamics added to the system while the Virtual Impedance controller is more stable for abrupt force changes, and filters the force noise as a second-order low-pass filter,
- MD model gives the best contact mechanics modeling in the VR Nano Simulator experiments since it can be applied to all cases without any assumption,
- The stage positioning accuracy is around 15 nm during the experiments which added limitations to the resolution of the felt micro/nano forces, and also caused instability problems in the case of stiff surfaces where vibrational behaviour occured in some cases if the force error gain K_f is selected as a large value. Therefore, the accuracy of the stage should be increased to few nanometers for more stable and high resolution force feedback,

- During the tele-nano contact, depending on the sample and tip adhesion forces, the selection of the force scaling factor α_f differs such that: for high surface adhesion, i.e. large tip radius (R_t) and high adhesion energy (γ_L), $\alpha_f = 1/\alpha_p$ gives better feedback while for small adhesion forces, $\alpha_f = 1/\alpha_p^2$ is a better selection which coincide with the theoretical calculations of Goldfarb [24]. Moreover, depending on the softness of the samples, these rules do not give good results such that the interaction/contact forces become exponetially very small while the motion range also increases. Thus instead of previous rules, our proposed heuristic rule becomes more attractive where the minimum and maximum contact force values are measured before the experiments, and α_f should be selected according to the Eq. (5.3),

- Electrostatic forces seem to be negligible for previously non-charged surfaces and grounded substrates. However, for a non-conducting sample, even the tip is conductive or semi-conductive, charges can be stored after the contact interaction, and these charges can increase the tip charge such that after a long time contact interaction with a sample, the electrostatic forces can increase as well as the tip can be deformed and the tip radius can increase. Thus, the adhesion forces could *increase with time* which should be included in the Nano Simulator modeling [11],

- During the approch process, the attractive forces becomes large only in the close vicinity to the surface. Therefore, the approach speed should be slow and the positioning resolution of the stage should be high for a *repeatable* approach attractive force feedback. Thus, in the experiments, these parts are felt only sometimes. As a solution to this kind of cases: α_f *should be selected depending on the region* such as approaching, indenting and retracting regions. However, in this case, the continuity of the forces is difficult during passing from one region to another, and therefore, depending on the purpose of the operator, region-dependent scaling may be or may not be used,

- Water layer on the surfaces and tip causes the instable jump-in-contact problem during approaching to surfaces, and increases the adhesion meniscus bridge length during the retraction. Thus, environmental conditions during the tele-touch experiments are important for understanding which forces we are feeling during the experiments,

- Cantilever parameters such as the stiffness k_c, tip size and shape R_t, resonance frequency f_r, and quality factor Q_c should be calibrated for the real AFM cantilever to be used in the experiments before the simulations for getting realistic interaction simulations.

Proposed force modeling is put into the VR Nano Simulator which enables a simulated training and test environment. At the simulations, also the effect of all different contact mechanics models can be tested easily. Frictional models are also added for 2-D Simulator, and by changing the simultor graphics to 3-D, also the 3-D simulations will be possible which is a future work.

6.9 Conclusion

In this chapter, a teleoperated micro/nano scale touching system is proposed, and micro/nano contact mechanics models are introduced. Using a 1-DOF haptic device, and Virtual Impedance and force-reflecting servo type scaled teleoperation controllers, touching experiments and VR Simulator-based simulations are realized. Scaling issue of the micro/nano force and position is discussed and possible solutions are proposed. Experimental and simulation results show that the proposed system can be used for micro/nano scale touching applications. During the experiments it is observed that only visual feedback is not enough for interacting the micro/nano worlds since the visual feedback includes many source of errors such as positioning drifts, nonlinearities, noises, and etc., and the force feedback can be reliably used for compensating these errors.

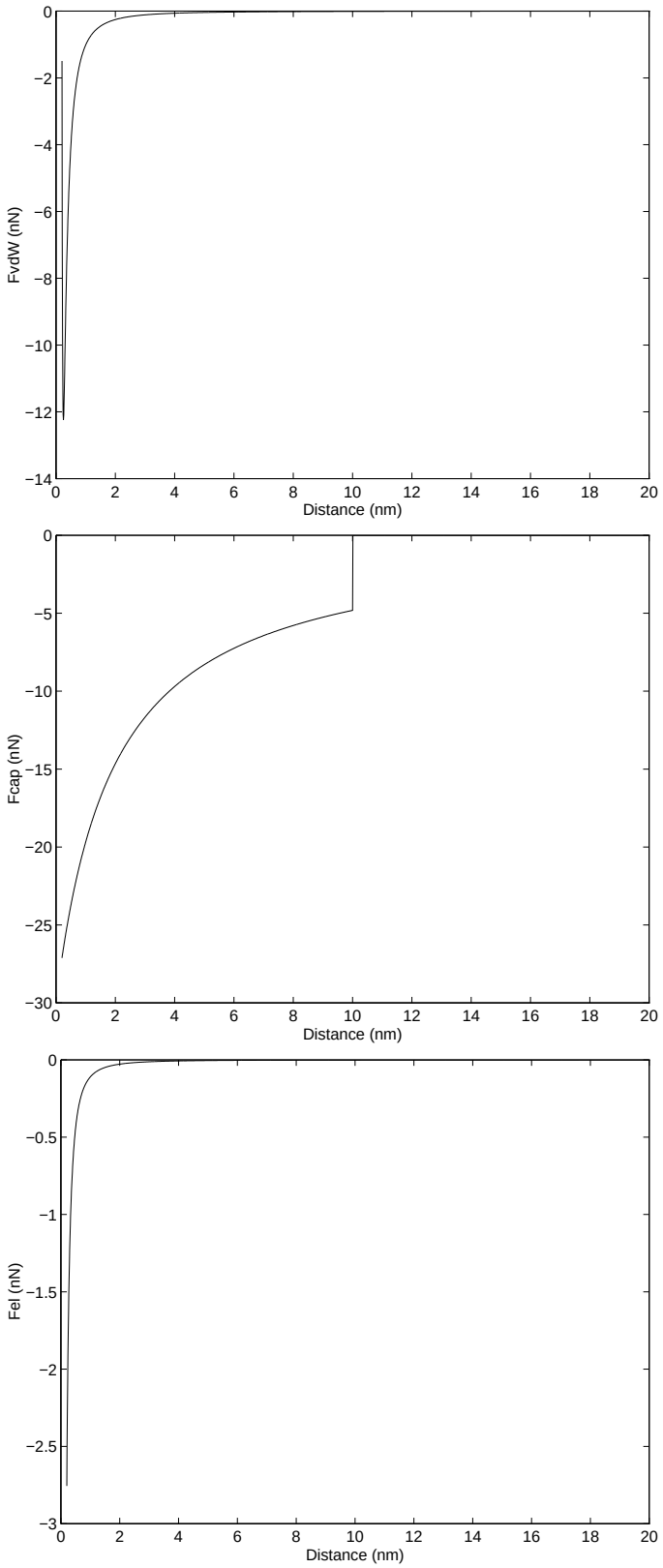

Figure 6.5: Comparison of the magnitudes of the F_{vdw} (uppermost), F_{cap} (middle) and F_{el} (bottom) non-contact attractive forces in air.

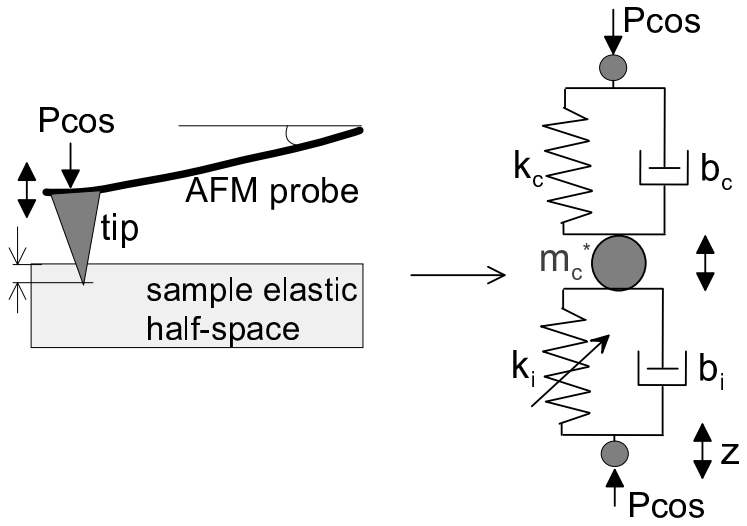

Figure 6.6: Mass-spring model of the contact mechanics for the deformable surfaces at the micro/nano scale using AFM tip as a single asperity contact tool.

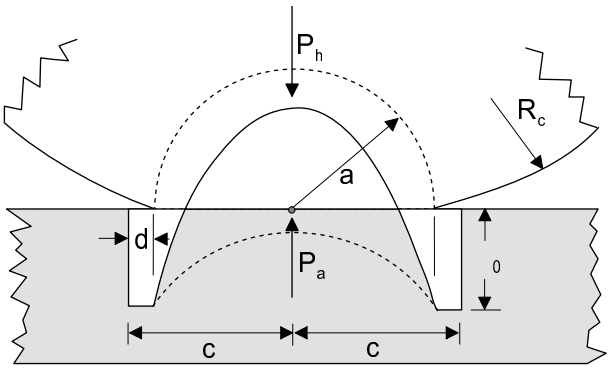

Figure 6.7: Continuum mechanics model of the elastic contact using Maugis-Dugdale approach.

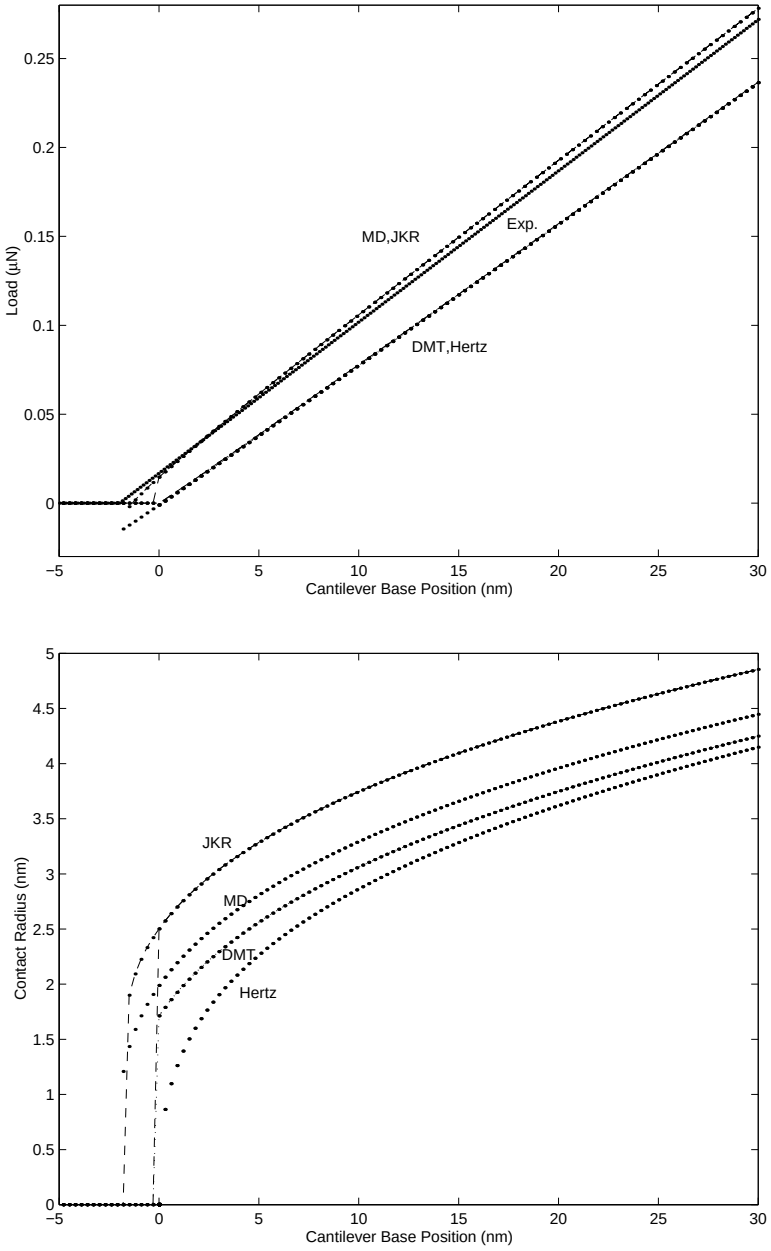

Figure 6.8: Applied load and contact radius results for Hertz, DMT, JKR and MD models during unloading (retraction) in the case of silicon tip and substrate contact (Exp. (solid line) in the load graph represents the experimental data).

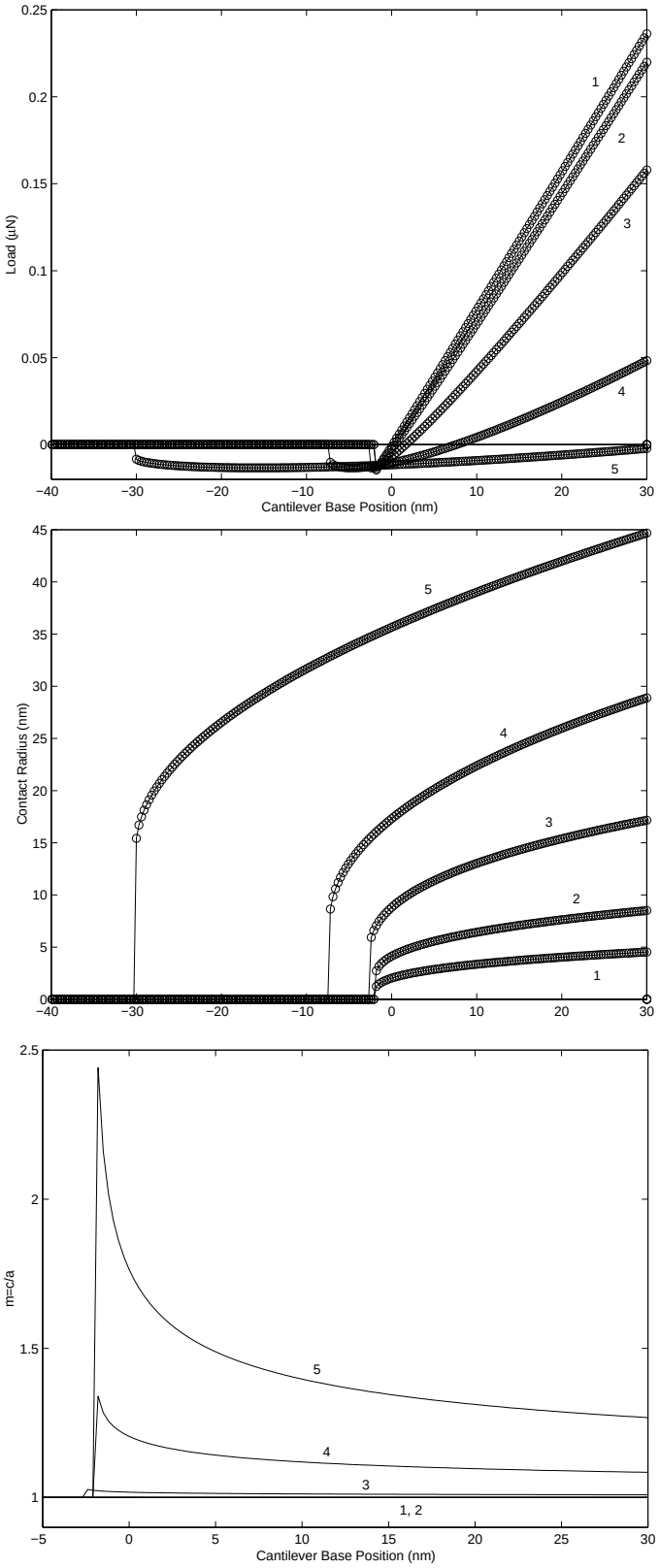

Figure 6.9: Load (upper), contact radius (middle), and m (bottom) vs. tip base displacement curves for different materials during unloading (E_s=(5) 0.01, (4) 0.1, (3) 1, (2) 10, (1) 100 GPa) using the MD model.[67]

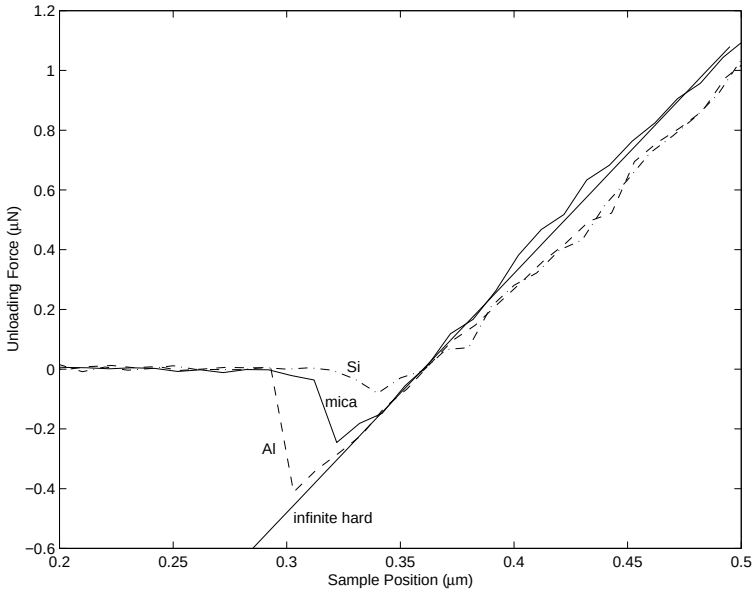

Figure 6.10: Experimental load (upper) vs. tip base displacement curve data for different materials during unloading for aluminium (E_s = 70 GPa; dashed line), mica (E_s =$\sim$ 200 GPa; solid line), silicon(100) (E_s = 110 GPa; dashed-dotted line), and infinitely hard material (linear line).

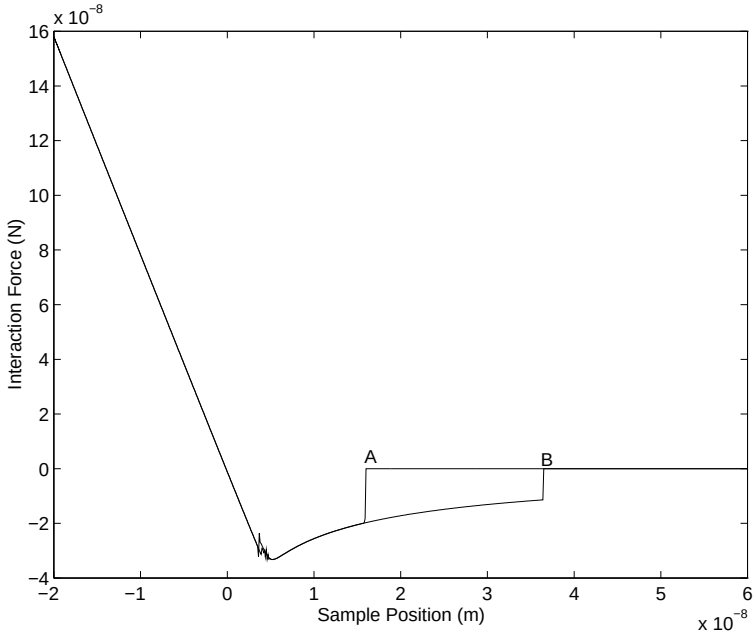

(a)

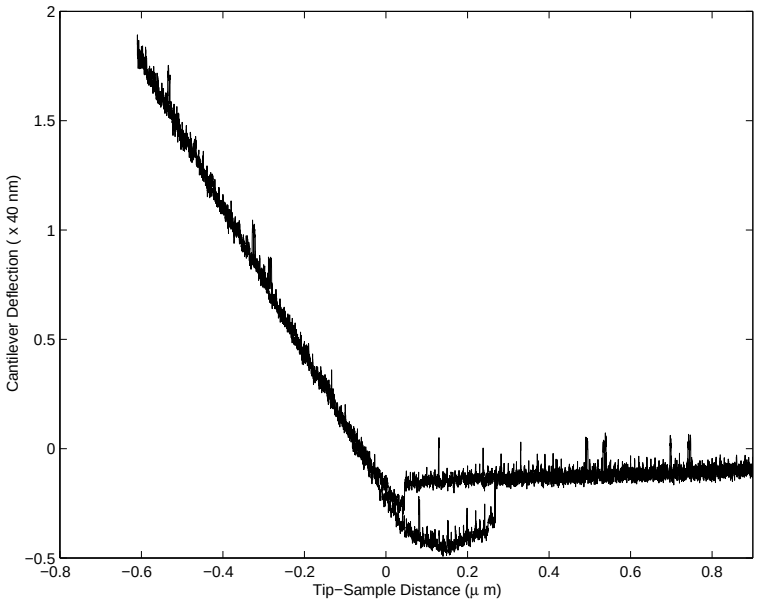

(b)

Figure 6.11: Capillary force-dominant silicon tip and surface approach and retraction data. (a) simulation using the surface forces and MD contact mechanics models; (b) experimental data. Point A in the upper image corresponds to the approach jump-to-contact point due to the capillary forces, and point B do for the separation point of the tip-water layer meniscus bridge.

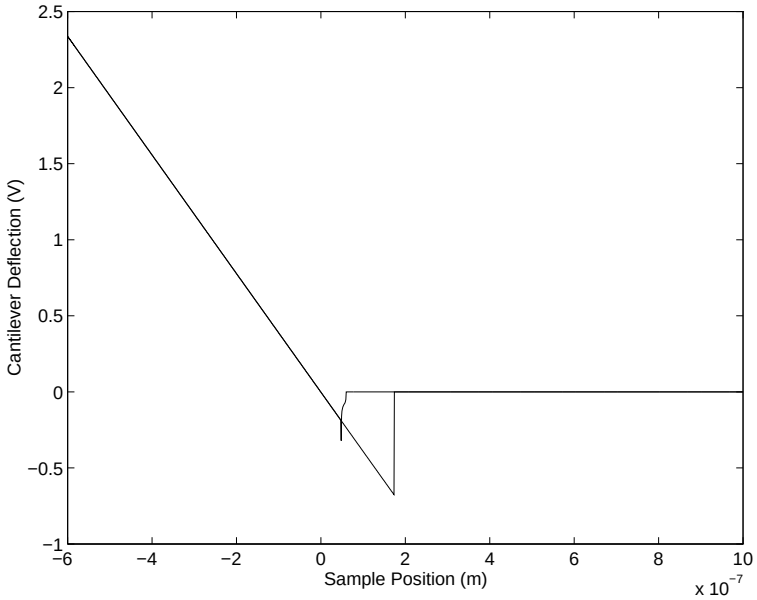

(a)

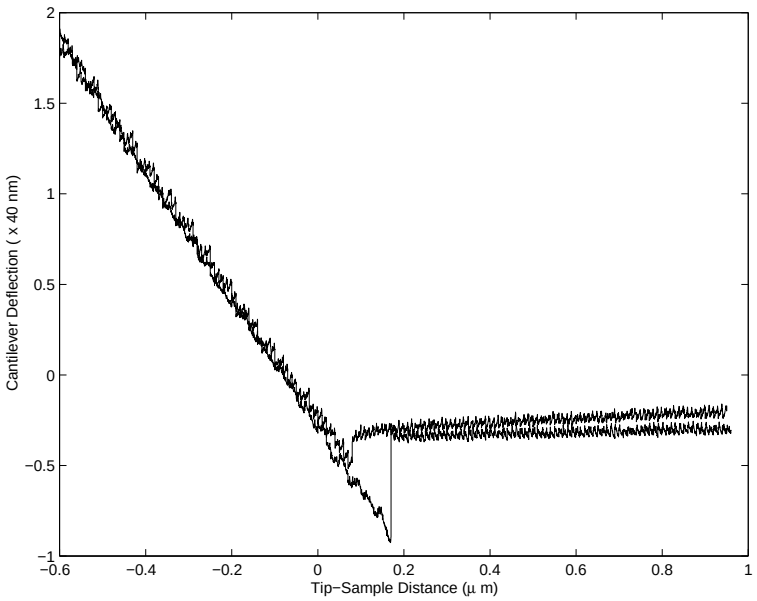

(b)

Figure 6.12: Contact mechanics-dominant silicon tip and surface approach and retraction data. (a) simulation using the surface forces and MD contact mechanics models; (b) experimental data.

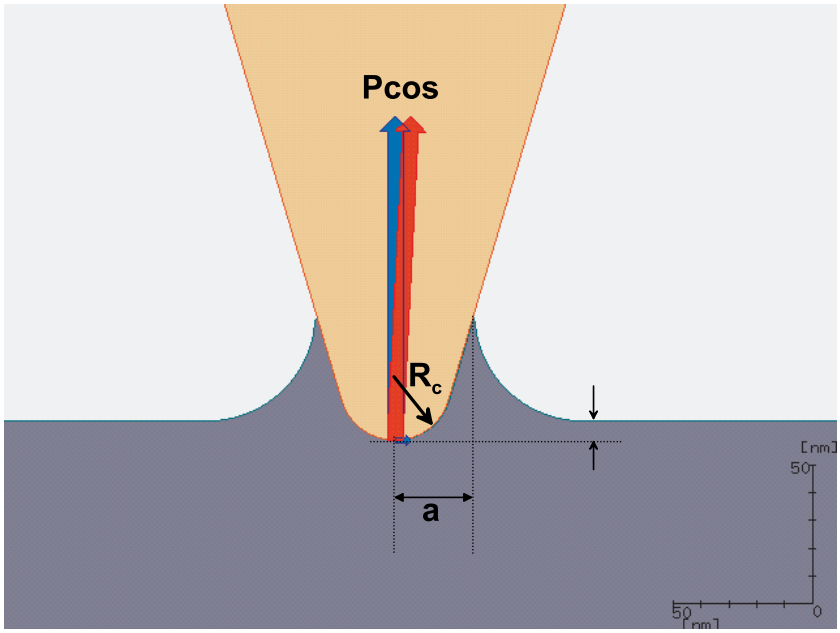

Figure 6.13: Virtual Reality Simulator for AFM tip-sample 1-DOF contact interaction.

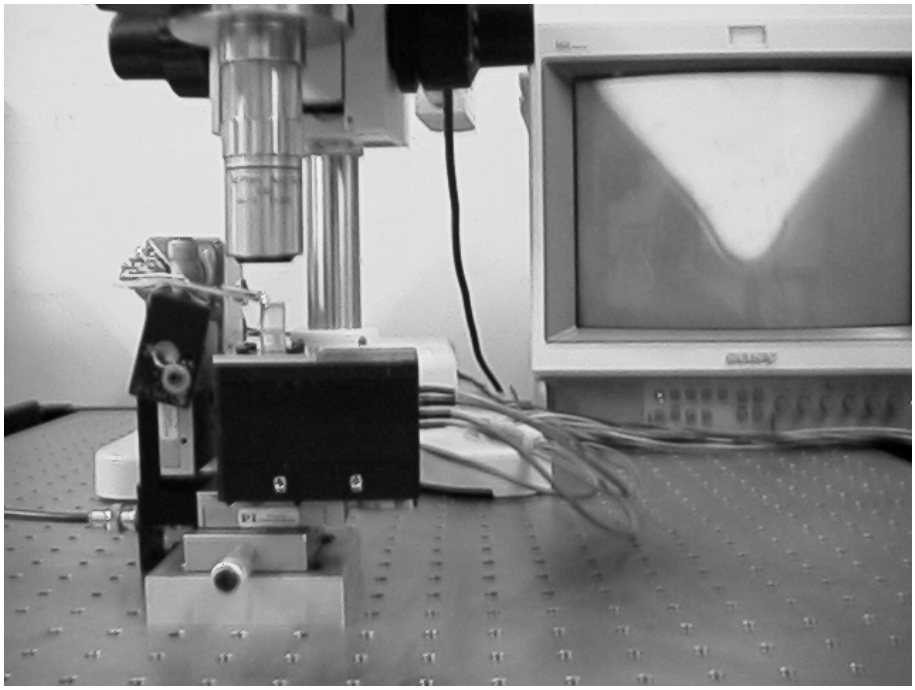

Figure 6.14: AFM system setup photo during tele-touch experiments.

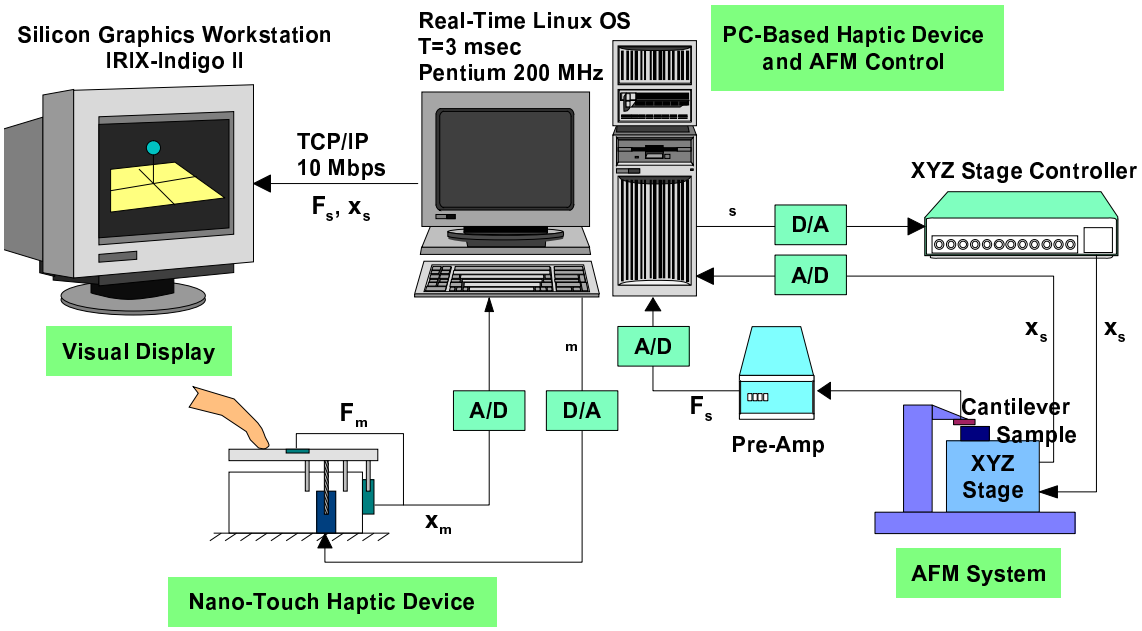

Figure 6.15: Hardware system structure.

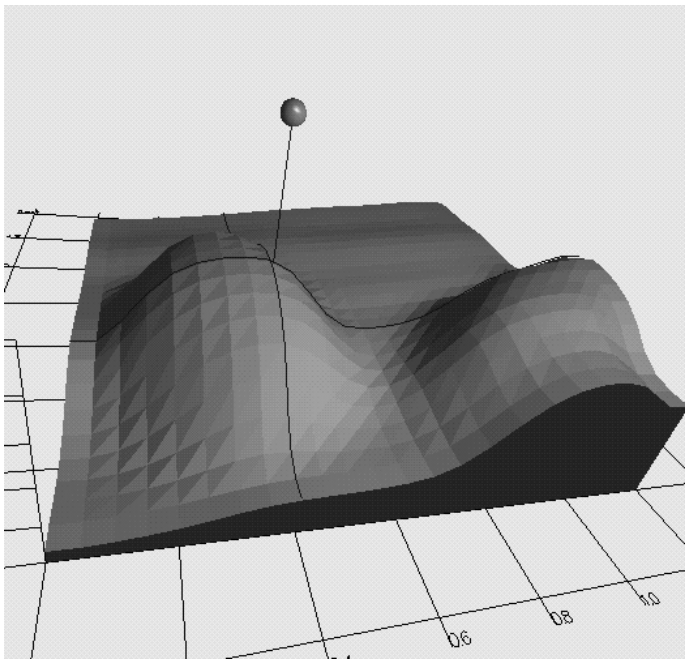

Figure 6.16: Virtual Reality Visulator during touching experiments (sphere represents the tip).

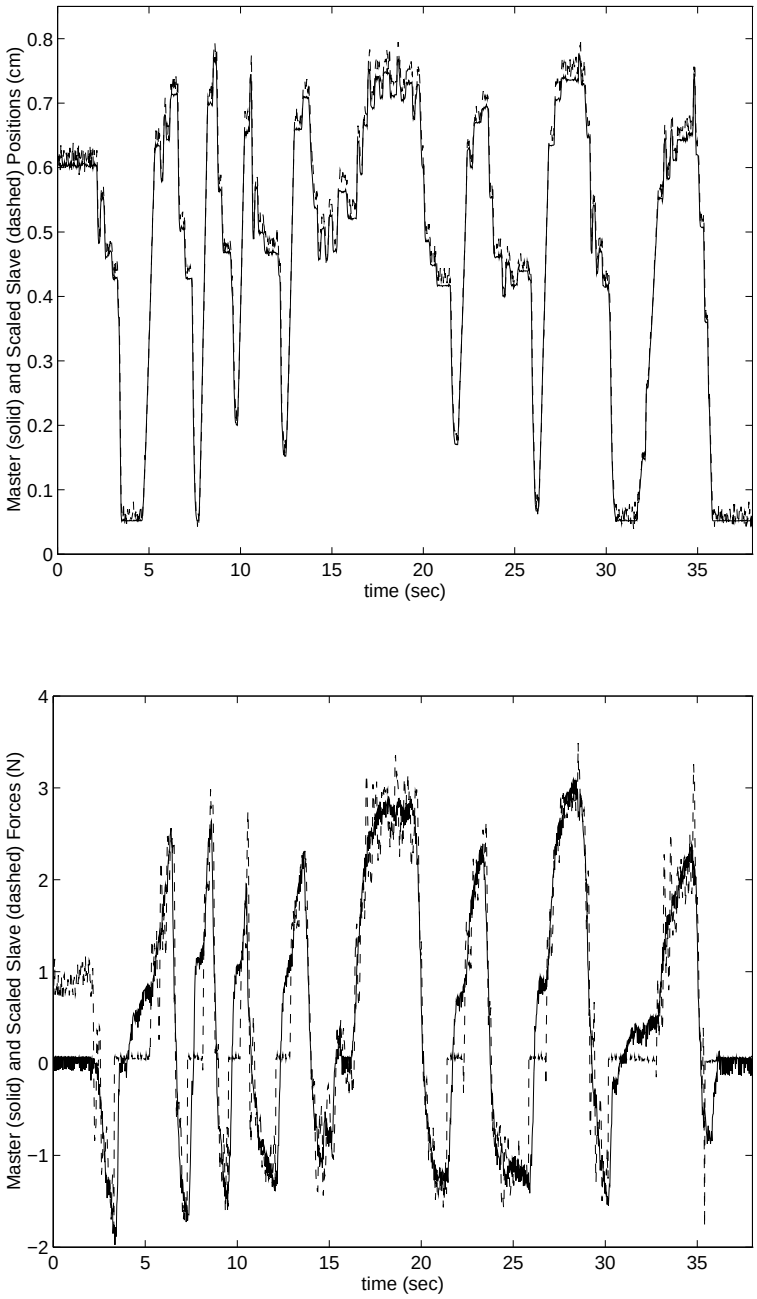

Figure 6.17: Touching results to a Si sample with Si tip: master (dashed) and scaled slave (solid) position (upper) and forces (lower).

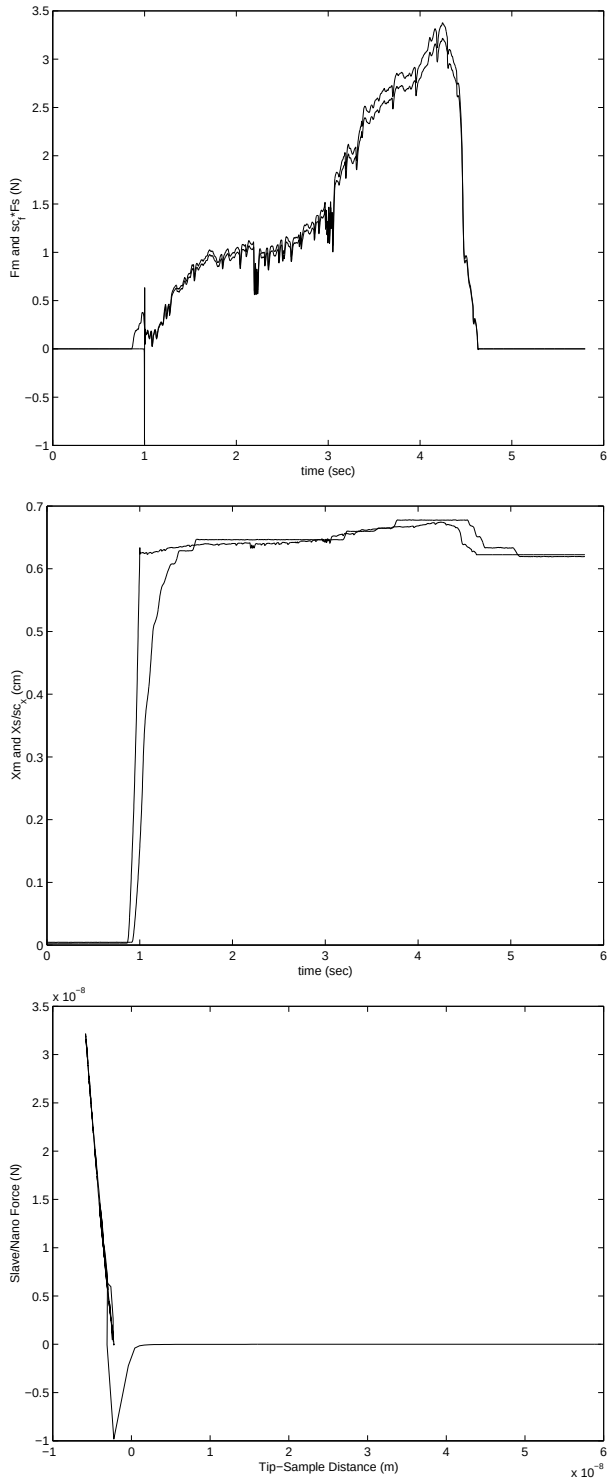

Figure 6.18: Bilateral force feedback during approaching to a mica sample using the Virtual Impedance controller where $F_m(t)$ and $\alpha_f F_s(t)$ (upper), $x_{mr}(t)$ and $x_m(t)$ (middle), and $F_s(h(t))$-$h(t)$ (bottom) graphs using the Hertz contact modeling.

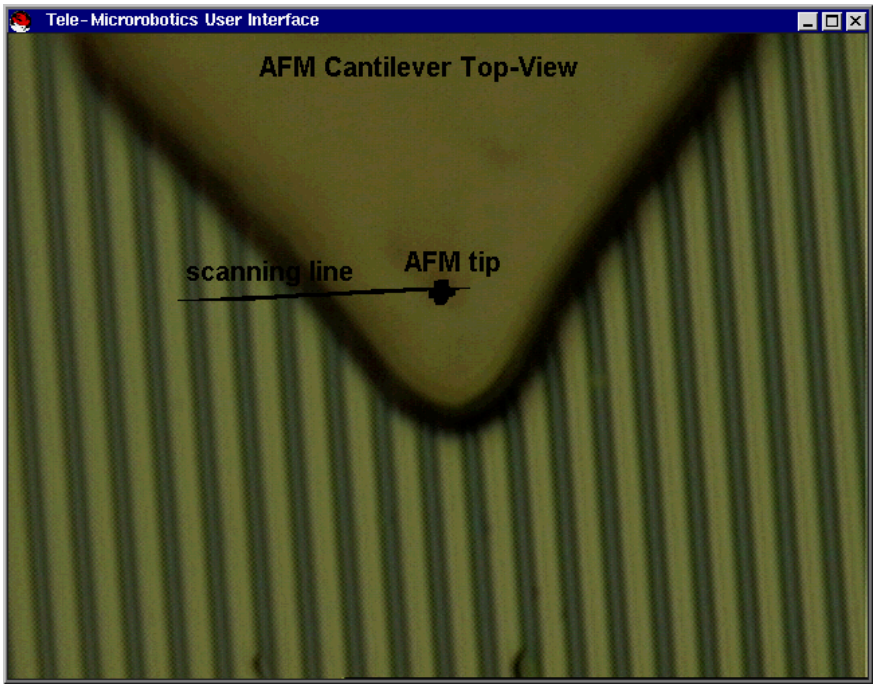

(a)

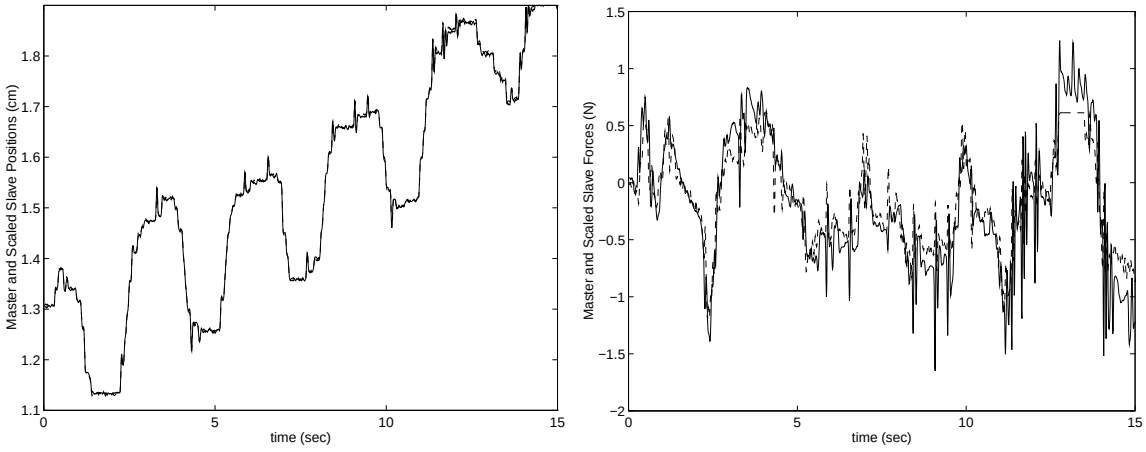

(b)

Figure 6.19: (a) Silicon grids with 480 nm height are scanned along the black line, and (b) the resulting topology feedback and force feedback using the force reflecting servo type teleoperation controller.

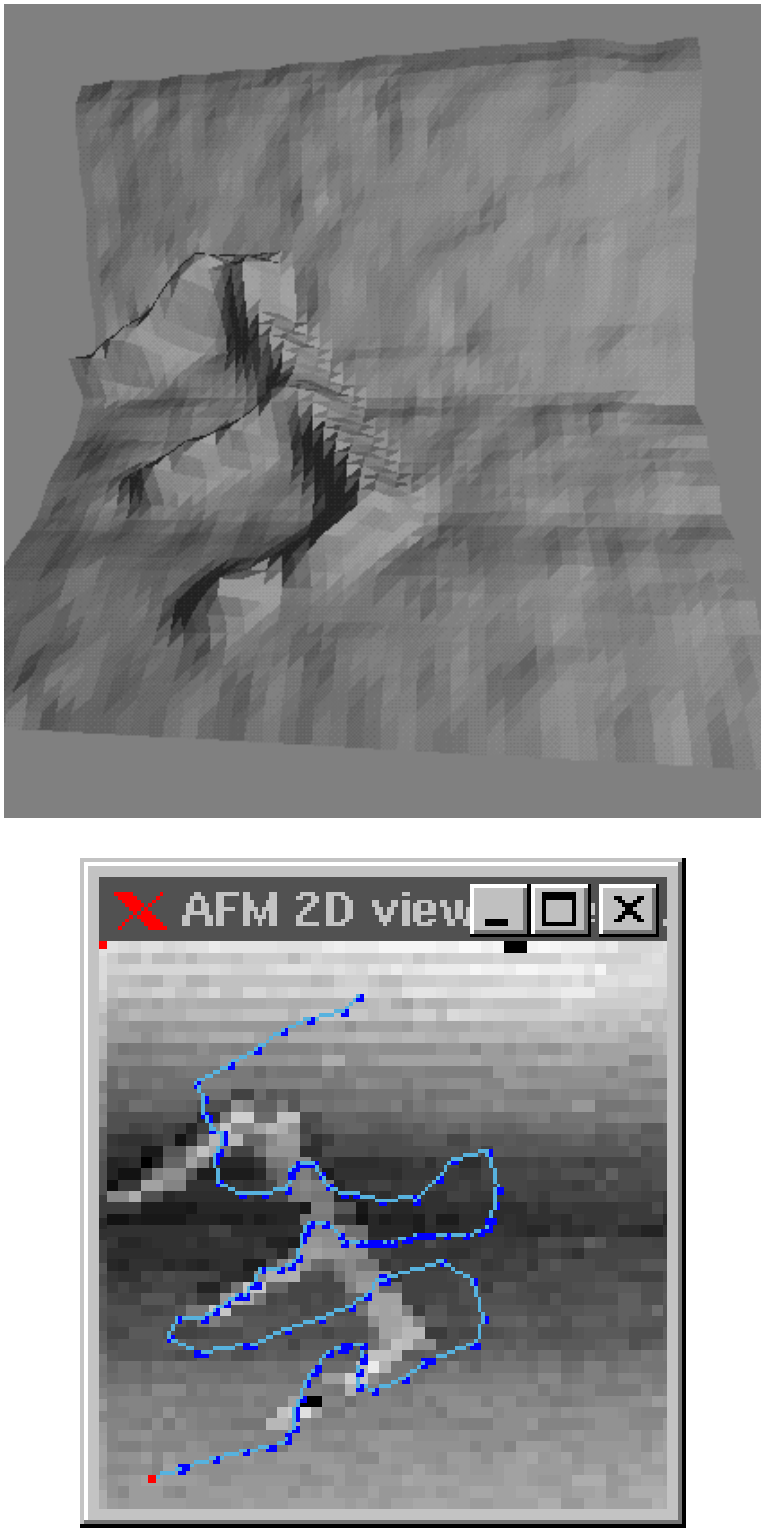

Figure 6.20: Tactile-feedback of the silicon sample surface with FIB etched number '3' in $10 \times 10 \mu m^2$ area. 3-D graphics (upper), and 2-D image with mouse traces (bottom).

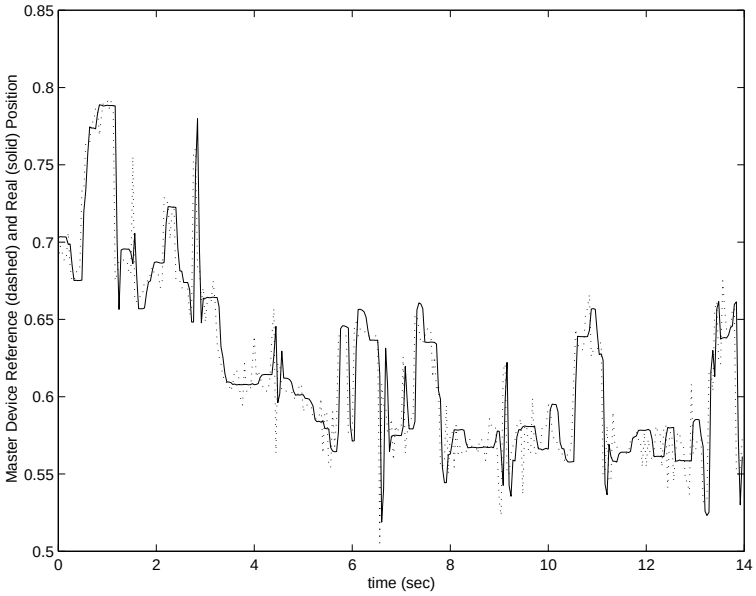

Figure 6.21: Resulting tactile feedback of the user-defined touching on the character '3'.

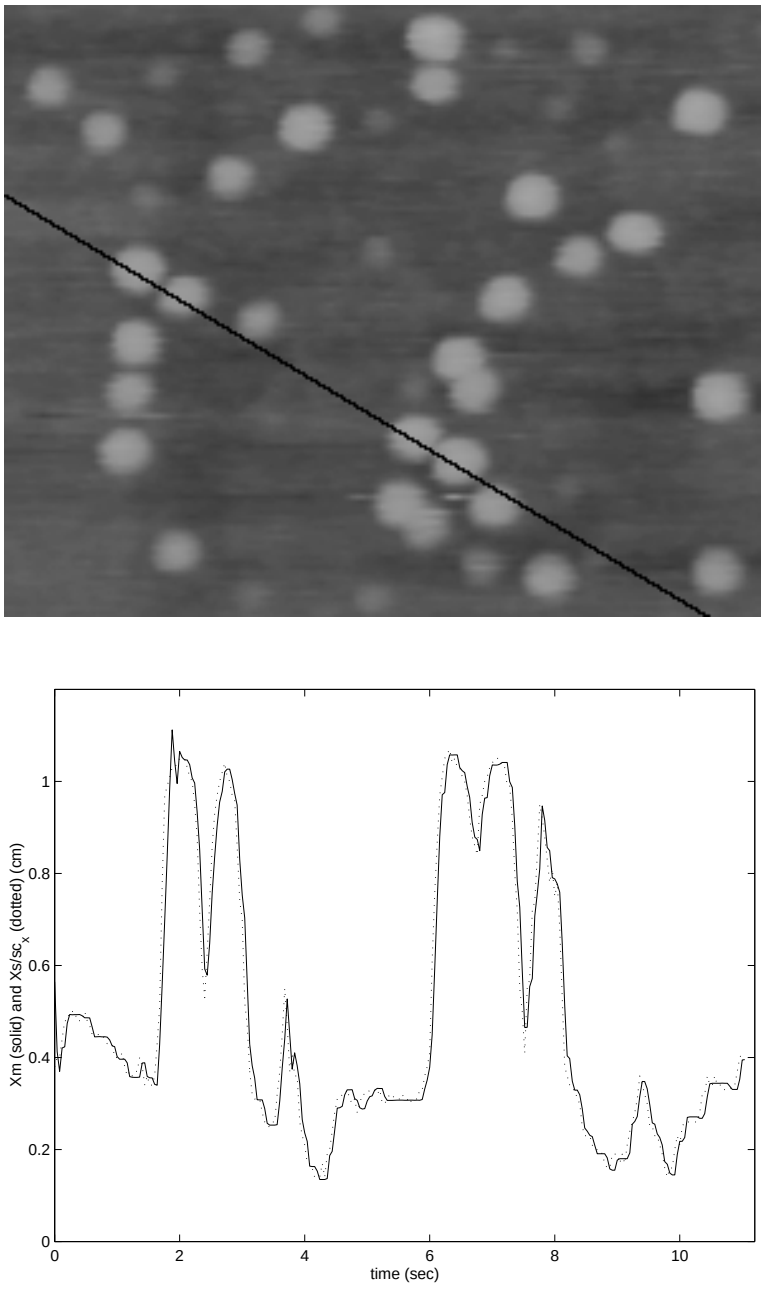

Figure 6.22: Touching to an InAs quantum dot surface (upper), and the resulting tactile feedback along the scanned line (lower).

Chapter 7

Application II: Controlled Pushing of Micro/Nanoparticles

7.1 Introduction

Nanotechnology which aims at the ideal miniaturization of devices and machines down to atomic and molecular sizes has been a recent hot topic as a promising high-technology for the forthcoming century. By precise control of atoms, molecules or nano scale objects, new sensors and man-made materials, tera-byte capacity memories, micro scale robots/machines, DNA-computers, quantum devices, micro scale distributed intelligence system devices with integrated sensors, actuators and communication tools, and etc. would be possible within the near future. However, for new nanotechnology products, still there are many challenges to be solved, and nano manipulation is one of the important challnges at the nano world. This kind of research is still immature since the physical and chemical phenomenon at this scale has not been completely understood, intelligent automatic precision manipulation strategies are not developed, and the specific tools for the specific applications have not been defined/designed clearly. Thus, the purpose of this chapter is to propose an Atomic Force Microscope (AFM)-based force controlled pushing system with physical analysis of the manipulation tool (AFM tip) and nano scale object physical interaction for 2-D positioning and assembly of nanoparticles.

AFM is a 3-D atomic resolution microscope which uses the interatomic force measurement principle for helding the topology images. Its mechanicsm is mechanical, and can be applied to imaging of all types of particles/samples which are fully or semi-fixed on a substrate with homogenous surface stiffness and interatomic force properties. Changing its function from only imaging to both imaging and manipulation, new challenging problems are introduced. At first, the particles on substrates should be *semi-fixed* in order to be able to move them. The solution to this problem could be using non-contact

mode AFM imaging for not moving the particles during imaging as proposed by [66]. However, the selection of the absorption chemicals is a difficult issue depending on the type of the substrate and particle (for Au particles, Silane is used for silicon subtrates [52], and Ploy-L-Lysine for mica substrates [55]). Next, the mechanism of interatomic forces and dynamics should be understood for precise positioning of the particles [58]. However, the micro/nano mechanics for this kind of application has not been developed completely. Moreover, real-time monitoring of the manipulation process is almost impossible. Since the same tool is used as either the imaging or manipulation tool at an instant, imaging is not possible during pushing operation. As one approach to this problem, researchers scan the area, where the target particle is, before and after the manipulation [4], [37], [57], [26]. Thus, by using some fixed reference features, the new relative position of the particle is obtained from the images. However, this imaging is still off-line and the problems during pushing cannot be understood by this way. On the other hand, the other way is utilizing the force feedback information during pushing for reliable manipulation [67], [70]. Another approach may be using high-resolution external Scanning Electron Microscope imaging [39] while this can be done only in vacuum environments, tip and particle can be obscured, and only some specific particles can be imaged by this way.

In this chapter, possible solutions are proposed for the above challenging problems of AFM-based pushing. Force and dynamics modeling of the pushing operation, using real-time force feedback instead of real-time visual feedback or another external microscope during pushing, and using non-contact (tapping) imaging mode for imaging, and contact-mode for pushing are to be realized. A home-made AFM system with piezoresistive detection is constructed, and simulation and experimental results are compared for latex particle pushing applications.

7.2 Problem Definition

In this work, gold-coated latex particles absorbed on silicon substrates are to be pushed using a silicon fabricated AFM cantilever tip in ambient conditions as shown in Figure 7.1.

AFM-based pushing is realized by the motion steps as shown in Figure 7.2.

- $A \rightarrow B$ (*auto-parking*): the tip is automatically moved at z-direction until detecting the contact by the substrate by measuring the cantilever deflection (absolute tip-substate distance is not known initially), and retracted back to a predetermined parking position,

- $B \rightarrow C$ (*auto-particle contact detection*): the tip is moved along the substrate until detecting the particle by cantilever deflection detection, and then stopped,

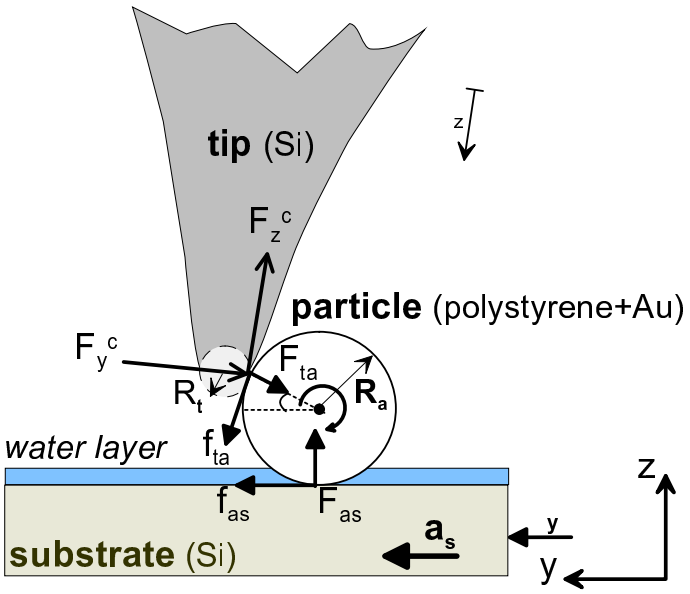

Figure 7.1: Positioning of the nano particles by the AFM tip contact pushing.

- $C \rightarrow D$: pushing the particle for a desired distance by moving the tip or the substrate with a constant speed,
- $D \rightarrow E$: after completing the pushing operation, retracting back to the initial height.

Spherical polyvinyl gold-coated latex particles with sizes around 50 nm - 2.02 μm are semi-fixed/absorbed to a Si substrate such that they are to be positioned by changing their xy positions. The particles are also called as *absorbates*. The operations are to be realized in open air conditions with high relative humidity. Thus, the sticking forces such as capillary and van der Waals are strong. Here, it is assumed that the electrostatic forces are negligible with respect to other forces.

The cantilever tip which has a radius $R_t \approx 25\ nm$ is being utilized in contact pushing and pulling of the particles. As shown in the Figure 7.1, the forces between the tip and particle and particle and substrate should be controlled such that the particles can be moved while not sticking to the tip. In the figure, F_{ta} and f_{ta} correspond to the tip-absorbate attractive/repulsive interaction force and friction force respectively. F_{as} and f_{as} are the interaction and friction forces for the absorbate and the substrate. The angle between the contact point of the tip and particle center is represented as β. The tip is aligned with an angle α. The tip is placed above the substrate with the parking height equals to the radius of the particle R_a. Thus, it is assumed not to touch to and interact with the substrate. By this way, the tip is not deformed, and vertical sticking

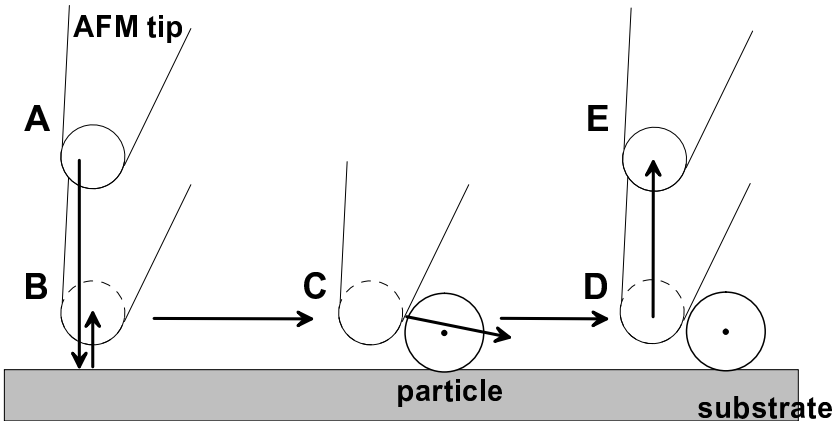

Figure 7.2: AFM-based particle pushing strategy.

force between the tip and particle is reduced.

Here, not the tip base but the substrate is moved with a constant speed V, and the manipulation strategy is as follows: *get the image of the particles using a non-contact type imaging device (OM or non-contact AFM imaging), then use the fixed cantilever as a stopper while moving the substrate under the particle with a uniform speed.* For fixing the particles, following conditions should be held:

- *at non-contact:* when the tip approaches or retracts from the particle, the particle should not stick to the tip and not move such that

$$\begin{aligned} F_{ta}sin\beta &\leq F_{as}, \\ f_{as} &\geq F_{ta}cos\beta, \end{aligned} \tag{7.1}$$

- *at contact:* when the tip contacts with the particle the resulting pushing or pulling force should be enough to fix the particle without breaking the tip or particle such that

$$\begin{aligned} f_{ta}cos\beta + F_{ta}sin\beta &\geq F_{as}, \\ f_{as} &\leq F_{ta}cos\beta - f_{ta}sin\beta. \end{aligned} \tag{7.2}$$

The aim is to design the control parameters such as the contact point, cantilever mechanical properties, particle-substrate friction, adhesion forces, humidity level and motion speed so that the above conditions can be held.

7.3 Requirements for Reliable Micro/Nanoparticle Pushing

During the manipulation of a nano object using an AFM probe, the interacting forces are shown in Figure 7.1. All of these forces should be modeled, and the dynamical analysis of the manipulation should be conducted for improving general design rules and strategies. The forces consist of adhesive forces (van der Waals, capillary and electrostatic forces), contact deformation forces, frictional forces, and triboelectrification forces (charge induction on the objects during pushing due to the substrate friction). Modeling of these forces in the spherical particle pushing case is given later. From these models, the conditions for a reliable contact pushing of any object are driven as follows:

1. Objects should be precisely movable by contact pushing on the substrate reducing friction between particle and substrate:

   (a) Depositing lubricant monolayer on the substrate, i.e. for a Au object, Silane monolayer on a Si substrate, and Polylysine layer on a Mica [58],

   (b) Minimizing the particle-substrate adhesion (friction is function of external load plus adhesive force at the nano scale [71]):

      i. Selecting proper material types (minimal surface energies),

      ii. Reducing the adhesive forces such as capillary force by reducing the humidity level or coating the tip by teflon, or electrostatic force by grounding the tip and substrate, and etc.,

   (c) Proper cantilever selection:

      i. high stiffness (10s of N/m) for pushing stability (applying enough load for pushing and breaking the adhesion force during separation from the object after manipulation),

      ii. hard tip (Si or Si_3N_4),

   (d) Contact point/angle selection (for applying maximum shearing force such that the horizontal line passing through the object center in spherical particle case),

   (e) High motion accuracy (for precise positioning during pushing): closed-loop positioners for reducing hystheresis and drift effects, reducing environmental noise sources (vibration, thermal changes, and etc.), and selecting low thermal conductivity materials on the mechanical parts for reducing the thermal drift,

2. Objects should not stick to the tip while retracting the probe after manipulation: (tip-particle adhesion) < (particle-substrate adhesion) :

   (a) small tip radius (few 10s of nm) with hard material: small contact area,

   (b) manipulation in liquid (reduces capillary and electrostatic forces),

   (c) tip or particle coating for reducing adhesion forces (latex particles are coated with Au for reducing adhesion due to triboelectrification [70]).

However, some of conditions have trade-offs. Conditions 1.b and 2 are opposite, then a between optimum particle-substrate adhesion should be designed. Secondly, Condition 1.c.i results in reduction of force measurement sensitivity such that smaller stiffness means higher force resolution. These trade-offs can be solved depending on the priority in a specific application.

7.3.1 Micro/Nano Forces During Pushing

The interatomic forces $F_{ta}(t)$ between the AFM tip and particle, and F_{as} between the particle and subtrate in the ambient conditions are to be modeled for understanding the pushing mechanism. For converting the spherical tip and flat surface models proposed models in Chapter 6 into the sphrical tip and a spherical particle case, **Derjaguin approximation** is to be used. In this approximation, assuming that the range of forces and separation distances are much shorter than the reduced radii of two spheres, R_t and γ_L in the force equations in Chapter 6 are changed into:

$$\begin{aligned} &R_t \rightarrow \tilde{R} = R_t R_a/(R_t + R_a) \ , \\ &\gamma_L \rightarrow \gamma_L/2 \ . \end{aligned} \tag{7.3}$$

Thus, the following equations are held for F_{ta} and F_{as}:

$$F_{as} = -4\pi R_a \gamma_L + \tfrac{4}{3}\sqrt{R_a} K_{as}(a_0 - \Delta)^{3/2} \ , \tag{7.4}$$

$$F_{ta} = \begin{cases} \sim 0 \ , & \text{if } h > 100\ nm; \\ -F_0\left(\frac{\sigma^2}{h^2} - \frac{\sigma^8}{30h^8}\right) - \frac{\epsilon_0 U^2 S}{2h^2} \ , & \text{if } 100\ nm \geq h > L\ nm; \\ -F_0\left(\frac{\sigma^2}{h^2} - \frac{\sigma^8}{30h^8}\right) - 2\pi\gamma_L\tilde{R}(1 - \frac{h-2e}{2r_1}) - \frac{\epsilon_0 U^2 S}{2h^2} \ , & \text{if } L \geq h > h^*; \\ -F_0\left(\frac{\sigma^2}{h^2} - \frac{\sigma^8}{30h^8}\right) - 2\pi\gamma_L\tilde{R}(1 - \frac{h-2e}{2r_1}) \ , & \text{if } h^* \geq h \geq a_0; \\ -2\pi\tilde{R}\gamma_L + \frac{4}{3}\sqrt{\tilde{R}} K_{ta}(a_0 - h)^{3/2} \ , & \text{if } h < a_0; \end{cases} \tag{7.5}$$

where Δ is the cantilever displacement from the particle-substrate contact point, $L = L_l$ during approaching and $L = \delta$ during retraction which is explained in Section

6.3.2, h^* is the threshold separation distance for electrostatic forces, $K_{ta} = \{(1 - \nu_t^2)/E_t + (1 - \nu_a^2)/E_a\}^{-1}$ and $K_{as} = \{(1 - \nu_a^2)/E_a + (1 - \nu_s^2)/E_s\}^{-1}$ are the reduced Young Modulus for the tip-particle and particle-substrate respectively. Here, since it is mathematically easy to deduce, the repulsive forces due to the elastic deformation are computed using the Hertz model assuming a high applied load. However, MD model is also used during simulations by using the numerical techniques to solve the parametric equations. Furthermore, after the separation distance of 100 nm, interatomic forces are assumed to be zero since the retardation effects reduce the van der Waals forces to almost zero, and electrostatic forces decay with the distance square speed.

7.3.2 Sample Preparation

Preparation of dispersed nanoparticles is a challenging issue, and JEOL Co. particles which are dispersed with a scattering gun on a silicon substrate is utilized for the experiments.

As the design issue, the above forces should be checked for the selected particle and substrate geometry and material type, and environmental conditions such that:

- during tip-particle approach and separation, the adhesion forces should not result in sticking of the particles to the tip,
- static frictional forces should be smaller than the applied load in order to be able to move a particle.

More detailed analysis results in following conditions for helding above features:

$$R_a > 0.5\tilde{R}sin\beta \ , \tag{7.6}$$

$$\mu_{as}^s \geq \frac{\tilde{R}cos\beta}{2R_a} = \frac{cos\beta}{2(1+R_a/R_t)} \ . \tag{7.7}$$

where μ_{as}^s is the static friction coefficient for particle-substrate interaction. First equality is always correct which shows the advantage of the sharp parabolic (spherical) tip apex structure. For the second one μ_{as}^s is calculated depending on R_a where $R_t = 30\ nm$ is fixed in our system. For $R_a = 10\ nm$, $\mu_{as}^s \geq 0.014$, and for $R_a = 1000\ nm$, $\mu_{as}^s \geq 0.35$. Here, μ_s cannot be selected arbitrarily since then the particle may not be pushed. For reducing this problem, μ_{as}^s should be selected as $\mu_{as}^s \approx cos\beta/2(1 + R_a/R_t)$, and a stiff cantilever should be used for enough pushing load.

7.3.3 Pushing Mechanism

For simplifying the notations and graphs, the particle is assumed to be pushed along y-axis where same notation and models can be extended to the x-y motion case directly.

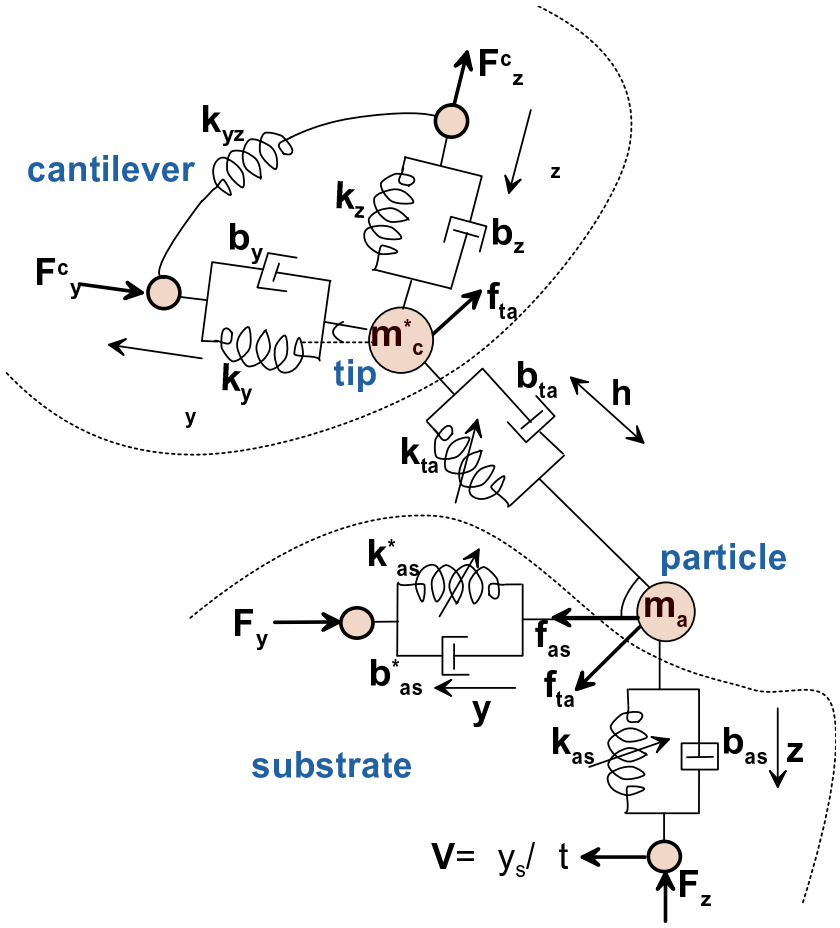

Figure 7.3: Point-mass model of the contact pushing mechanism (yz-axes view only).

The interacting forces during pushing are shown in Figure 7.3. The parameters shown in the model are given as follows: $k_z = k_c$, $k_y = k_c/c_2$, $k_{xy} = k_c/c_3$, $b_z = b_y = 2\pi f_r m_c^*/Q_c$ where f_r is the cantilever resonant frequency and Q_c is the quality factor in air, $m_c^* = k_z/(4\pi^2 f_r)$ is the cantilever effective mass, m_a is the particle mass, $V = dy_s/dt$ is the *constant* y-stage speed, h is the tip-particle indentation depth, $k_{as}^* = 8R_a G^*$ with $G^* = ((2-\nu_a)/G_a + (2-\nu_s)/G_s)^{-1}$ where G_a and G_s are the shear modulus for the particle and substrate respectively, $k_{ta} = -\partial F_{ta}/\partial h$, b_{ta} is the tip-particle damping term which is negligible, $k_{as} = -\partial F_{as}/\partial z$, b_{as} is the particle-substrate damping, $k_{as}^* = 0.85 k_{as}$ [54], and $b_{as}^* \approx 0$.

During the pushing operation, there are two main phases: static friction and kinetic friction regions. At the beginning, due to the satic friction, the particle and tip follow the stage motion along y-axis until to the point where the applied cantilever load exceeds the static friction between the particle and substrate. In this region following equations

are held at the equilibrium points assuming a slow motion:

$$
\begin{aligned}
f_{as} &= F_y^c cos\alpha + F_z^c sin\alpha \ , \\
f_{as} &= \mu_{as}^s(y)(F_{as} + A_{as}) \ , \\
F_{as} &= F_y^c sin\alpha - F_z^c cos\alpha \ , \\
F_y^c &= k_y y cos\alpha \ , \\
F_z^c &= k_z y sin\alpha \ , \\
F_y &= k_{as}^* y \ .
\end{aligned} \tag{7.8}
$$

Here, $\zeta_y \approx ycos\alpha$, $\zeta_z \approx ysin\alpha$, $y = y_s$, $z = \delta$ from the JKR model using Eq. (6.16) with $P_z = F_{as}$. At the shearing point $y = y^*$, $f_{as} = \mu_{as}^s(F_{as}(y^*) + A_{as}) = F_y(y^*)cos\alpha + F_z(y^*)sin\alpha$. Then y^* can be computed as

$$
y^* = \frac{\mu_{as}^s 4\pi R_a \gamma_L}{k_y cos^2\alpha + k_z sin^2\alpha - \mu_{as}^s sin\alpha cos\alpha (k_y - k_z)} \ . \tag{7.9}
$$

From this relation, the condition for enabling the particle pushing can be given as $y^* \geq 0$ which means that $\mu_{as}^s \leq (k_y cot\alpha + k_z tan\alpha)/(k_y - k_z)$. For example, for $\alpha = 15^o$, $k_z = 8\ N/m$ and $k_y = 1427\ N/m$, $\mu_{as}^s \leq 3.45$. Connecting this equality with Eq. (7.7):

$$
\frac{cos\beta}{2(1 + R_a/R_t)} \leq \mu_{as}^s \leq \frac{k_y cot\alpha + k_z tan\alpha}{k_y - k_z} \ . \tag{7.10}
$$

After the particle is separated from the substrate surface, following cases may occur: pure sliding, stick-slip motion and rolling. At this phase, $f_{as} = \mu_{as}^k F_{as}$ where μ_{as}^k is the kinetic friction coefficient, and the main dynamics of the particle or tip due to the constant $V = dy_s/dt$ speed can be obtained as follows:

$$
\begin{aligned}
&m_c^* \ddot{\zeta}_y + b_y \dot{\zeta}_y + k_y \zeta_y = F_y^c + F_z^c c_3/c_2 \ , \\
&m_c^* \ddot{\zeta}_z + b_z \dot{\zeta}_z + k_z \zeta_z = F_z^c + F_y^c c_3 \ , \\
&I_0 \ddot{\theta} = (f_{as} - f_{ta}) R_a \ , \\
&m_a \ddot{y} + b_{as}^* \dot{y} + k_{as}^* y = f_{as} + f_{ta} sin\beta - F_{ta} cos\beta \ , \\
&m_a \ddot{z} + b_{as} \dot{z} + k_{as} z = F_{as} - F_{ta} sin\beta - f_{ta} cos\beta \ , \\
&f_{as} = F_{ta} cos\beta - f_{ta} sin\beta \ , \\
&F_{as} = F_{ta} sin\beta + f_{ta} cos\beta \ , \\
&F_y^c = k_y cos\alpha y - F_{ta} cos\gamma + f_{ta} sin\gamma \ , \\
&F_z^c = k_z sin\alpha y - F_{ta} sin\gamma - f_{ta} cos\gamma \ ,
\end{aligned} \tag{7.11}
$$

where $I_0 = 2m_aR_a^2/5$ is the moment of inertia of the particle, and $\gamma = \beta - \alpha$. From these equalities, assuming no rolling ($\ddot{\theta} = 0$) and $h \approx 0$, at the steady state:

$$
\begin{aligned}
&\zeta_y = F_y^c/k_y + F_z^c/k_{yz} \ , \\
&\zeta_z = F_z^c/k_z + F_y^c/k_{yz} \ , \\
&f_{as} = f_{ta} \ , \\
&F_{ta} = \mu_{as}^k(\mu_{ta}^k cos\beta A_{ta} + A_{as})/ \\
&(cos\beta/(1+sin\beta) - \mu_{as}^k(\mu_{ta}^k cos\beta + sin\beta)) \ , \\
&f_{ta} = F_{ta}cos\beta/(1+sin\beta) \ , \\
&y = \zeta_y cos\alpha + \zeta_z sin\alpha + \Delta y \ , \\
&\Delta y = (\zeta_y sin\alpha - \zeta_z cos\alpha)sin\beta cos\beta \ , \\
&\Delta z = (\zeta_y sin\alpha - \zeta_z cos\alpha)sin^2\beta \ , \\
&\tilde{\beta} = arctan\{(R_a sin\beta + \Delta z)/(R_a cos\beta - \Delta y)\} \ , \\
&F_z = k_y\zeta_y sin\alpha - k_z\zeta_z cos\alpha \ , \\
&z = \delta(\tilde{\beta}) \ .
\end{aligned}
\tag{7.12}
$$

7.4 Force-Controlled Pushing

Using the real-time ζ_z feedback during pushing, following force-controlled pushing strategies can be proposed: z-position , xy-position, or xyz-position controlled pushing. The xy-position controlled pushing control scheme is shown in Figure 7.4. The main design variable is the reference (x_r, y_r) position value. For a 2-D pushing-based positioning (x_r, y_r) is selected as $(x(0), y(0))$ where $x(0)$ and $y(0)$ are the after automatic contact detection particle (x, y) position since the stage and particle move, and the cantilever tip behaves as the stopper. Here, H_{xy} function transforms the deflection and position data to the particle position (x_a, y_a) feedback such that:

$$
H_{xy} = \begin{cases} (x, y) = (x_s, y_s) \ , & \text{if } t \leq t^*; \\ (x, y) = (x^o, y^o) \ , & \text{otherwise.} \end{cases}
\tag{7.13}
$$

Here, (x_s, y_s) is the stage xy-position, t^* is the particle-substrate separation instant, and (x^o, y^o) is the tip-particle pushing settling xy-position. t^* can be detected experimentally in real-time by observing ζ_z such that if ζ_z has a peak at time t, then $t^* = t$. However, (x^o, y^o) cannot be measured directly, and needed to be estimated from the pushing model. For example, using the previous models, y^o can be observed in the Figure 7.5 where x^o can be observed in the same way. However, depending on the special parameters, the behaviour of the (x, y) could be also periodic motion, which

can be observed in the model and experiments. In this case, the mean of the periodic function can be used as the (x, y) information.

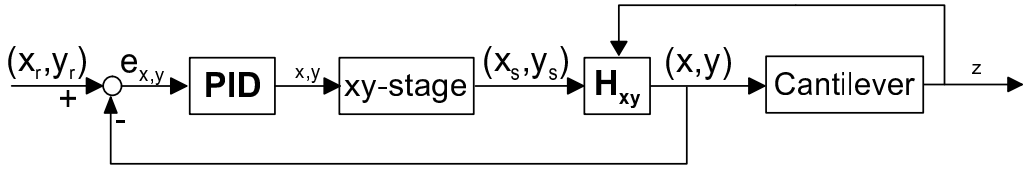

Figure 7.4: Force-controlled xy-positioning during particle pushing.

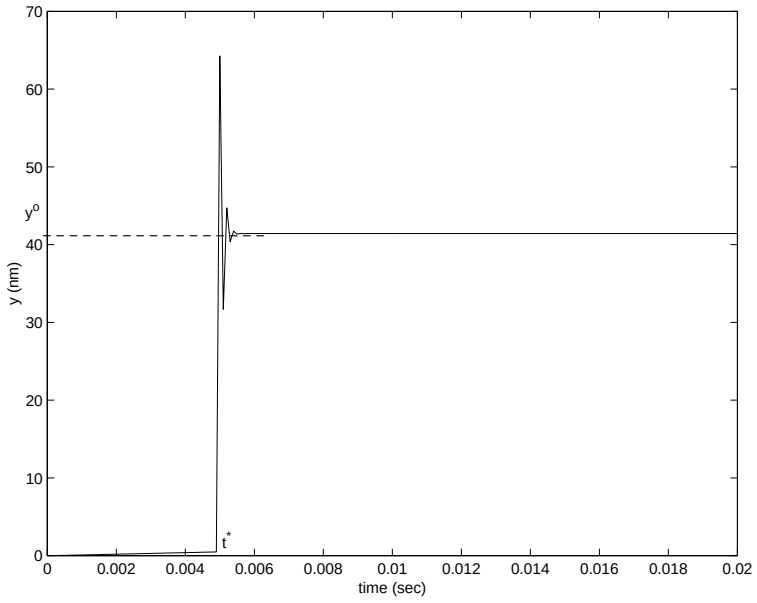

Figure 7.5: The settling of the y position of the particle during pushing.

7.5 2-D Micro/Nanoparticle Assembly

7.5.1 Direct Teleoperation User Interface

In the case of nanoparticles, a direct teleoperation system which is the same as in Chapter 6 is utilized for pushing the particles. Mainly the force reflecting servo type controller is used during the pushing operation for the real-time force feedback of the tip-particle interaction force, and also initial alignment contact detection and parking.

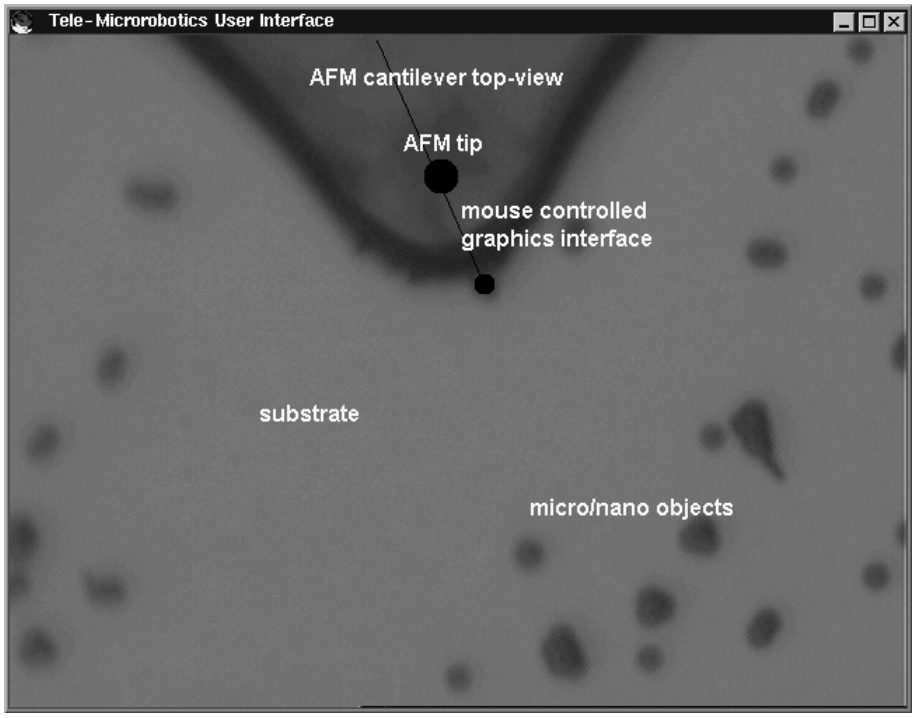

Figure 7.6: Task-based microparticle pushing interface display consisting of the real-time images of the top-view optical microscope.

7.5.2 Task-Based Teleoperation User Interface

For the microparticles of $R_a \geq 1\ \mu m$, optical microscope is enough for real-time visual feedback. Thus, the PC monitor optical microscope image window can become a kind of touch panel by using the mouse cursor clicks. Therefore, a task-based teleoperation control becomes more feasible where an example display of task-based micorparticle pushing interface is shown in Figure 7.6. In this interface, AFM is utilized in following ways:

- the alignment error of the substrate can be compensated by getting a contact 3-D topology planar image of the substrate along single x and y lines where there is no particle,
- the contact point between the tip and the particle can be detected by measuring ζ since it will change if there is a contact.
- the initial z-position of the tip above the substrate is set by contacting and retraction of the sample to the tip.

Selection of the Particle

The operator clicks any (x, y) point on the particle. Assuming that the approximate maximum pixel area of the particle $L_x \times L_y$ is known (it is learned by preliminary tests), a window is created with left-up corner $(x - L_x, y - L_y)$ and right-bottom corner $(x + L_x, y + L_y)$. Inside of this window each pixel (i, j) with the color light intensity I_{ij} is checked such that:

initially, $m_x = m_y = n = 0$,

for all (i, j)s inside of the window:

if $I_{ij}^{red} > T_p$ and $I_{ij}^{blue} > T_p$ and $I_{ij}^{green} > T_p$

$$\begin{aligned} m_x &= (m_x + i)/(n+1), \\ m_y &= (m_y + j)/(n+1), \\ n &= n + 1, \end{aligned}$$

where m_x and m_y are particle center x and y positions, n is the number of detected particle pixels, and T_p is the threshold which is determined by the operator previously. Thus $x_O = m_x$ and $y_O = m_y$ are computed.

Coordinate Frame Calibration

Image to world coordinates transformation constitutes of scaling and rotation transformations, and it is calibrated before the experiments. For this purpose, a selected particle is tracked automatically during a controlled x-y motion. Particle detection image processing part is the same with the selection of the particle procedure. As an example, a scanning motion with 1 μm steps and 0.1% hystheresis error results in the particle center positions as shown in Figure 7.7. The positions have some noise and deformation due to the horizontal table vibration, and nonhomogenous lighting.

From the figures, the rotation angles ϕ and γ for the x and y axes, and scaling factor s are computed. Then, the pixel to μm position trasformation is as follows:

$$\begin{aligned} &\mathbf{x_{\mu m}} = \mathbf{A}\mathbf{x_p}, \\ &\mathbf{A} = \begin{bmatrix} -scos\phi & ssin\gamma & 640scos\phi \\ ssin\phi & scos\gamma & -640ssin\phi \\ 0 & 0 & 1 \end{bmatrix}, \\ &\mathbf{x_{\mu m}} = [x_{\mu m} \quad y_{\mu m} \quad 1]^T, \\ &\mathbf{x_p} = [x_p \quad y_p \quad 1]^T. \end{aligned} \tag{7.14}$$

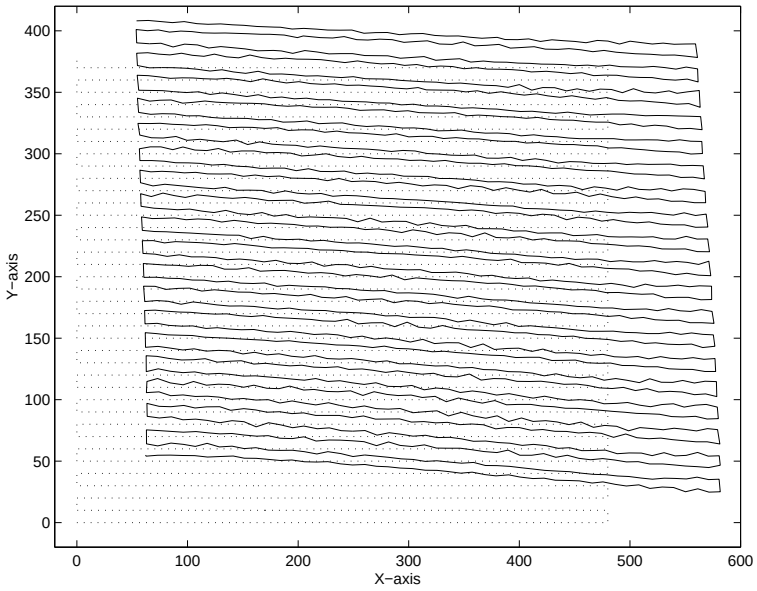

Figure 7.7: Controlled x-y scanning of the Stage I, and resulting detected particle center positions.

Surface Alignment Calibration

Since the fine motion XYZ stage motion axes and the sample surface may not be parallel to each other, the orientation errors or differences should be compensated for a reliable manipulation. For this purpose, the surfaces are scanned through two scan lines through x and y axes separately as can be seen in Figure 7.9, and AFM contact mode imaging has enabled the z data of those lines which can be used to calculate the orientation angles ϕ_x and ϕ_y as can be seen in Figure 7.10.

Tip Position Calibration

Since the OM images are top-view images, the AFM cantilever tip which is at the bottom inside part of the cantilever cannot be seen directly by the microscope. Also, since the position of the tip can differ for each cantilever, a calibration procedure for each cantilever is necessary before the pushing experiments. For this purpose, initially a particle is aligned closely to the end of the cantilever end as can be seen in Figure 7.8. The particle center position in the image coordinates is calculated by clicking on it where the automatic particle center detection algorithm computes the exact center position. Then, by a tapping mode scanning of the sample by an enough range (approximately $15\mu m \times 15\mu m$), the particle center is found inside of the AFM grey-scale topology image automatically by thresholding the height data, and averaging those thresholded data.

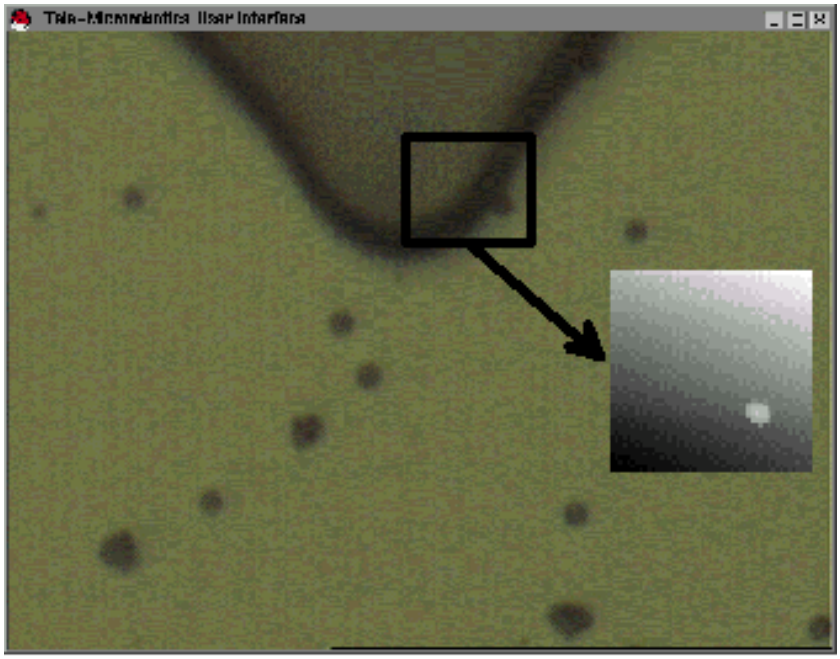

Figure 7.8: Automatic tip center position calibration using the tapping mode AFM imaging and selecting a particle close to the end of the cantilever end with a known center position in the image coordinates.

Thus, the tip center position (x_M, y_M) is computed as:

$$\begin{aligned} x_M &\approx x_O - \frac{x_O^{\mu m}}{s} \ , \\ y_M &\approx y_O - \frac{y_O^{\mu m}}{s} \ , \end{aligned} \tag{7.15}$$

where $(x_O^{\mu m}, y_O^{\mu m})$ are the particle center position in the tapping mode AFM image coordinate frame as the micrometer values computed from the distance of the particle center to the image left-up corner origin point, and s is the micrometer to pixel transformation scaling factor ($s \approx 0.091\ \mu m/pixel$ in our setup).

User Interface

The user interface constitutes of the real-time display of the top-view images from the camera mounted on the OM. The operator uses the mouse cursor and keyboard for defining the tasks for the micromanipulator (AFM) controller. At present there are three main tasks:

- *Task 1 (T1)*: position the tip above the substrate,

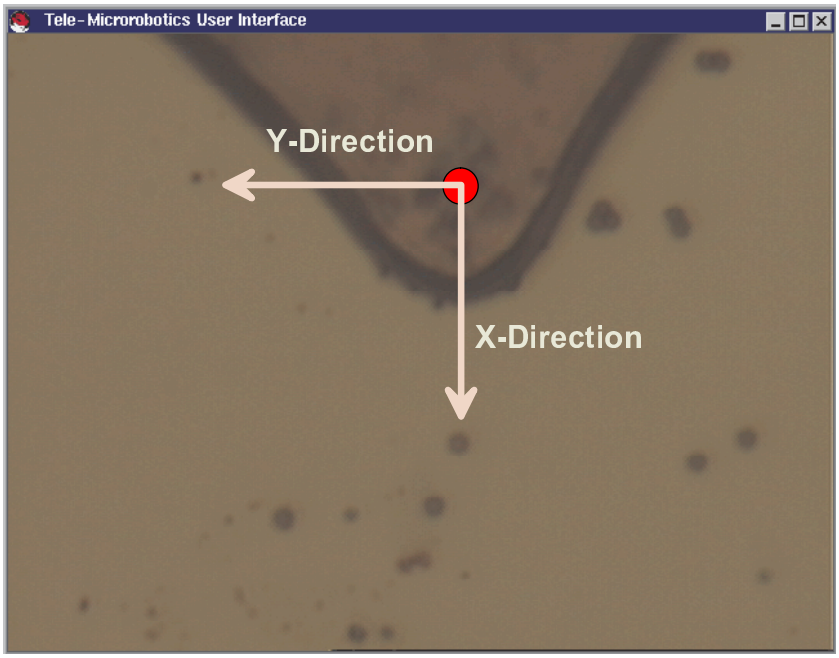

Figure 7.9: Surface and XYZ-stage motion axis orientation calibration by getting the contact mode images of the shown xy-directions, and computing the orientation angles.

- *Task 2 (T2)*: point-to-point motion,
- *Task 3 (T3)*: automatic pushing or pulling.

At the task T1, the tip is set to the height of R_a above from the substrate automatically. For this, the substrate is moved along the z-direction until touching to the tip, i.e. tip deflection is measured as ζ_{set}, then retracted back to the z-position given as $z = z_{final} - h_{set}$ where $h_{set} = R_a$ as shown in Figure 7.11.

In the task T2, the operator points the first point and the target point to be moved by the mouse cursor. Then the positon controller automatically moves with the amount of relative distance between the two points. This operation is needed for searching and initially positioning the particles on the screen.

The task T3 is used for semi-autonomous particle pushing or pulling. Freezing the continuous image, the operator selects the particle to be moved by clicking on the particle. Using image processing, the particle center $\mathbf{O}$ is automatically located. Next, the target position $\mathbf{T}$ is clicked by the operator. Then the pushing or pulling operation is realized automatically as shown in Figure 7.12 by the following strategy:

- *Step 1:* the tip center position $\mathbf{M}$ and radius R_t, particle center position $\mathbf{O}$ and radius R_a, and the target position $\mathbf{T}$ are computed,

- *Step 2:* compute the relative distance and orientation between **O** and **T** such that

$$\begin{aligned} \Delta x &= x_T - x_O, \\ \Delta y &= y_T - y_O, \\ \theta &= tan^{-1}(|\Delta y|/|\Delta x|), \\ s_x &= \Delta x/|\Delta x|, \\ s_y &= \Delta y/|\Delta y|, \end{aligned} \tag{7.16}$$

- *Step 3:* find the point **P′** which is the initial set point before tip-particle contact such that

$$\begin{aligned} x_{P'} &= x_M + s_x R cos\theta, \\ y_{P'} &= y_M + s_y R sin\theta, \\ R &= R_t + 3R_a, \end{aligned} \tag{7.17}$$

- *Step 4:* move the tip $3R_a$ upward from the substrate for avoiding any possible collision between the tip and particle,
- *Step 5:* move from the point **O** to **P'**,
- *Step 6:* move back the tip to its parking height using T1,
- *Step 7:* if the substrate is not oriented paralelly to the x-y motion direction of the stage, the z-position of the tip can change; therefore, use the task T1 to reposition the tip on the substrate to d_{set},
- *Step 8:* find the contact point **P** by moving from **P'** through **M** by measuring the cantilever deflection,
- *Step 9:* find the point **S** where

$$\begin{aligned} x_S &= x_P - s_x \Delta L cos\theta, \\ y_S &= y_P - s_y \Delta L sin\theta, \\ \Delta L &= (\Delta x^2 + \Delta y^2)^{1/2}, \end{aligned} \tag{7.18}$$

- *Step 10:* move from **P** to **S**,
- *Step 11:* move from **P** to **T**.

7.5.3 System Setup

For conducting experiments, a home-made open-structure AFM system with Virtual Reality (VR) graphics display and haptic device is utilized [72]. Piezoresistive cantilevers where the cantilever has a doped silicon layer which changes its resistance due to the deflection moment are utilized. These type of cantilevers can be the future micro-robot grippers as the integrated sensor probes. Only the ζ_z is measurable with the present system. As the user interface, the VR Nano Visulator integrated with the 1-DOF haptic device is utilized. In the graphics display, scanned AFM images, and real-time cantilever tip position (spherical ball in the figure) are displayed. Using the haptic device, z-position of the tip can be controlled by the user with a real-time bilateral force feedback control. Thus, even there are positioning errors due to the piezoelectric stage on the visual display, the force-feedback enhances these types of errors.

7.5.4 Experiments and Simulations

As the first experiment, the contact point detection is tested. The cantilever parameters are $R_t = 30\ nm$, and $k_c = 8\ N/m$, $L_x = 50\ \mu m$, $L_y = 155\ \mu m$, and $L_z = 6.5\ \mu m$. The motion speed is around $V = 2\ \mu m/sec$ with $\Delta = 0.1\ \mu m$ steps. During the particle-tip contact as can be seen in Figure 7.15, $-0.2\ V$ is the no deflection line where around the 43^{th} step of motion the particle contacts and bends until to $-1.5\ V$ which is the ζ_{set} for automatic contact detection. At this point stage stops moving.

For the simulations, the proposed models are utilized such that the effect of different parameters cantilever deflection, and particle position is tried to be understood. During the simulations, if that parameter is not the changing one, the parameter values are selected as follows: $k_z = 8N/m$, $\mu^s_{as} = \mu^s_{ta} = 0.3$, $\mu^k_{as} = \mu^k_{ta} = 0.2$, $R_a = 1\ \mu m$, $R_t = 30\ nm$, $V = 1\ \mu m/sec$, $L_y = 155\ \mu m$, $L_z = 6.7\ \mu m$, $\alpha = 15^o$, $\beta = 30^o$, $\gamma_L = 72\ mJ/m^2$, $\nu_s = 0.27$, $\nu_t = 0.3$, $E_s = 169\ GPa$, and $E_t = 70\ GPa$. Assuming only pure-sliding case and contact point between the tip and particle is $y = 0$, at first, the tracking of the cantilever y and z deflection, and particle y and z positions are shown in Figure 7.13. During pushing, also the β values change as denoted by $\tilde{\beta}$ since the particle tip interface also moves due to the z motion of the cantilever and particle. This effect can be seen in Figure 7.14 where $\tilde{\beta}$ settles to a constant value after some time. Fastly, the positions track a constant value. the effect of the cantilever tilt angle α is observed. Here and after, all y and ζ_z values are the settled steady state values in the graphs. From Figure 7.16, it can be seen that within a limited range of α, ζ_z and y increase with the increased angle. Secondly, changing β tip-particle contact angle values, it can be deduced from the Figure 7.17 that optimum β can result in minimum y motion of the particle with a detectable range of ζ_z. Moreover, μas^s effect is tested as shown in Figure 7.18. From the figure, μ^s_{as} value around $0.6 - 0.7$ results in an unstable y and

ζ_z behaviour. Finally, the cange in R_a results in the effect as shown in Figure 7.19.

As the pushing experiment, 0.5 μm radius gold-coated latex particles are pushed in a task-based control user interface. The optical microscope images of an pushed particle example is given in Figure 7.22. During pushing, ζ_z measurement can be seen from the Figure 7.20. Since, the silicon surface is not perfectly flat, the deflection data is not horizontal, and it goes to zero by increasing the stage position. Also, particle is added to a line of particles successfully as shown in Figure 7.23.

As the next experiment, the automatic pushing of two particles to form a line shape is realized as shown in Figure 7.24. The automatic pushing results can be seen in the figure where the particles are positioned to the user-defined target points. During pushing, the motion of the cantilever tip can be seen from the Figure 7.21. Pushing can break the cantilever tip sometimes due to large loading. But this is prevented by checking the ζ during pushing such that if it exceeds $-10\,V$, which is also the saturation voltage of the amplifier, then the pushing is stopped, and the design of the particle and substrate should be changed according to the force analysis.

7.6 Tribological Characterization of Particle-Substrate Interfaces

In this section, the aim is to try to understand the tribological behaviour and properties of particle-substrate interfaces using the AFM-based pushing [20]. Understanding of this kind of behaviour can help in designing new lubricants, for example for hard disk technology, and new polishing materials for Chemical Mechanical Polishing technologies. In this study, especially micro/nano gold-coated latex particles are pushed on silicon substrates in order to understand their frictional behaviour. Assuming ambient conditions, frictional forces during detaching the latex particles from the silicon substrate are measured and possible behaviour with effecting parameters are determined.

For characterizing the frictional behaviour, the user interface should be task-based since the particle pushing velocity and other parameters are as much as controllable with a high precision. Therefore the task-based user interface in Section 7.5.2 is utilized in this application.

7.6.1 Frictional Behaviour Modeling

Since the home-made AFM system cannot measure torsional bending, the frictional forces are measured directly from the normal deflection where the particles are pushed along the y axis. Forces during pushing are the same as in Figure 7.1. Here, the important parameter is the coefficient of friction between the particle and substrate

μ_{as}. During the static friction phase, $\zeta_z = (sin\alpha + cos\alpha k_y/k_{yz})y$. Using the Eq. 7.9 of the separation point y^*, μ^s_{as} can be computed as follows:

$$\mu^s_{as} = \frac{k_c(cos\beta - \mu^s_{ta}sin\beta)\zeta^*_z}{(sin\beta - \mu^s_{ta}cos\beta)k_c\zeta^*_z + 4\pi R_a\gamma_L(sin\gamma + \mu^s_{ta}cos\gamma + (cos\gamma - \mu^s_{ta}sin\gamma)3L_z/(2L_y))} . \tag{7.19}$$

where ζ^*_z is the separation point cantilever z deflection. Experimentally ζ^*_z can be measured, and then μ^s_{as} can be predicted.

During pushing, the separation points of the particle from the substrate can be observed as ζ^*_z peaks [82]. These peaks are caused by the shearing of the contact points [46] during the separation such that at these maxima:

$$f^*_{as} = \kappa a^*_{as} = \mu^s_{as}(F_{as} + A_{as}) = c_\zeta \zeta^*_z , \tag{7.20}$$

where κ is the shear stregth of the contact points ($\kappa = 144 \times 10^6 N/\mu^2$ in the case of water layer between the particle and substrate), a_{as} is the contact area of the particle-substrate interface, and c_ζ is given as:

$$c_\zeta = \frac{k_c}{sin\gamma + mu^s_{ta}cos\gamma + (cos\gamma - \mu^s_{ta}sin\gamma)3L_z/(2L_y)} . \tag{7.21}$$

Thus, the important point is such that shear force linearly depends on the contact area and shearing z-deflection, and the experimental ζ^*_z data can be utilized for computing f^*_{as} and a^*_{as}.

7.6.2 Frictional Sliding Behaviour from the Deflection Data

After the shearing point, the kinetic frictional force and the applied loads and other parameters of the pushing such as k_c, α, β, R_a, R_t, L_y, L_z and V determine the sliding behaviour. The particles can roll, purely slide, have stick-slip motion, or have all these different behaviour during the same pushing operation. The interesting question here is: *Could we get the sliding behaviour by getting the z-deflection data after the shearing point?* From the models, assuming the particles are pushed through their center (for avoiding the rotational force and losing contact during pushing), the deflection data shape can give idea about the sliding behaviour such that:

- continuous linear shape can be pure sliding (Figure 7.25a),
- saw-like shape can be due to the stick-slip motion (Figure 7.25b),
- sinusoidal-like shape can be due to the rolling motion (Figure 7.25c).

7.6.3 Experiments

Spherical gold-coated 2 μm size latex particles are pushed on a Si surface. The initial and final positions of the particles are shown in Figure 7.26 where the selected particle is pushed around 11 μm distance with a short-time stop around at 32 μm x-position. The cantilever z deflection is shown in Figure 7.27. The two minimum points of the deflection show the shearing points during the initial motion and short stop. The force measured at this point can give the shearing force after some calculations [73], [70].

For the computation of the shearing force and static friction constant values, the deflection data in Figure 7.25a is analyzed. The peak deflection experimental value of $\zeta_z^* \approx 50\ nm$, and experimental values of $\alpha = 15^o$ and $\beta = 30^o$ result in the computed values of $f_{as}^* = 265\ nN$, $\mu_{as}^s = 0.05$ and $a_{as}^* = 24.2\ nm$ using Eq. (7.19), Eq. (7.20) and Eq. (7.21).

7.7 Conclusion

In this chapter, a micro/nanoparticle manipulation system using Atomic Force Microscope (AFM) as the manipulator has been proposed. Modeling and control of the AFM cantilever tip and particle interaction has been realized for moving gold-coated latex particles with sizes down to 484 nm on a silicon substrate in 2-D. Particle manipulation experiments are realized, and it is shown that the system can be utilized in 2-D micro/nano particle assembling, and as a particle-substrate tribological characterization tool. As the future work, the manipulation operations will be realized in a liquid environment where the capillary and electrostatic forces are reduced.

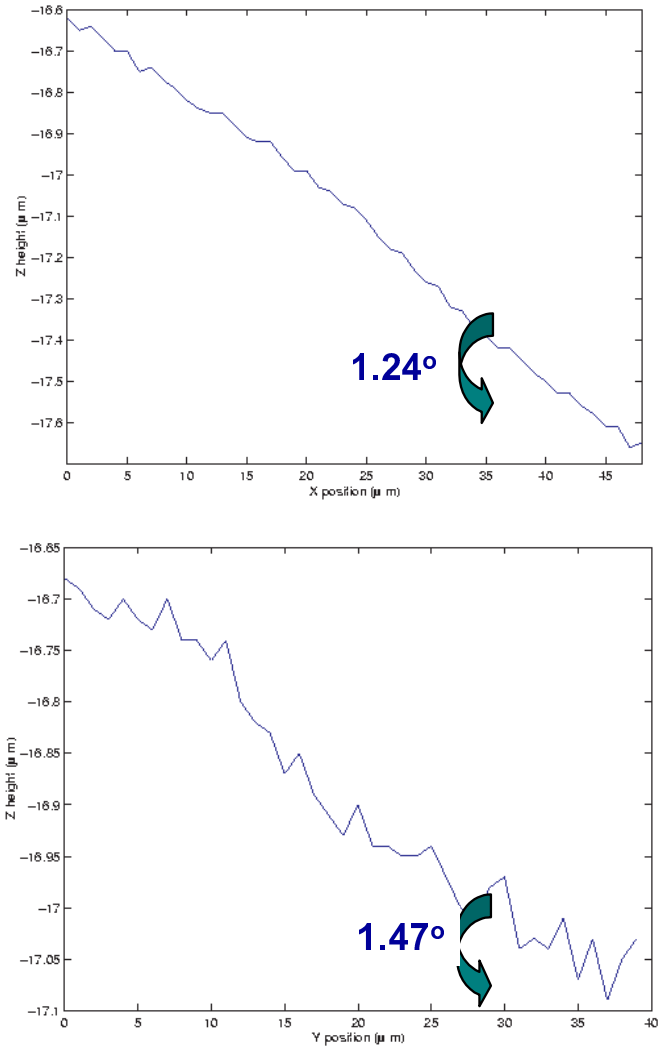

Figure 7.10: Measured x and y-axes orientation sample data consisting of the contact mode AFM detected height data.

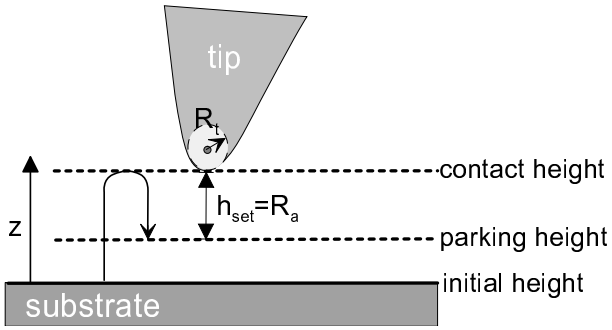

Figure 7.11: Parking height setting for the tip.

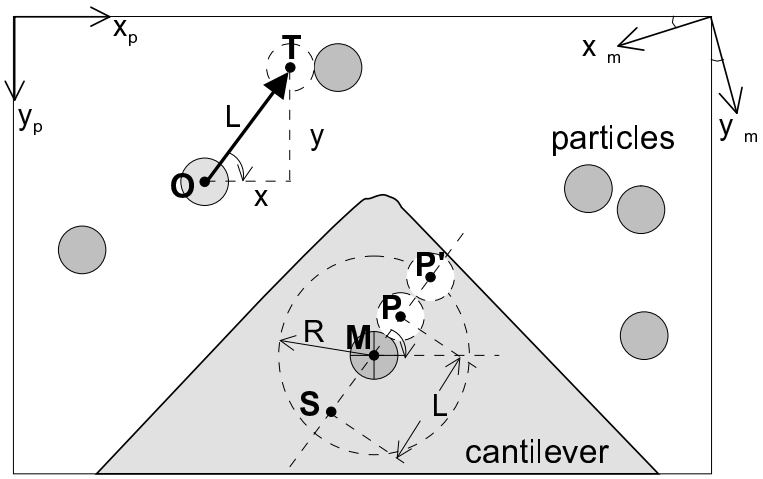

Figure 7.12: Automatic pushing or pulling operation, and image and positioner coordinates.

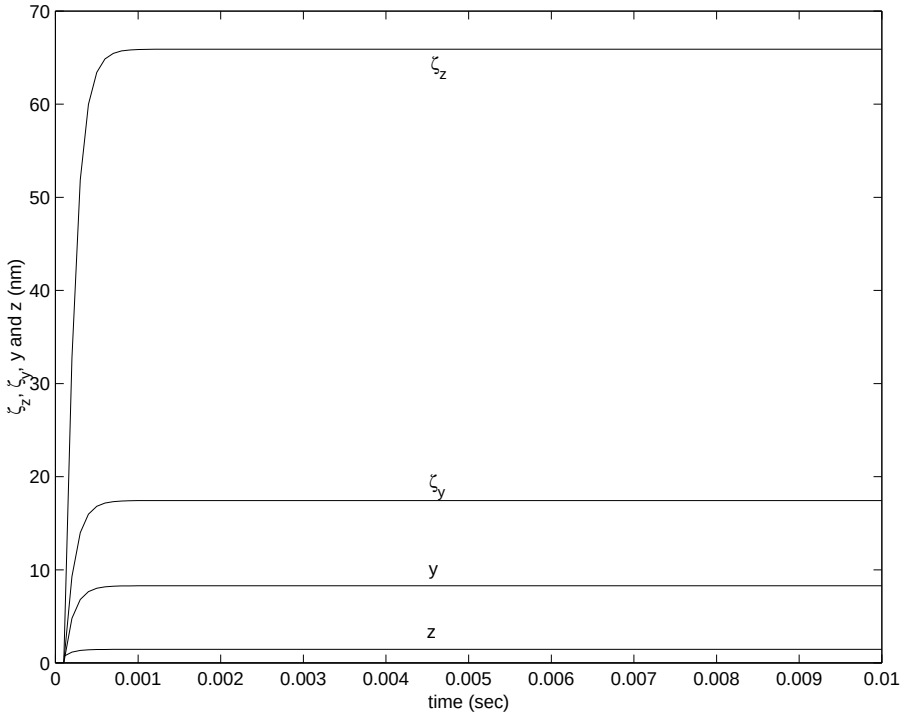

Figure 7.13: The settling of the y, z, ζ_z and ζ_y positions of the particle and cantilever during pushing.

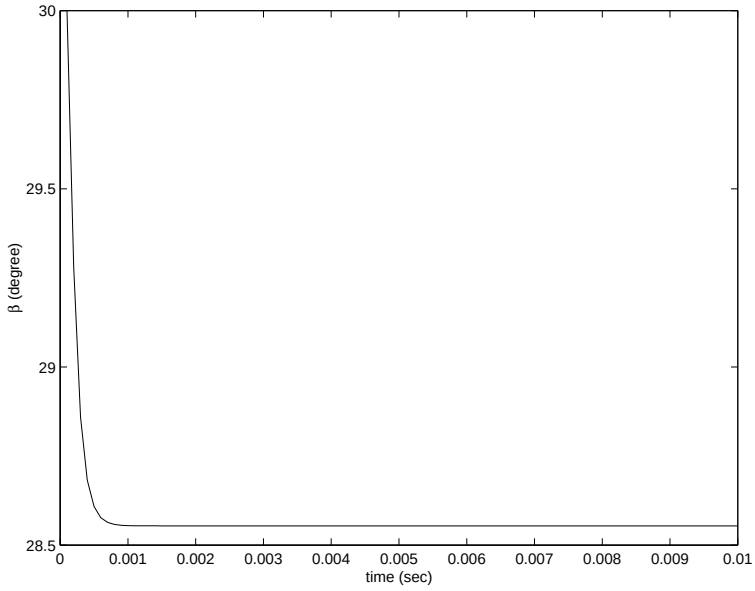

Figure 7.14: The settling of the β value where it can change due to the particle and tip z motion.

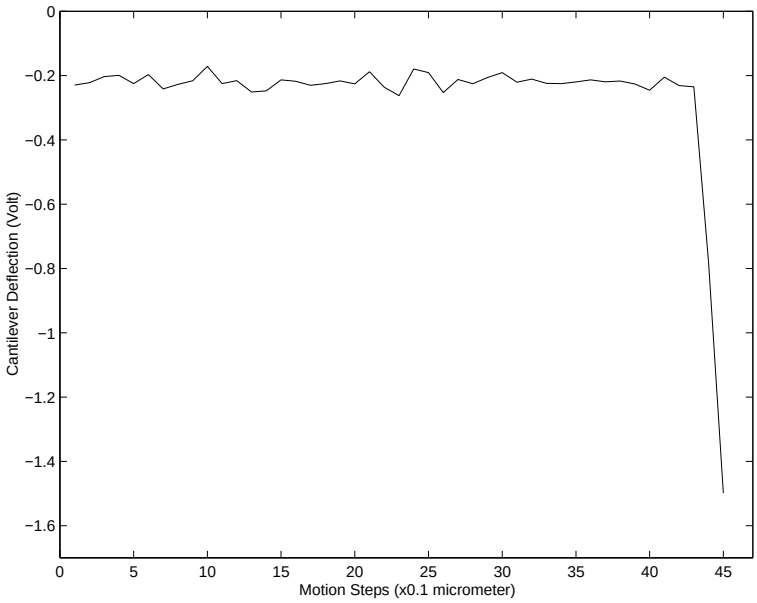

Figure 7.15: The experimental cantilever deflection during automatic contact detection.

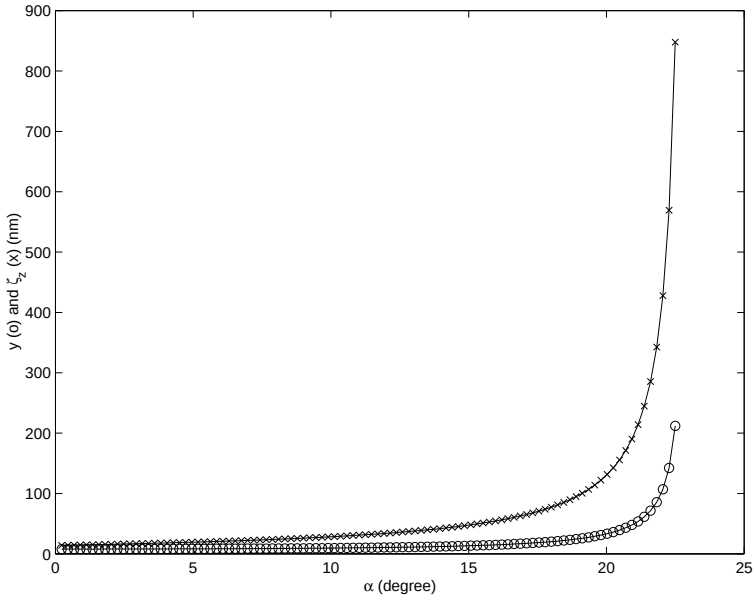

Figure 7.16: The effect of changing α on y ('o') and ζ_z ('x').

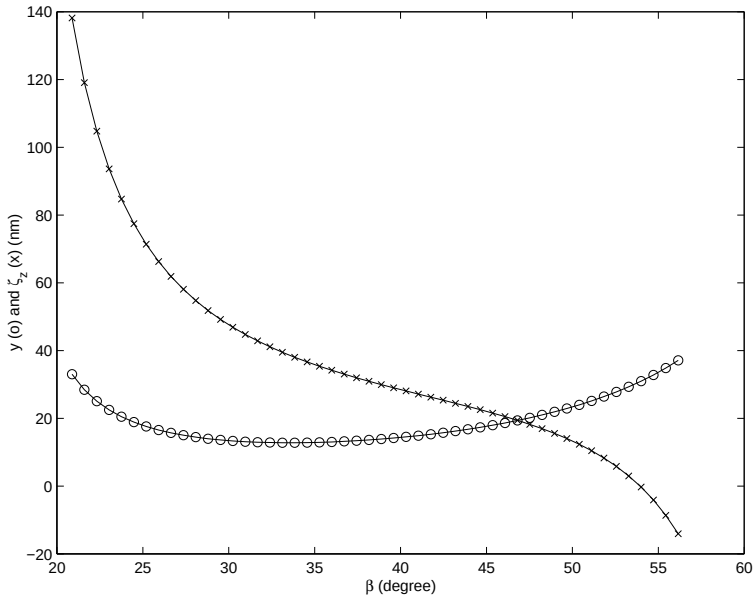

Figure 7.17: The effect of changing β on y and ζ_z.

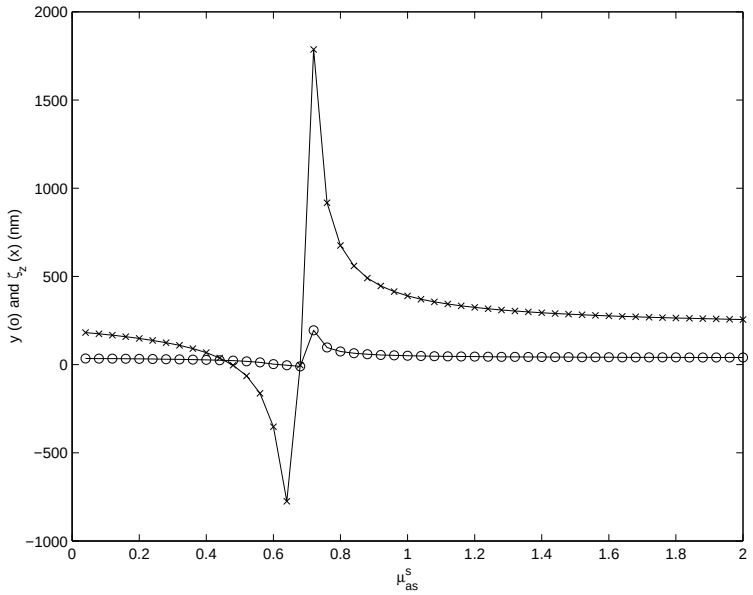

Figure 7.18: The effect of changing μ_{as}^{s} on y and ζ_z.

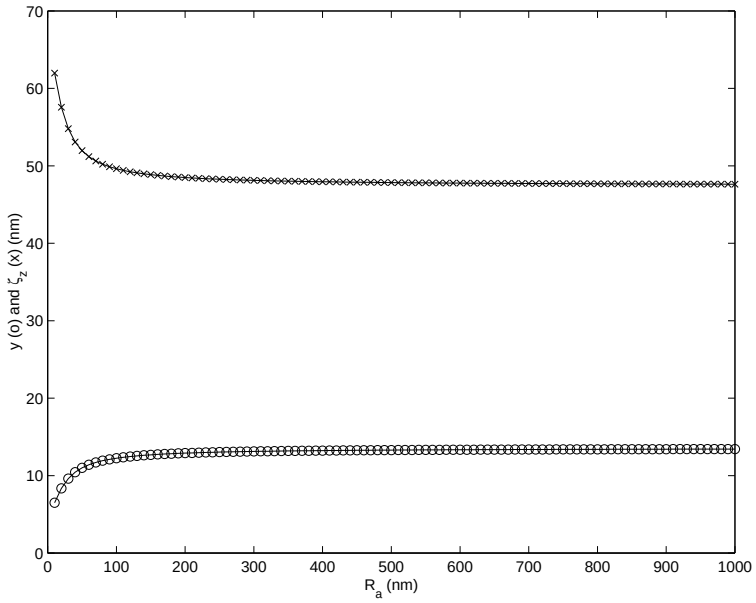

Figure 7.19: The effect of changing R_a on y and ζ_z.

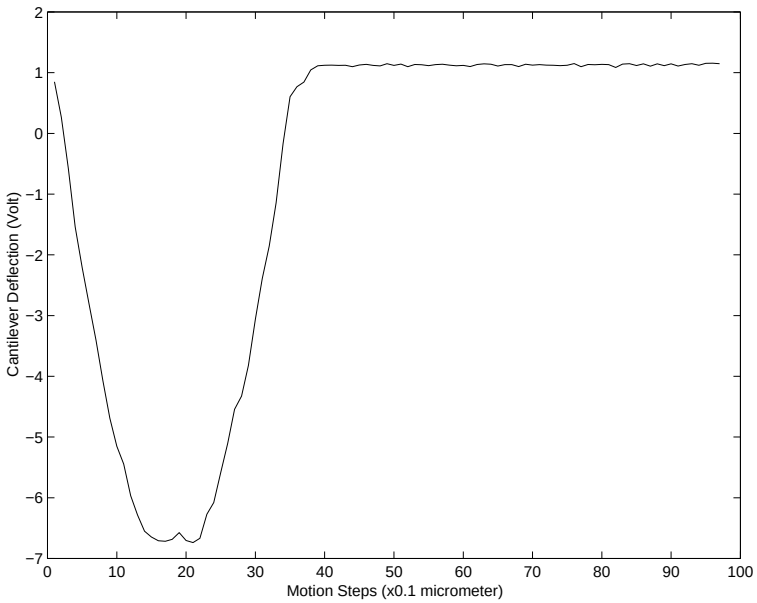

Figure 7.20: Experimental cantilever deflection data during pushing.

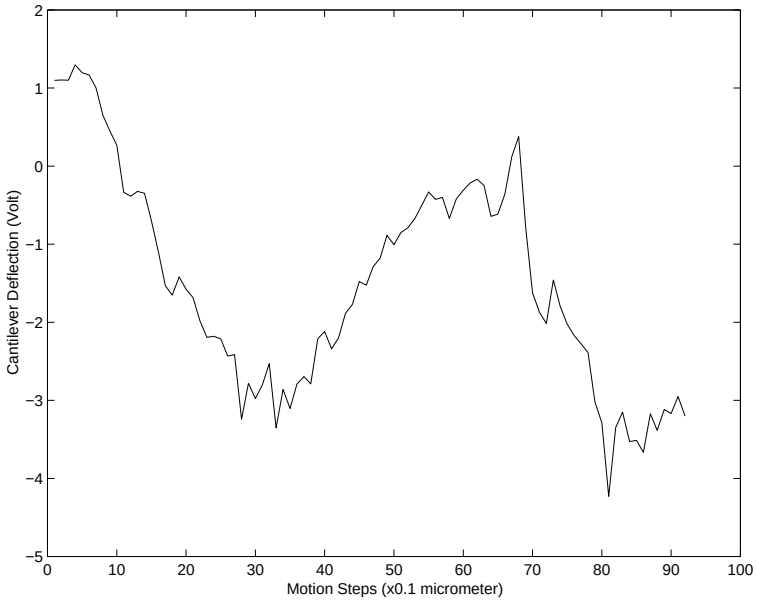

Figure 7.21: The cantilever deflection during pushing.

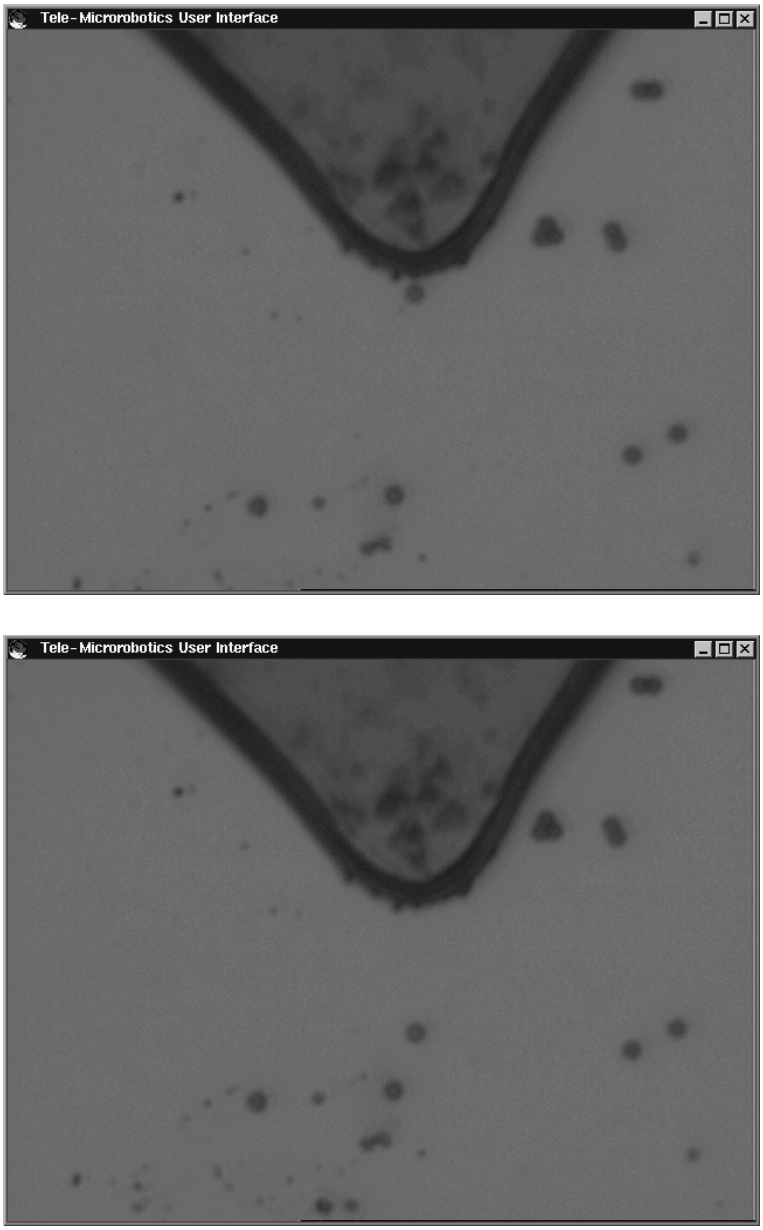

Figure 7.22: Pushing a 0.5 μm radius latex particle where the initial (upper image) and final positions (lower image) are shown using the high-resolution optical microscope top-view images.

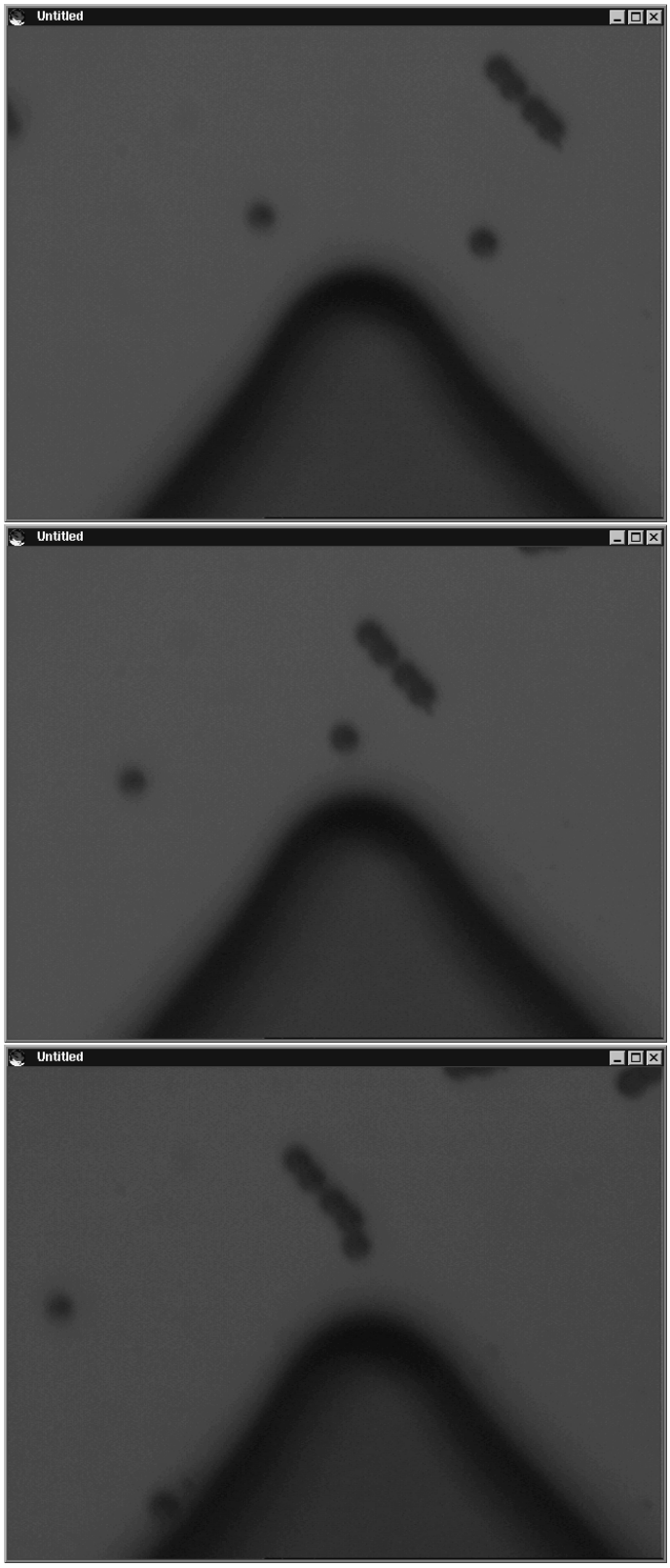

Figure 7.23: Image sequences of pushing a $2\mu m$ size particle by the steps shown above beginning from the initial position (uppermost) to the last configuration (bottom).

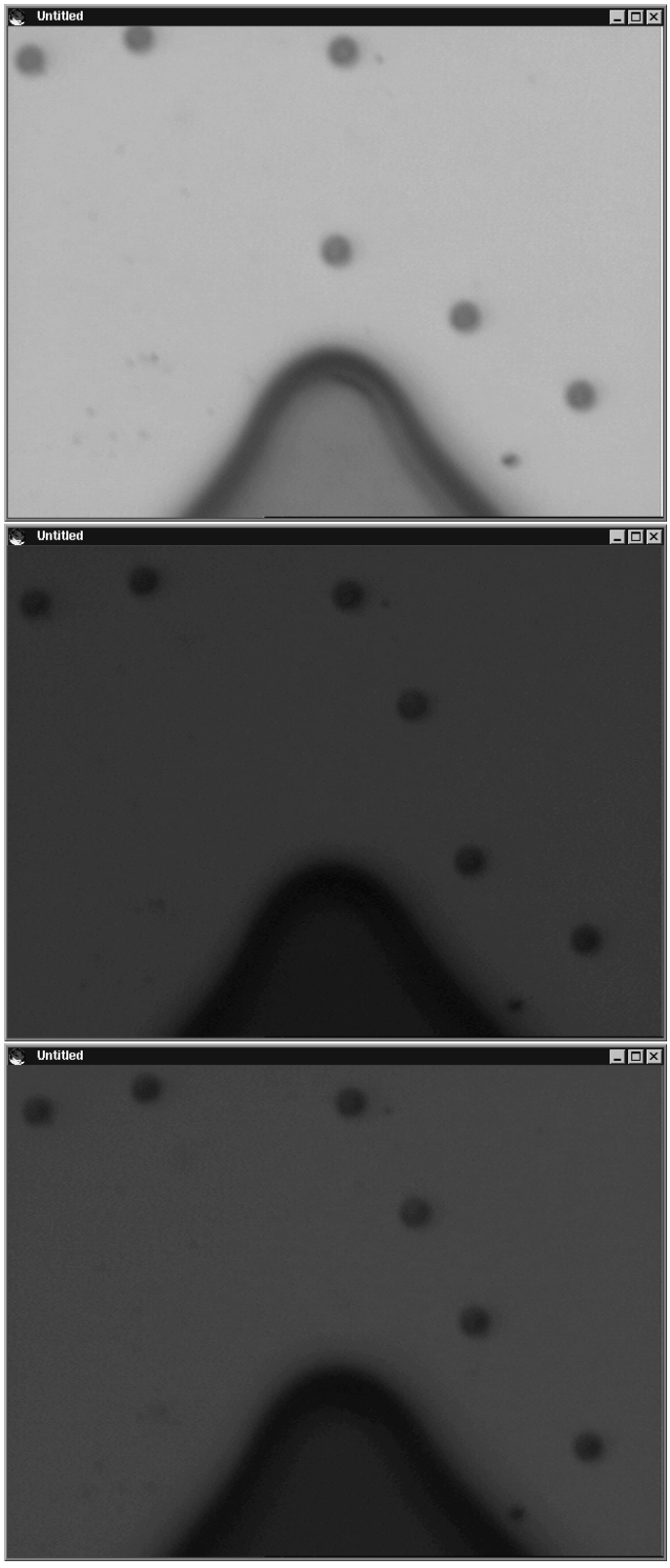

Figure 7.24: Pushing particle result where the initial positions are shown in upper image, and the last configuration in the bottom one.

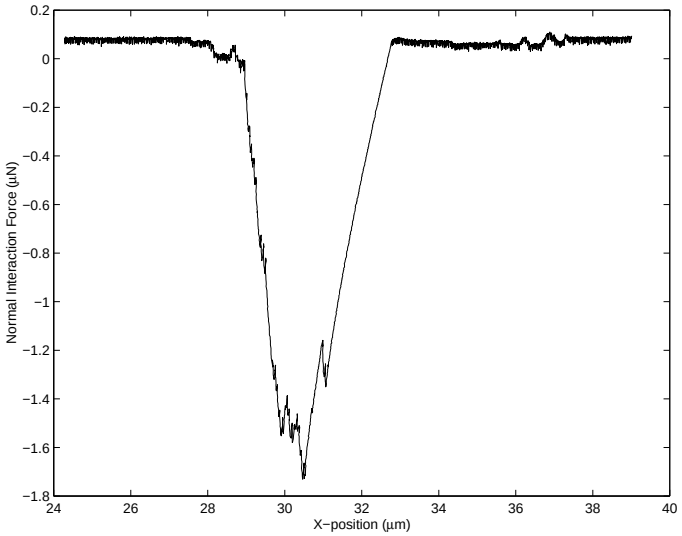

(a)

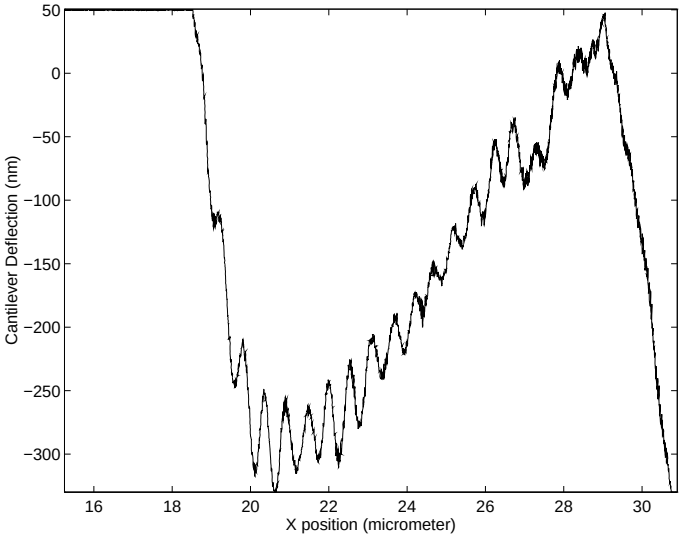

(b)

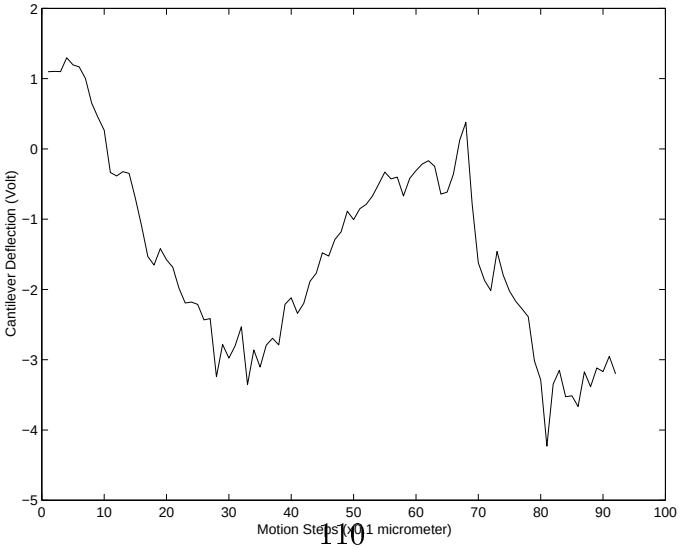

(c)

Figure 7.25: Sliding behaviour prediction from the z-deflection data after the shearing point. (a) linear shape for pure sliding, (b) saw-like shape for stick-slip motion, and (c) sinusoidal shape for rolling motion.

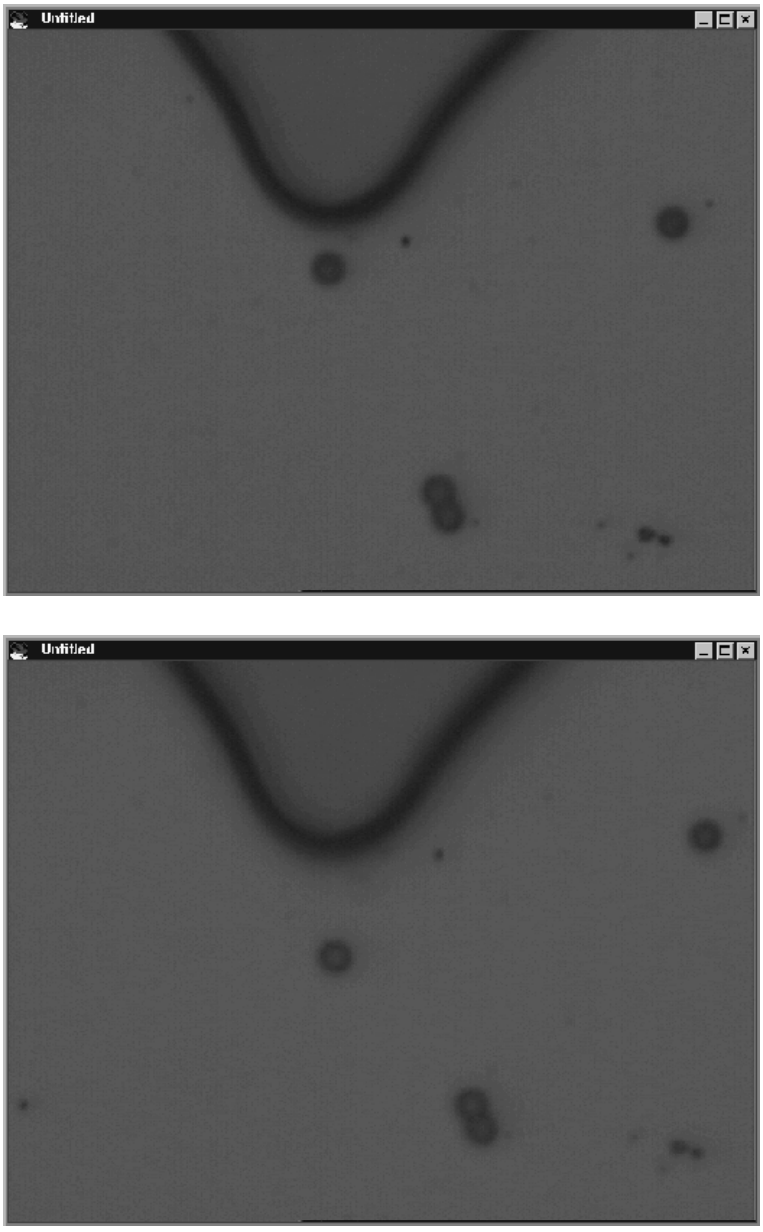

Figure 7.26: Contact pushing of 2 μm size latex particles on a silicon surface using the AFM tip as a pushing tool: before (left) and after pushing (right).

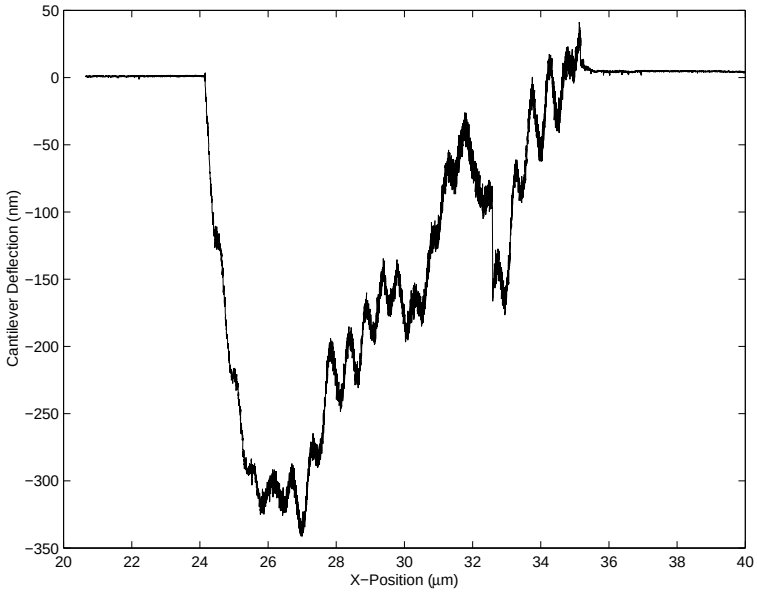

Figure 7.27: Piezolever deflection during pushing.

Chapter 8

Conclusion

8.1 Summary of the Thesis

In this study, a teleoperated 2-D manipulation of micro/nano objects, especially spherical particles, and tele-touch interaction with nano scale surfaces is presented. Tele-Microrobotics and Tele-Nanorobotics systems using Atomic Force Microscope (AFM) as a push-and-pull contact type manipulator and force and 3-D topology sensor are proposed. As AFM, a home-made open structure AFM system using piezoresistive cantilevers is constructed. Modeling and control of the AFM cantilever, and modeling of micro/nano scale forces have been proposed for telemanipulation applications. Besides of 3-D visual feedback in the user interface, a 1-DOF home-made haptic device has been constructed for nano scale tactile sensing and generating motion commands for the AFM. Introducing teleoperation control systems with Virtual Impedance control and force-servo control approaches, micro/nano scale forces or geometries are felt by the operator. As experiments, tele-compliance feedback of surfaces, topology feedback of Si fabricated etched shapes, 0.484, $1, 2\ \mu m$ size latex particle assembly in 2-D, and finally Virtual Reality based Micro/Nano Dynamics simulator for 1-DOF and 2-DOF micro/nano force feedback during interaction are conducted. These experiments show that the system can be utilized for different tele-micro/nanomanipulation applications such as 2-D micro/nano particle assembly, tribological characterization of particle-substrate interfaces, or even biological object manipulation.

8.2 Problems and Future Works

The present system can be improved in different ways for more complex micro/nano manipulation tasks. The problems and possible improvements are as follows:

- Real-time visual feedback at the nano scale using Scanning Probe Microscopes is almost not possible since a scanning data take long time, and during manipulation,

the tip is utilized only for manipulation, and cannot be used as the topology sensor at the same time. As solutions to this problem:

  - Using the real-time force feedback to compensate the errors during the manipulation (the approach in this thesis).
  - Using a far-field visual sensor such as Scanning Electron Microscope (SEM). Here, there are additional problems introduced such that SEM necessitates vacuum environment which limits the mechanical design and increases the cost, it can be used only for (1/2)conducting and some special nonconducting materials, its best resolution is around 5 nm, and it can only provide 2-D information (no depth information is possible which is not good for manipulation applications). Furthermore, high-resolution Optical Microscope (OM) can also be used depending on the application. With florescense, or other special type of colouring techniques, resolutions down to $10 - 20$ nm may even be visible. However, it is limited to application, and 2-D. Thus, if AFM and OM are integrated together, it can be a good combination (also this kind of combination is desirable for all manipulation systems since a rough micro imaging simplifies the initial setting and alignment operations such as in our system).
  - Improving the proposed models in this thesis, and updating the Nano Simulator to 3-D, the behaviour of the manipulated objects and manipulators can be **animated** by the real-time experimental data and physical model-based predictive display. This kind of technique is possible in teleoperated space-robotics applications where there is a long delay time, and model-based predictive displays can animate the pseudo-real-time teleoperation motions.
  - Array of multiple AFM cantilevers can enable parallel and fast scanning of the surfaces [48]. However, many cantilevers add complexities of simultenous control, image merging, collision, and etc. type of problems.

- Contact type mechanical manipulation can cause problems for the manipulation of very soft materials such as bio-samples. Therefore, optical tweezers, electrophoresis, and etc. kind of non-contact manipulation techniques should be integrated with AFM system for the sensitive materials.

- **3-D Manipulation**

  Using one AFM cantilever, mostly 2-D mechanical type of manipulations can be realized. Then the achievable tasks are very limited, and 3-D manipulation is desirable for 3-D fabrication technologies for the future. For 3-D manipulation, following approaches could be possible:

- Assuming the manipulated objects are conductive or semiconductive, STM-like electric pulse type of manipulation can enable 3-D pick and place task of molecules or nano objects. Since the STM measures the tunneling current not the interatomic force, it is not desirable for delicate applications which need force control. Therefore, one possible solution is using STM/AFM type metal-coated AFM cantilevers where the manipulation can be done by voltage pulses between the tip and objects, and also the force information can be get in real-time.
- More than one AFM cantilevers can be used as a robot gripper as shown in Figure 8.1. However, with the present AFM cantilever fabrication techniques, the tip of the cantilever is in the inside part of the beam, and cannot be utilized as a gripper as given in the figure. Therefore, special cantilevers which have the tip at the end of the beam and has an outside slope should be fabricated. Also, in order to move the cantilevers independently as a gripper, the optical detection technique is not convenient, and piezoresistive or piezoelectric type of cantilevers should be used.
- By using biochemicals at the apex of the AFM tip, molecular adhesion or recognition type of characateristics can be used to pick and place of special materials.

- *Real 3-D imaging using AFM?*

  The present AFM images constitute of the outer surface topology images, and cannot mostly enable the 3-D complex structure imaging due to its imaging/scanning principle, finite size tip and tip shape. However, *manipulation* tools such as another AFM tip or an optical tweezer can be utilized for fixing and rotating the samples, and then the stretched objects can be scanned with an AFM tip. Thus, more compplete 3-D topology images of complex structures could be held.

- Sample preparation for the micro/nano scale object pushing applications is challenging. The frictional properties of the object and substrate interface (monolayers can be used for reducing the friction), the adhesional forces, environmental conditions, and object fixation chemicals are all specific to the material types and object sizes. Thus, chemistry and material science are indispensable backgrounds for good sample fixation and material selection.

- For the tribological characterization application, torsional deflection measurement is the best for decoupled and direct measurement where the normal deflection can be utilized only indirectly in our case. Thus, optical deflection system can be used while thus kind of detection limits the motion of the cantilever. The best choise could be a piezoresistive torsional deflection detection system [7].

- Fast user-defined precision positioning with few nanometers accuracy is necessary for reliable and *repeatable* manipulation tasks. Thus, open-loop stages are almost not reliable, and sensor-integrated stages is one possible solution. The commerically available best stages utilize the capacitive sensors while there are many problems of precision mechanics, thermal drift, electronics noise, environmental disturbances, and etc. Also, the other problem is, when the sensors are integrated to the stage and closed-loop control is held, the bandwidth of the positioning drops very much since the control takes time, and the stage mass becomes very large with the sensor mechanics design which reduces the resonance frequency.

- Since the interactions at the micro/nano scale is mostly nonlinear and coupled, *intelligent*, stable and robust manipulation control strategies should be introduced. Teleoperation reduced the intelligence necesity to the proposed system while the bilateral teleoperation can have the stability problems.

- After changing to a both bending and torsional deflection detection system, haptic device degree of freedom should be increased to three.

- Even the environmental parameters are controlled with adhesion force modeling and control, still there may be sticking problems in air conditions due to the large capillary forces, and produced electrostatic forces during contacting and manipulating objects. Therefore, manipulation in liquid could be a solution since these forces are largely reduced. However, in liquid environments, liquid flow instabilities and double-layer type of new forces are introduced, and these forces should be controlled carefully. Furthermore, liquid manipulation also enables *in situ* biological object manipulation as shown in Figure 8.2.

- Piezoresistive cantilevers are very novel tools for future micro/nano robots in the sense of integrated sensor-type manipulation tools. However, these type of sensors have the electronic and thermal noise and drift problems with compared to the laser detection cantilevers [27]. Thus, special care should be taken for controlling these noises with temperature control and low-noise electronics.

- The proposed micro/nano force models all assume continuum mechanics modeling. However, going to the 10s of nanometer, quantum effect and other type of discontinuous interatomic forces become more dominant. Therefore, Molecular Dynamics Modeling or other type of advanced molecular scale simulation techniques should be user for detailed behaviour understanding.

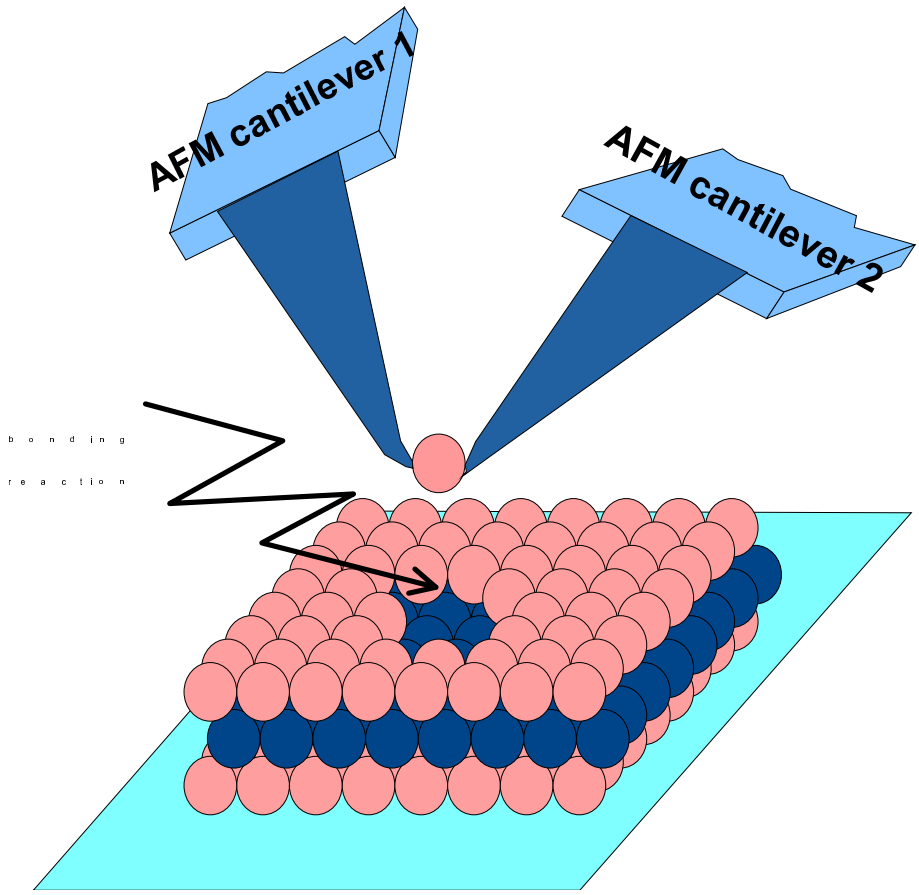

Figure 8.1: 3-D nano manipulation using two AFM cantilevers with the tips at the end of the beam.

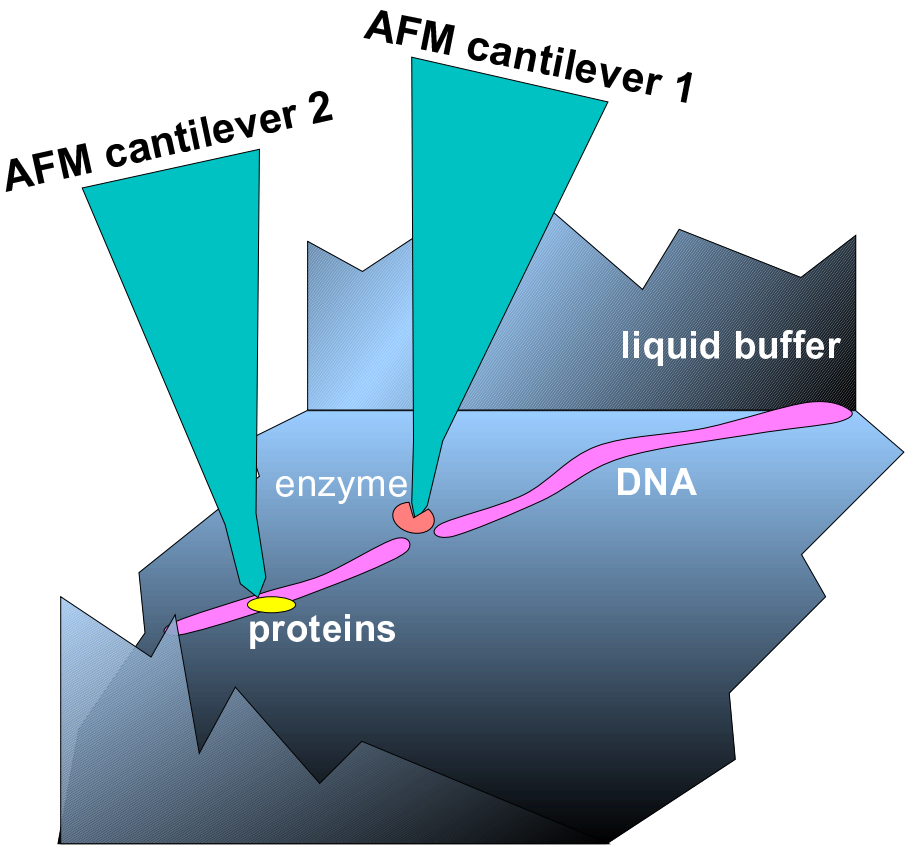

Figure 8.2: Biological object observation and manipulation *in situ* environment in liquid buffers using the AFM cantilevers as cutting, topology sensing, force and mechanical property characterization, and etc. tools.

References

[1] M. Aono, C. S. Jiang, and at al. Method to measure local electrical, optical and magnetic properties on the nanometer scale. In *Proc. of the France-Japan Workshop on from Nano to Macro Science and Tech. through Microsystems*, page 23, 1998.

[2] F. Arai, D. Ando, and T. Fukuda. Micro manipulation based on micro physics: Strategy based on attractive force reduction and stress measurement. In *Proc. of the IEEE Int. Conf. on Robotics and Automation*, pages 236–241, 1995.

[3] F. Arai, D. Andou, Y. Nonoda, T. Fukuda, H. Iwata, and K. Itoigawa. Micro endeffector with micro pyramids and integrated piezoresistive force sensor. In *Proc. of the IEEE/RSJ Int. Conf. on Intelligent Robots and Systems*, pages 842–849, 1996.

[4] C. Baur, A. Bugaciv, and et al. Nanoparticle manipulation by mechanical pushing: Underlying phenomena and real-time monitoring. *Nanotechnology*, 9:360–364, 1998.

[5] P. H. Beton, A. W. Dunn, and P. Moriarty. Manipulation of c60 molecules on a si surface. *Applied Physics Letters*, 67(8):1075–1077, August 1995.

[6] K.F. Bohringer, R.S. Fearing, and K.Y. Goldberg. Parallel microassembly. In *Workshop on Precision Manipulation at Micro and Nano Scales, IEEE Int. Conf. on Robotics and Automation*, pages 110–135, 1998.

[7] J. Brugger, J. Burger, and et al. Lateral force measurements in a scanning force microscope with piezoresistive sensors. In *8th Int. Conf. on Solid-State Sensors and Actuators, and Eurosensors*, pages 636–639, Junw 25-29, 1995.

[8] B. Brushan. *Micro/Nanotribology and Its Applications.* Kluwer Academic, Vol. E330, 1997.

[9] N. A. Burnham, O.P. Behrend, and et al. How does a tip tap? *Nanotechnology*, 8:67–75, 1997.

[10] N. A. Burnham and A. J. Kulik. Surface forces and adhesion. *Handbook of Micro/Nanotribology*, ed. by B. Bhushan, CRC Press, Dec. 1997.

[11] J. Chen, C. Dimattia, and et al. Sticking to the point: A friction and adhesion model for simulated surfaces. In *Proc. of teh Annual Symp. on Haptic Interfaces for Virutal Env. and Teleoperator Systems*, 1997.

[12] A. Codourey, M. Rodriguez, and I. Pappas. Human machine interaction for manipulations in the microworld. In *Proc. of the IEEE Int. Workshop on Robot and Human Communication*, pages 244–249, 1996.

[13] J. Colchero, E. Meyer, and O. Marti. Friction on atomic scale. *Handbook of Micro/Nano Tribology, Second Ed., CRC Press*, pages 273–333, 1999.

[14] J. E. Colgate. Robust impedance shaping telemanipulation. *IEEE Transactions on Robotics and Automation*, 9(4):374–384, Aug. 1993.

[15] J. Crassous, E. Charlaix, H. Gayvallet, and J.L. Loubert. Experimental study of a nanometric liquid bridge with a surface force apparatus. *Langmuir*, 9:1995–1998, 1993.

[16] D. M. Eigler and E. K. Schweitzer. Positioning single atoms with a scanning electron microscope. *Nature*, pages 524–526, Apr. 1990.

[17] T. Yamamoto et al. Molecular surgery of dna using restriction enzymes. In *Proc. of the France-Japan Workshop on from Nano to Macro Science and Tech. through Microsystems*, page 38, 1998.

[18] M. Falvo, R. Superfine, S. Washburn, and et al. The nanomanipulator: A teleoperator for manipulating materials at the nanometer scale. In *Proc. of the Int. Symp. on the Science and Technology of Atomically Engineered Materials*, pages 579–586, Nov 1995.

[19] M. R. Falvo, S. Washburn, and et al. Manipulation of individual viruses: Friction and mechanical properties. *Biophysical Journal*, 72:1369–1403, March 1997.

[20] M.R. Falvo, R.M. Taylor II, and et al. Nanometer-scale rolling and sliding of carbon nanotubes. *Nature*, 397:236–238, 21 Jan. 1999.

[21] R. S. Fearing. Survey of stcking effects for micro parts handling. In *Proc. of the IEEE/RSJ Int. Conf. on Intelligent Robots and Systems*, pages 212–217, 1995.

[22] J. T. Feddema, P. Xavier, and R. Brown. Assembly planning at the micro scale. In *Workshop on Precision Manipulation at Micro and Nano Scales, IEEE Int. Conf. on Robotics and Automation*, pages 56–69, 1998.

[23] F. J. Giessibl and B. M. Trafas. Piezoresistive cantilevers utilized for scanning tunneling and scanning force microscope in ultrahigh vacuum. *Rev. Sci. Instrum.*, 65(6):1923–1929, June 1994.

[24] M. Goldfarb. Dimensional analysis and selective distortion in scaled bilateral telemanipulation. In *Proc. of the IEEE Int. Conf. on Robotics and Automation*, pages 1609–1614, 1998.

[25] M. Guthold, M.R. Falvo, and et al. Controlled manipulation of molecular samples with the nanomanipulator. In *Proc. of the IEEE/ASME Int. Conf. on Advanced Intelligent Mechatronics*, 1999.

[26] L. T. Hansen, A. Kuhle, and et al. A technique for positioning nanoparticles using an atomic force microscope. *Nanotechnology*, 9:337–343, 1998.

[27] O. Hansen and A. Boisen. Noise in piezoresistive atomic force microscopy. *Nanotechnology*, 10:51–60, 1999.

[28] H. Hashimoto and S. Monorotkul. Tele-handshake through the internet. In *Proc. of the IEEE Int. Workshop on Robot and Human Communication*, pages 90–95, 1996.

[29] T. R. Hicks and P. D. Atherton. *The Nano Positioning Book*. Queensgate Inst. Ltd., 1997.

[30] R. L. Hollis, S. Salcudean, and D. W. Abraham. Toward a tele-nanorobotic manipulation system with atomic scale force feedback and motion resolution. In *Proc. of the IEEE Int. Conf. on MicroElectromechanical Systems*, pages 115–119, 1990.

[31] S. Horiguchi. Virtual reality interface for afm-based nanomanipulation. *M.Sc. Thesis*, Dept. of Electrical Engineering, March 1999.

[32] S. Horiguchi, M. Sitti, and H. Hashimoto. Visualization interface for afm-based nano-manipulation. In *Proc. of the IEEE Int. Symp. on Industrial Electronics*, July 1999 (to be published).

[33] I. W. Hunter, S. Lafontaine, P. M. Nielsen, P. J. Hunter, and J. M. Hollerbach. Manipulation and dynamic mechanical testing of microscopic objects using a telemicro-robot system. *IEEE Control Systems Magazine*, pages 3–9, Feb. 1990.

[34] T. Inoue, K. Iwatani, I. Shimoyama, and H. Miura. Micromanipulation using magnetic field. In *Proc. of the IEEE Int. Conf. on Robotics and Automation*, pages 679–684, 1995.

[35] J. Israelachvili. *Intermolecular and Surface Forces.* Academic Press, 1992.

[36] K.L. Johnson. A continuum mechanics model of adhesion and friction in a single asperity contact. *Micro/Nanotribology and its Applications, Kluwer Ac. Pub.*, pages 151–168, 1997.

[37] T. Junno, K. Deppert, L. Montelius, and L. Samuelson. Controlled manipulation of nanoparticles with an atomic force microscopy. *App. Physics Letters*, 66(26):3627–3629, June 1995.

[38] K. Kaneko, H. Tokashiki, K. Tanie, and K. Komoriya. A development of experimental system for macro-micro teleoperation. In *Proc. of the IEEE Int. Workshop on Robot and Human Communication*, pages 30–35, 1995.

[39] T. Kasaya, H. Miyazaki, S. Saito, and T. Sato. Micro object handling under sem by vision-based automatic control. In *Proc. of the IEEE Int. Conf. on Robotics and Automation*, pages 2189–2196, 1999.

[40] S. Katsura, K. Hirano, and et al. Direct laser trapping of single dna molecules in the globular state. *Nucleic Acids Research*, 26(21):4943–4945, 1998.

[41] K. Koyano and T. Sato. Micro object handling system with concentrated visual fields and new handling skills. In *Proc. of the IEEE Int. Conf. on Robotics and Automation*, pages 2541–2548, 1996.

[42] M. Krantz. Building a better world–atom by atom. *Times*, pages 62–63, Dec. 2 1996.

[43] J.M. Lehn. Supramolecular chemistry and nanotechnology. In *France-Japan Workshop on from Nano to Macroscale Science and Technology through Micro Systems*, pages 14–15, Apr. 1997.

[44] I.W. Lyo and P. Avouris. Filed-induced nanometer-to atomic-scale manipulation of silicon surfaces with the stm. *Science*, 253:173–176, 12 July 1991.

[45] W. R. Mark, S. C. Randolph, M. Finch, and et al. Adding force feedback to graphics systems: Issues and solutions. In *Computer Graphics Proceedings SIGGRAPH*, pages 447–452, 1996.

[46] C. M. Mate. Force microscopy studies of the molecular origin of friction and lubrication. *IBM J. Res. Develop.*, 39(6):617–627, Nov. 1995.

[47] D. Maugis. Adhesion of spheres: The jkr-dmt transition using a dugdale model. *J. of Colloidal and Interface Science*, 150(1):243–269, April 1992.

[48] S.C. Minne, S.R. Mannalis, and C.F. Quate. Parallel atomic force microscopy using cantilevers with integrated piezoresistive sensors and integrated piezolectric actuators. *Appl. Phys. Lett.*, 67(26):3918–3920, 25 Dec. 1995.

[49] H. Miyazaki and T. Sato. Pick and place shape forming of three-dimensional micro structures from fine particles. In *Proc. of the IEEE Int. Conf. on Robotics and Automation*, pages 2535–2540, 1996.

[50] K. Morishima, T. Fukuda, F. Arai, and K. Yoshikawa. Manipulation of dna molecule utilizing the conformational transition in the higher order structure of dna. In *Proc. of the IEEE Int. Conf. on Robotics and Automation*, pages 1454–1459, 1997.

[51] B. J. Nelson and Y. Zhou. Task-based micromanipulation control strategies for assembly of hybrid mems. In *Workshop on Precision Manipulation at Micro and Nano Scales, IEEE Int. Conf. on Robotics and Automation*, pages 5–29, 1998.

[52] T. Ondarcuhu and C. Joachim. Combing a nanofiber in a nanojunction. *Nanotechnology*, 1998 (to be appeared).

[53] I. Pappas and A. Codourey. Visual control of a microrobot operating under a microscope. In *Proc. of the IEEE/RSJ Int. Conf. on Intelligent Robots and Systems*, pages 993–1000, 1996.

[54] U. Rabe, J. Turner, and W. Arnord. Analysis of the high-frequency response of atomic force microscope cantilevers. *Appl Phys. A*, 66:277–282, 1998.

[55] T. R. Ramachandran, C. Baur, and et al. Direct and controlled manipulation of nanometer-sized particles using the non-contact atomic force microscope. *Nanotechnology*, 9:237–245, 1998.

[56] A. A. Requicha, C. Baur, and et al. Nanorobotics assembly of two-dimensional structures. In *Proc. of the Workshop on Precision Manipulation at the IEEE Robotics and Autom. Conf.*, pages 136–150, 1998.

[57] A.A.G. Requicha, C. Baur, A. Bugacov, and et al. Nanorobotic assembly of two-dimensional structures. In *Proc. of the IEEE Int. Conf. on Robotics and Automation*, pages 3368–3374, 1998.

[58] R. Resch, C. Baur, and et al. Manipulation of nano particles using dynamic force microscopy: Simulation and experiments. *App. Phys. A*, 67(3):265–271, Sept. 1998.

[59] Y. Rollot, S. Regnier, P. Bidaud, and J.C. Guinot. Some conditions of micromanipulation by adhesion. In *Proc. of the Symp. Franco-Israelien*, France, 1998.

[60] S. Saito, H. Miyazaki, and T. Sato. Pick and place operation of a micro object with high reliability and precision based on micro physics under sem. In *Proc. of the IEEE Int. Conf. on Robotics and Automation*, pages 2736–2743, 1999.

[61] D. Sarid, J. P. Hunt, R. K. Workman, and et al. The role of adhesion in tapping-mode atomic force microscopy. *Appl. Phys. A*, (66):283–286, 1998.

[62] Dror Sarid. *Scanning Force Microscopy: With Applications to Electric, Magnetic and Atomic Forces*. Oxford University Press, 1994.

[63] K. Sasaki, H. Fujiwara, and H. Masuhara. Optical manipulation of a lasing particle and its application to near-field microsprectroscopy. *J. Vac. Sci. Technol. B*, 15(6):2786–2790, Nov./Dec. 1997.

[64] T. Sato. Micro/nano manipulation world. In *Proc. of the IEEE/RSJ Int. Conf. on Intelligent Robots and Systems*, pages 834–841, 1996.

[65] T. Sato, J. Ichikawa, M. Mitsuishi, and Y. Hatamura. A new micro-teleoperation system employing a hand-held force-feedback pencil. In *Proc. of the IEEE Int. Conf. on Robotics and Automation*, pages 1728–1733, 1994.

[66] D.M. Schafer, R. Reifenberger, A. Patil, and R.P. Andres. Fabrication of two-dimensional arrays of nanometric-size clusters with the atomic force microscopy. *App. Physics Letters*, 66(8):1012–1014, Feb. 1995.

[67] M. Sitti and H. Hashimoto. Teleoperated nano scale object manipulation. In *Recent Advances on Mechatronics*, pages 322–335. ed. by O. Kaynak, S. Tosunoglu and M.J. Ang, Springer Verlag Pub., Singapore, 1999.

[68] M. Sitti and H. Hashimoto. Two-dimensional fine particle positioning under optical microscope using a piezoresistive cantilever as a manipulator. *J. of Micromechatronics*, May 1999 (in review process).

[69] M. Sitti and H. Hashimoto. Tele-nanorobotics using atomic force microscope. In *Proc. of the IEEE/RSJ Int. Conf. on Intelligent Robots and Systems*, pages 1739–1746, Canada, Oct. 1998.

[70] M. Sitti and H. Hashimoto. Two-dimensional fine particle positioning using a piezoresistive cantilever as a micro/nano-manipulator. In *Proc. of the IEEE Int. Conf. on Robotics and Automation*, pages 2729–2735, Detroit, May 1999.

[71] M. Sitti and H. Hashimoto. Macro to nano tele-manipulation through nanoelectromechanical systems. In *Proc. of the IEEE Ind. Electronics Conf.*, pages 98–103, Germany, Sept. 1998.

[72] M. Sitti and H. Hashimoto. Tele-nanorobotics using atomic force microscope. *Advanced Robotics Journal*, Invited Session on IROS'98, Fall 1999 (in review process).

[73] M. Sitti and H. Hashimoto. Pushing micro/nano scale particles on substrates using atomic force microscope probe towards tribological characterization of particle-substrate interfaces. In *STM'99 Conf.*, (to be published) Korea, July 1999.

[74] M. Sitti, M. Hoummady, and H. Hashimoto. Trends on mechatronics for micro/nano telemanipulation: Survey and requirements. In *IFAC Information Control in Manifacturing 1998*, pages 235–240. edited by G. Morel and F. B. Vernadat, Pergamon Pub., Belgium, 1998.

[75] R. W. Stark, S. Thalhammer, and et al. The afm as a tool for chromosomal dissection - the influence of physical parameters. *Appl. Phys. A*, 66:579–584, 1998.

[76] J.A. Stroscio and D.M. Eigler. Atomic and molecular manipulation with the scanning tunneling microscope. *Science*, 254(5036):1319–1326, Nov. 1991.

[77] J. Tamayo and R. Garcia. Deformation, contact time, and phase contrast in tapping mode scanning force microscopy. *Langmuir*, 12(18):4430–4435, 1996.

[78] T. Tanikawa, T. Arai, and T. Masuda. Development of micro manipulation system with two-finger micro hand. In *Proc. of the IEEE/RSJ Int. Conf. on Intelligent Robots and Systems*, pages 850–855, 1996.

[79] M. Tortonese, R. C. Barrett, and C. F. Quate. Atomic resolution with an atomic force microscope using piezoresistive detection. *App. Physics Letters*, 62(22):834–836, Feb. 1993.

[80] H. Uchida, D.H. Huang, J. Yoshinobu, and M. Aono. Single-atom manipulation on the si(111)7x7 surface by the stm. *Surface Science*, 287/288:1056–1061, 1993.

[81] M. R. VanLandingham, S. H. McKnight, and et al. Relating elastic modulus to indentation response using atomic force microscopy. *J. of Materials Science Letters*, 1996.

[82] A. Yamamoto, S. Mishima, N. Maruyama, and M. Sumita. A new technique for direct measurement of the shear force necessary to detach a cell from a material. *Biomaterials*, 19:871–879, 1998.

[83] J. Yuqiu, C. Juang, and et al. Mechanical, electrical, and chemical manipulation of single dna molecules. *Nanotechnology*, 3:16–20, 1992.

[84] W. Zesch and R. S. Fearing. Alignmnet of microparts using force controlled pushing. In *SPIE Conf. on Microrobotics and Micromanipulation*, Boston, Nov. 2-5 1998.

[85] Y. Zhou, B. J. Nelson, and B. Vikramaditya. Fusing force and vision feedback for micromanipulation. In *Proc. of the IEEE Int. Conf. on Robotics and Automation*, pages 1220–1225, 1998.